Channel Estimation and Interference Mitigation for Reconfigurable Intelligent Surfaces

DOĞA GÜRGÜNOĞLU

Doctoral Thesis in Electrical Engineering
Stockholm, Sweden, 2025

KTH Royal Institute of Technology
School of Electrical Engineering and Computer Science
Division of Decision and Control Systems
SE-10044 Stockholm
Sweden

TRITA-EECS-AVL-2025:8
ISBN 978-91-8106-156-7

Akademisk avhandling som med tillstånd av Kungl Tekniska högskolan framlägges till offentlig granskning för avläggande av Teknologie doktorexamen i elektroteknik torsdagen den 20 mars 2025 klockan 09.00 i Sal Ka-Sal C, Kistagången 16, Kungliga Tekniska Högskolan, Stockholm.

Tryck: Universitetsservice US AB

Abstract

In the sixth generation of wireless communication systems (6G), there exist multiple candidate enabling technologies that help the wireless network satisfy the ever-increasing demand for speed, coverage, reliability, and mobility. Among these technologies, reconfigurable intelligent surfaces (RISs) extend the coverage of a wireless network into dead zones, increase capacity, and facilitate integrated sensing and communications (ISAC) tasks by consuming very low power, thus contributing to energy efficiency as well.

RISs are meta-material-based devices whose electromagnetic reflection characteristics can be controlled externally to cater to the needs of the communication links. Most ubiquitously, this comes in the form of adding a desired phase shift to an incident wave before reflecting it, which can be used to phase-align multiple incident waves to increase the strength of the signal at the receiver and provide coverage to an area that otherwise would be a dead zone.

While this portrays an image of a dream technology that would boost the existing wireless networks significantly, RISs do not come without engineering problems. First of all, the individual elements do not exhibit ideal reflection characteristics, that is, they attenuate the incident signal in a fashion depending on the configured phase shift. This creates the phenomenon called "phase-dependent amplitude". Another problem caused by RISs is the channel estimation overhead. In a multiple-antenna communication system, the channel between two terminals is as complex as the product of the number of antennas at each end. However, when an RIS comes into the equation, the cascade of the transmitter-RIS and RIS-receiver channels has a complexity further multiplied by the number of RIS elements. Consequently, the channel estimation process to utilize the RIS effectively becomes more demanding, that is, more pilot signals are required to estimate the channel for coherent reception. This adversely affects the effective data rate within a communication system since more resources need to be spent for pilot transmission and fewer resources can be allocated for data transmission. While there exists some work on reducing the channel dimensions by exploiting the channel structure, this problem persists for unstructured channels. In addition, for the wireless networks using multiple RISs, a new kind of pilot contamination arises, which is the main topic of this thesis.

In the first part of this thesis, we study this new kind of pilot contamination in a multi-operator context, where two operators provide services to their respective served users and share a single site. Each operator has a single dedicated RIS and they use disjoint frequency bands, but each RIS inadvertently reflects the transmitted uplink signals of the user equipment devices in multiple bands. Consequently, the concurrent reflection of pilot signals during the channel estimation phase introduces a new inter-operator pilot contamination effect. We investigate the implications of this effect in systems with either deterministic or correlated Rayleigh fading channels, specifically focusing on its impact on channel estimation quality, signal equalization, and channel capacity. The numerical results demonstrate the substantial degradation in system performance caused by this phenomenon and highlight the

pressing need to address inter-operator pilot contamination in multi-operator RIS deployments. To combat the negative effect of this new type of pilot contamination, we propose to use orthogonal RIS configurations during uplink pilot transmission, which can mitigate or eliminate the negative effect of inter-operator pilot contamination at the expense of some inter-operator information exchange and orchestration.

In the second part of this thesis, we revisit the inter-operator pilot contamination. This time, however, we investigate the use of multiple antennas at the base stations to eliminate inter-operator pilot contamination. While orthogonalizing the RIS configurations as in the single antenna case eliminates pilot contamination, it doubles the number of pilots required to perform channel estimation. Considering the extant pilot overhead problem in RIS-aided communication systems, an alternative approach that does not increase the number of pilots to be transmitted is necessary. To this end, we propose using receive beamforming and null forming to eliminate inter-operator pilot contamination. We show that it is possible to eliminate inter-operator pilot contamination by placing nulls toward the signal coming from the other operator's RIS.

In the third part of this thesis, we consider a single-operator-two-RIS ISAC system where the single user is both a communication terminal and a positioning target. Based on the uplink positioning pilots, the base station aims to estimate both the communication channel and the user's position within the indoor environment by estimating the angle of arrival (AoA) of the impinging signals on both RISs and then exploiting the system and array geometries to estimate the user position and user channels respectively. Although there is a single operator, due to the presence of multiple RISs, pilot contamination occurs through the same physical means as multi-operator pilot contamination unless the channel estimation process is parameterized. Since the communication links are considered to be pure line-of-sight (LOS), their structure allows the reduction of the number of unknown parameters. Consequently, the reduction of information caused by pilot contamination does not affect the channel estimation procedure, hence the pilot contamination is overcome. In addition, the position of the user is determined by intersecting the lines drawn along the AoA estimates. We adopt the Cramér-Rao Lower Bound (CRLB), the lower bound on the mean squared error (MSE) of any unbiased estimator, for both channel estimation and positioning. Our numerical results show that it is possible to utilize positioning pilots for parametric channel estimation when the wireless links are LOS.

The fourth part of the thesis ventures into the domain of near-field communications. Here, we consider the estimation of parametric channels in the uplink of a multi-user multiple-input-multiple-output (MU-MIMO) communication system where the users are located within the radiative near field (Fresnel region) of the base station's aperture antenna. In this setup, we consider near-field channel models characterized by the users' distances and azimuth angles relative to the aperture array. We derive the CRLB to estimate these location parameters and the parametric channel estimates in closed form. Moreover, we consider using the 2D-MUSIC algorithm to esti-

mate these parameters and compare the performance of the 2D-MUSIC algorithm with the CRLB. Our results indicate that the 2D-MUSIC algorithm is asymptotically consistent and efficient.

Keywords: Reconfigurable intelligent surface, channel estimation, pilot contamination, positioning, angle of arrival estimation, integrated sensing and communications, receive beamforming, radiative near field.

Sammanfattning

I den sjätte generationen av trådlösa kommunikationssystem (6G) finns flera potentiella tekniker som gör det möjligt för det trådlösa nätverket att uppfylla de ständigt ökande kraven på hastighet, täckning, tillförlitlighet och rörlighet. Bland dessa tekniker återfinns de så kallade omkonfigurerbara intelligenta ytor (reconfigurable intelligent surface - RIS på Engelska), vilka kan förlänga ett nätverks täckning till områden utan signal (så kallade "dead zones"), öka kapaciteten och underlätta integrerade sensor- och kommunikationslösningar (ISAC). Samtidigt förbrukar RIS mycket lite energi och bidrar därmed till ökad energieffektivitet.

RIS är en metaytebaserad teknologi där ytan kan styras externt för att justera hur inkommande elektromagnetiska vågor reflekteras. Vanligtvis innebär detta att varje element på ytan åstadkommer en önskad fasförskjutning av den inkommande signalen innan den reflekteras, vilket kan utnyttjas för att fassjustera flera inkommande vågor och därmed förstärka signalen vid mottagaren. På så sätt kan täckning ges till annars otillgängliga områden.

Trots att denna teknik lovar betydande förbättringar för dagens trådlösa nätverk medför RIS även nya ingenjörsmässiga utmaningar. För det första uppvisar de enskilda elementen inte perfekta reflektionskarakteristiker, utan dämpar signalen på ett sätt som beror på den inställda fasförskjutningen, ett fenomen som kallas fasberoende amplitud. För det andra uppstår extra overhead inom kanalskattningen. I ett flerantennsystem är kanalens komplexitet mellan två noder redan omfattande, men när en RIS läggs till multipliceras komplexiteten med antalet RIS-element. Följaktligen krävs fler pilotsignaler för att skatta kanalen i system som använder RIS, vilket minskar den effektiva datahastigheten eftersom fler resursblock går åt till pilotsändning. Även om det finns metoder för att reducera kanalens dimensioner genom att utnyttja kanalstruktur, kvarstår problemet för kanaler utan särskild struktur. Därtill uppstår en ny typ av pilotförorening (pilot contamination) i scenarier med flera RIS:ar eller flera operatörer, vilket är huvudtemat i denna avhandling.

I avhandlingens första del studeras denna nya typ av pilotförorening i ett multioperatörsscenario, där två operatörer delar samma plats men använder olika frekvensband och har varsin dedikerad RIS. Även om frekvensbanden är åtskilda reflekterar varje RIS oavsiktligt de upplänksignaler som skickas av användare i båda banden. Under kanalskattningsfasen leder denna samtidiga reflektion av pilotsignaler till interoperatörs-pilotförorening. Vi analyserar hur fenomenet påverkar system med både deterministiska och korrelerade Rayleigh-fadande kanaler, med fokus på kanaluppskattning, signalequalisering och kapacitet. Numeriska resultat visar en tydlig prestationsförsämring och understryker att interoperatörs-pilotförorening är ett allvarligt problem i multioperatörssystem med RIS. För att motverka denna effekt föreslår vi att använda ortogonala RIS-konfigurationer under upplänkens pilotfas. Detta kan mildra eller helt eliminera pilotföroreningen, men kräver samordning och viss informationsdelning mellan operatörerna.

I avhandlingens andra del studeras samma interoperatörs-pilotförorening men i ett scenario där basstationerna har flera antenner. Att ortogonalisera

RIS-konfigurationerna, som i fallet med en enda antenn, eliminerar visserligen pilotföroreningen, men fördubblar samtidigt antalet nödvändiga pilotsignaler. Mot bakgrund av den redan existerande pilotsignalsproblematiken i RIS-baserade system behövs en annan lösning som inte ökar pilotbehovet. Därför undersöks här hur mottagarstrålformning och nollställning (null forming) kan användas för att eliminera pilotföroreningen. Vi visar att det är möjligt att undertrycka den oönskade signalen från den andra operatörens RIS genom att placera nulls mot den, och därmed undvika pilotförorening utan att öka antalet pilotsignaler.

I avhandlingens tredje del betraktas ett enoperatörssystem med två RIS:ar i en integrerad sensor- och kommunikationsmiljö (ISAC), där en enda användare fungerar både som kommunikationsenhet och positioneringsmål. Baserat på upplänkens positioneringspiloter försöker basstationen uppskatta både kommunikationskanalen och användarens position inomhus. Detta görs genom att först skatta infallsvinklar (AoA) på signalerna som träffar de två RIS:arna och därefter, med hjälp av system- och antenngeometrier, beräkna användarpositionen samt motsvarande kanaler. Trots att detta inte är ett multioperatörsscenario kan pilotförorening uppstå av samma fysiska skäl när flera RIS:ar används, såvida kanaluppskattningen inte parameteriseras. Eftersom kommunikationslänkarna här antas vara rena siktlänkar (LOS) kan man dock utnyttja kanalstrukturen för att minska antalet okända parametrar. Detta gör att informationsförlusten orsakad av pilotförorening inte påverkar kanaluppskattningen, och pilotföroreningen kan därmed överbryggas. Vidare bestäms användarens position genom att skära de räta linjerna som definieras av AoA-estimaten. Vi använder Cramér-Raos lägsta gräns (CRLB) som prestandamått för den lägsta möjliga medelkvadratfelet (MSE) för en skattning av både kanal och position. Numeriska resultat visar att det är fullt möjligt att utnyttja positioneringspiloter för parameterbaserad kanaluppskattning i LOS-scenarier.

I avhandlingens fjärde del förflyttar vi oss till närfältskommunikation, där användarna befinner sig i den s.k. Fresnelzonen relativt basstationens antennapertur. Vi analyserar ett uplänkscenario i ett fleranvändarsystem med flera antenner (MU-MIMO) och antar att kanalmodellen är närfältsbaserad och beror på användarnas avstånd och azimutvinkel relativt antennaperturen. Vi härleder CRLB för att i slutet uppskatta såväl positioneringsparametrar (avstånd och vinkel) som de parameteriserade kommunikationskanalerna i slutet form. Dessutom undersöker vi hur 2D-MUSIC-algoritmen kan användas för att skatta dessa parametrar, och vi jämför dess prestanda med CRLB. Resultaten visar att 2D-MUSIC är både asymptotiskt konsistent och effektiv för denna typ av närfältsbaserad kanaluppskattning.

Nyckelord: Omkonfigurerbar intelligent yta, kanaluppskattning, pilotkontaminering, positionering, uppskattning av ankomstvinkel, integrerad sensorik och kommunikation, mottagarens strålforming, strålande närfält.

List of Papers

1. ***Impact of Pilot Contamination Between Operators With Interfering Reconfigurable Intelligent Surfaces***
   Doğa Gürgünoğlu, Emil Björnson, Gábor Fodor
   IEEE International Black Sea Conference on Communications and Networking (2023)

2. ***Combating Inter-Operator Pilot Contamination in Reconfigurable Intelligent Surfaces Assisted Multi-Operator Networks***
   Doğa Gürgünoğlu, Emil Björnson, Gábor Fodor
   IEEE Transactions on Communications (2024)

3. ***Receive Beamforming Schemes to Mitigate Inter-Operator Pilot Contamination in RIS-Aided MIMO Networks***
   Doğa Gürgünoğlu, Ziya Gülgün, Emil Björnson, Gábor Fodor
   Signal Processing (submitted, under review)

4. ***Joint Pilot-Based Localization and Channel Estimation in RIS-Aided Communication Systems***
   Doğa Gürgünoğlu, Emil Björnson, Gábor Fodor
   IEEE Wireless Communications Letters (2024)

5. ***Performance Analysis of a 2D-MUSIC Algorithm for Parametric Near-Field Channel Estimation***
   Doğa Gürgünoğlu, Alva Kosasih, Parisa Ramezani, Özlem Tuğfe Demir, Emil Björnson, Gábor Fodor
   IEEE Wireless Communications Letters (submitted, under review)

Other contributions by the author not included in the thesis.

6. ***Deep Reinforcement Learning Based Joint Downlink Beamforming and RIS Configuration in RIS-aided MU-MISO Systems Under Hardware Impairments and Imperfect CSI***
   Baturay Sağlam, **Doğa Gürgünoğlu**, Süleyman S. Kozat
   IEEE International Conference on Communications (ICC) Workshops (2023)

7. ***Optimizing Pilot Spacing in MU-MIMO Systems Operating Over Aging Channels***

Sebastian Fodor, Gábor Fodor, **Doğa Gürgünoğlu**, Miklós Telek
IEEE Transactions on Communications (2023)

8. ***Power adaptation for vector parameter estimation according to Fisher information-based optimality criteria***
Doğa Gürgünoğlu, Berkan Dulek, Sinan Gezici
Signal Processing (2022)

9. ***Optimal Power Allocation for the Secure Estimation of Multiple Parameters***
Doğa Gürgünoğlu, Çağrı Göken, Sinan Gezici
IEEE Signal Processing Letters (2021)

Contributions to the Publications included in the Thesis

1. E.B. proposed the topic on a conceptual level. I formulated the system model and derived the estimators and the resulting estimation errors in closed form. Then, I developed the code to generate the numerical results. G.F. and E.B. helped me write the introduction significantly in finding related work and highlighting contributions that signify the article in terms of impact.

2. E.B. and G.F. identified the potential extensions to the conference paper. I derived the estimator in the Bayesian context and the capacity lower bound. G.F. and E.B. helped me in deriving the capacity bound. Then, I developed the code to generate the numerical results. G.F. and E.B. helped me write the introduction.

3. Z.G. proposed this research idea that receive beamforming might also eliminate inter-operator pilot contamination. I developed the theory and the source code to generate the numerical results, and wrote the article. E.B. & G.F. helped me refine the article text.

4. I proposed the topic and E.B. helped me put it into context. I developed the theory and the source code to generate the numerical results. G.F. and I worked together on the selection of numerical results, and E.B. & G.F. helped me write the introduction.

5. A.K. proposed the CRB analysis of his prior research on near-field parametric channel estimation. A.K. and P.R. worked on the development of the 2D-MUSIC algorithm. I developed the theory and code for CRB analysis, and wrote Sections I, IV, and V. G.F. and E.B. provided me with the resources to develop the CRB analysis, and Ö.T.D., G.F., and E.B. helped me refine the article text.

Acknowledgement

First, I would like to thank my supervisors Prof. Gábor Fodor and Prof. Emil Björnson for their valuable contributions, insights, and support throughout my doctoral studies. I believe that the most important backbone of a high-quality doctoral education is high-quality supervision, therefore, their effort in supervising me is invaluable.

I also would like to thank my master's supervisor Prof. Sinan Gezici for raising me as a self-conscious researcher with a strong background before my arrival to Sweden. To this day, the fundamental skills I obtained under his supervision still work in my favor as a researcher, and I find it much easier to adapt to the changing academic landscape thanks to him.

I would like to thank my collaborators Sebastian Fodor, Prof. Miklós Telek, Baturay Sağlam, and Prof. Süleyman Serdar Kozat for their cooperation in my academic ventures outside of my Ph.D.. I enjoyed collaborating with them and contributing to the literature together.

Then I would like to thank my invaluable friends, or rather, my companions. I would like to thank Alper Umut Uçar for being there for me at my darkest hour as always, I could not have survived my darkest times without his support. I would like to thank Çınar Yalçınduran for bearing with me through 12 long years as a close friend and tolerating my impulsive and sometimes annoying personality, and also for teaching me how to write my first line of code. I would like to thank Süleyman Taylan Topaloğlu for his inspirational comments on my research and his presence as a valuable friend. I would like to thank Can Soygür for always being at the other end of the phone whenever I needed, and for hosting me throughout my visits to Ankara. I would like to thank Onur Özder for his emotional support throughout my life in Sweden and for being online at the most unconventional hours, especially during winter. I would like to thank Ömer Deveer for his bare existence, he fueled my life energy whenever I ran short of it, and always had a thrilling story to tell. I would like to Çağdaş Öztekin for letting me accompany him through the streets of Södermalm and showing me evidence of life in Stockholm even at its dullest times. I would like to thank Nazlı Daşdemir for always supporting me even on my weirdest days. I would like to thank my friends Yamaç Ergiz, Abdallah Ghazi Faisal Zaid Alkilani, Ceyhun Emre Öztürk, Mustafa Bay, Bilge Selin Emre, Elif Nur Güngör, Ecem Karabay,

Ege Balcıoğlu, Ali Bahadır Alga, and Efkan Öz for always being there for me and giving me a good time. I would like to thank Asst. Prof. Özlem Tuğfe Demir for giving me useful advice whenever I needed it, and for being an inspiration for being a productive researcher. More importantly, I would like to thank her for being a great friend. I would like to thank Dr. Ziya Gülgün for his inspiring research ideas and his positive energy. I also would like to thank all my friends at the Decision and Control Systems & Communication Systems department, along with my valuable friends from the Ph.D. Chapter.

I would like to send my sincere thanks and love to my dearest fiancée and my soon-to-be wife Gizem Demir for being there for always being there for me and showing me the light of hope. I would not be able to cope with the hardships of this journey without her. Whenever I got lost in this seemingly endless journey, she reminded me that I was human and had a heart.

Last but not least, I would like to thank my parents. My mother Serap Gürgünoğlu, and my father Mehmet Feridun Gürgünoğlu. I would not be here today writing these lines if they had not supported me through the 27 long years of my life. I would like to thank my father Mehmet Feridun Gürgünoğlu for his highly reasonable advice, reassuring attitude, and for teaching me how to think like an engineer. I would like to thank my mother Serap Gürgünoğlu for her continuous support, her daily good morning texts, her good vision of raising me, and always listening to me on any topic. Just like how a high-quality doctoral education requires high-quality supervision, a high-quality life requires high-quality parenting.

Contents

Chapter 1

Introduction

Wireless communication is one of the key enablers of the modern world we live in. By facilitating the circulation of knowledge, it has enabled the globalization of our world. In the blink of an eye, it is possible to call a friend on the other side of the world, hear news from thousands of kilometers away, and access the most recent scientific articles on a browser. It is the technology that accelerates other technologies, it is the technology that made it possible to stay connected even when the world was in lockdown. It let the industry continue advancing throughout the pandemic, and it let lovers miles apart see and talk with each other, although through a phone or computer screen.

While the concept of wireless communication unites all technologies that use electromagnetic waves to carry information from one place to another, its subcategories are quite diverse. For example, both Digital Mobile Radio (DMR) and Bluetooth systems use electromagnetic waves to carry information and very similar dynamics apply to signal blockage, propagation, reflection, and penetration loss. On the other hand, their internal design and their ways of representing information in the form of signals are quite different. A mobile communication system, for example, is very different from both of the aforementioned technologies. This stems from the difference in use cases. Bluetooth operates on very short ranges and has much more relaxed throughput requirements, while a mobile communication system is much more throughput-intensive and demands much higher reliability.

1.1 Evolution of Mobile Communication Systems

Mobile communication systems evolved drastically since their dawn. While a mixture of fourth and fifth-generation networks (4G and 5G) are in use right now, they are markedly different from what 1G was back in the 80s. 1G was analog, and the cell phones were very bulky. It was not until 2G came out

that mobile phones started to communicate digitally and Short Message Service (SMS) became a reality. 3G made it possible to communicate at higher rates and integrate the internet into mobile devices. It was not until 4G that the mobile internet performance reached the level of WiFi since the internet service provided by 3G was too slow and unstable to provide a satisfactory user experience. With the introduction of 5G, mobile communications evolved into a technology that does not only serve human users. 5G was introduced with three concepts [1, Chapter 1.2.1]:

- **Enhanced Mobile Broadband (eMBB):** This concept covers the use cases where the aim is to provide the human user with immense data rates such as augmented reality (AR) and high-quality streaming.
- **Ultra-Reliable Low-Latency Communications (URLLC):** This concept covers the use cases where the aim is to transfer the data from one place to another with extremely high reliability and very low latency. These use cases are usually very sensitive to error, therefore, the use cases under this umbrella are usually referred to as "mission-critical applications", such as vehicular communications for autonomous driving and remote surgery.
- **Massive Machine-Type Communications (mMTC):** In massive Internet of Things (IoT) applications, there exists a high number of low-complexity and low-data rate devices in a very small area. Handling such massive connectivity requires very efficient cell management in applications such as autonomous factories and smart agriculture.

One of the key enablers of this amazing evolution of wireless communication systems is the massive multiple-input multiple-output (MIMO) technology [2, 3]. This technology came up with the idea of using multiple antennas to transmit and receive information over the air. It turned out that a MIMO channel was richer than its single input single output (SISO) counterpart, and this richness could be used to increase reliability by exploiting the channel's diversity and to increase data rates through the channel's ability to accommodate spatial multiplexing. Another phenomenon that massive MIMO systems enjoy is channel hardening [4]. When the number of antennas at either end of the channel increases, the normally stochastic channel becomes more and more deterministic and more communications-friendly. This not only enables more reliable communication at higher data rates but also facilitates signal processing. Another benefit of massive MIMO is its ability to serve multiple users at the same time and frequency resource by introducing the capability of spatial multiplexing.

As we live in the fast-paced world of the twenty-first century, the question of what 6G will be has already been raised even when 5G is not fully rolled out [5]. While the disparity between the vision and reality of 5G calls for the postponement of certain features to 6G, there still exist many ambitious goals to achieve,

some of which are considered far-fetched by today's technology. Consequently, a set of key enabling technologies of 6G became quite popular in academia and industry. One of these technologies is RISs.

Reconfigurable Intelligent Surfaces

RISs are envisioned to be periodic surfaces consisting of engineered elements whose electromagnetic properties are externally controllable and consume very little power [6]. In traditional MIMO, engineering efforts were directed towards finding the best way to transmit the signal from the transmitter and using the received signal in the smartest way possible at the receiver, given a propagation environment. RISs represent a paradigm change, mainly because by adjusting the phase difference between the incident and reflected waves, RISs provide partial control over the propagation environment.

Since RISs consist of multiple elements capable of shifting the phases of incident signals, it is possible to use RISs for beamforming. With the necessary CSI, RISs can align the phases of the multiple paths of the channel so that constructive interference occurs at the receiver, hence boosting the received signal's signal-to-noise ratio (SNR). This not only results in improved achievable rates but also extended coverage, that is, if the system has a certain SNR threshold to operate and the SNR would remain below at a certain location without the RIS, the presence of an RIS might boost the SNR to a level above the threshold to convert a dead zone into a live zone.

In addition, RISs can provide higher energy efficiency. If a certain receiver SNR is to be satisfied in a system, by using a RIS that consumes very low power, it is possible to boost the channel gain to decrease the transmit power requirement. This gain is particularly important for IoT devices since they are usually battery-operated and have simpler power amplifiers.

There are various technologies considered to fabricate RISs. Tunable dielectric materials, for example, exhibit some tunable electromagnetic properties such as permittivity and permeability upon being subjected to external stimuli such as electric and magnetic fields, and changing temperature. Controllable electromagnetic properties make these materials a candidate technology to make RIS a reality [7]. A closely related candidate technology is the use of micro-electromechanical systems (MEMSs). Consisting of miniature electromechanical devices, MEMS-based RIS elements can be designed to alter their geometries, hence their electromagnetic properties.

In the literature, metamaterial-based RISs are quite popular. The prefix "meta" for these artificial materials stands for the fact that these materials exhibit properties that are not present in natural materials. This is achieved by periodi-

cally arranging resonant structures with sub-wavelength spacing. RISs produced through metamaterials can be used to control the phase, amplitude, and polarization of the reflected wave. This not only opens up a new set of possibilities but also brings the necessity of accurate electromagnetic models for the RISs. While the electromagnetic properties of reflecting surfaces are studied such as in [8, 9], full integrity between the domains of electromagnetism and wireless communications is yet to be established since the wireless communications literature still uses the same models for RISs as those used for modeling antenna arrays.

Given the diversity of techniques in producing RISs, the diversity in RIS features is no big surprise. One of the most popular comparisons among the different kinds of RISs is the active RIS and the passive RIS. As the names suggest, passive RISs operate on low power and change the phases of incident waves. Active RISs, on the other hand, consist of elements capable of amplifying and attenuating incident waves in addition to changing their phases. While passive RISs have the advantage of very low power consumption and hence the capability of drastically increasing the energy efficiency of the system, they face the problem of multiplicative path loss. Since passive RISs do not amplify the incident wave that has already experienced path loss, the reflected wave experiences path loss once again until it reaches its target. It is still argued that the multiplicative path loss is counteracted by the SNR boost introduced by the RIS, however, depending on the propagation conditions, this might require a huge number of RIS elements which complicates processes such as channel estimation and optimizing the RIS configuration.

Active RISs, on the other hand, have the power of amplification and perform better at combating the multiplicative path loss phenomenon [10]. However, due to the power amplifiers they possess, they introduce amplifier noise to the propagating wave. On top of this, due to the higher power consumption compared to passive RISs, active RISs might not boost the energy efficiency of the system as much.

1.2 Theoretical Background

This thesis is highly focused on statistical signal processing. Statistical signal processing is a sub-area of signal processing where the processed signals contain any kind of randomness. That is, signals corrupted by noise, signals with non-deterministic time/frequency variations, random variables, random vectors, and random processes are all within the scope of statistical signal processing. In statistical signal processing, problems based on detection and estimation come up ubiquitously. For certain problems, we know that there exist 2 or more possible true states of nature. Based on our observation of nature, we formulate these possible true states as hypotheses, and we test our observation against our hy-

potheses to determine the true state of nature. These kinds of problems are called detection problems. On the other hand, we might also want to determine a quantity buried in nature based on our observation, which is called estimation. We provide some theoretical background on detection and estimation in the following subsections.

In addition to detection and estimation theory, we will also need some tools regarding MIMO processing at the receiver side. Having multiple antennas at the receiver creates multiple options for receiver signal processing. These options include focusing on maximizing the power received from the intended signal, eliminating interference, or maintaining a balance between the two objectives. We provide some background on this in the following subsections.

We also require some background on an algorithm called Multiple signal classification (MUSIC). Introduced in [11], the MUSIC algorithm characterizes multiple parameters associated with multiple signals by separating the observation into signal and noise subspaces. Assuming that the number of signals is known, this algorithm uses the signal-noise orthogonality by creating peaks at certain parameter values. We provide more details in the following subsections.

Detection Theory

In detection problems, the common element is that we have two or more hypotheses, and based on observation, we decide among two or more possible situations [12, Chapter II.A]. We can put the hypothesis testing problems into three categories involving simple hypothesis testing, and a fourth category involving composite hypothesis testing:

- **Bayesian Hypothesis Testing:** In this framework, the hypotheses' prior probabilities of occurrence are considered to be known, and the state of nature is considered to be a discrete random variable. For a binary hypothesis testing problem, for example, the state of nature is considered to be a Bernoulli random variable [12, Chapter II.B]. In such problems, the cost of declaring hypothesis A while the truth is B is known, and based on this knowledge and the prior distribution, the Bayes risk is formulated and the decision rule minimizing this risk is called the Bayes decision rule. Now let us provide a simple binary hypothesis testing formulation.

  Let $\mathcal{H}_0$ and $\mathcal{H}_1$ denote the null and alternative hypotheses with prior probabilities p_0 and $p_1 = 1 - p_0$. Let $C_{ij} \geq 0$ denote the cost of choosing hypothesis i while the true hypothesis is j. Let the observation Y reside within the set Γ, and δ be the decision rule partitioning Γ into Γ_0 and Γ_1. Denoting $P_j(\Gamma_i) \triangleq P(Y \in \Gamma_i | \mathcal{H}_j)$, we can define the conditional risk as

$$R_j(\delta) = C_{1j} P_j(\Gamma_1) + C_{0j} P_j(\Gamma_0). \tag{1.1}$$

Then using the prior probabilities, we can define the Bayes risk:

$$r(\delta) = p_0 R_0(\delta) + p_1 R_1(\delta) \tag{1.2}$$

$$\delta_B = \arg\min_{\delta} r(\delta), \tag{1.3}$$

where δ_B minimizing $r(\delta)$ over all rules is called the *Bayes rule*. To determine the Bayes rule, it is possible to rewrite (1.2) as

$$\begin{aligned} r(\delta) &= \sum_{j=0}^{1} p_j R_j(\delta) = \sum_{j=0}^{1} p_j [C_{1j} P_j(\Gamma_1) + C_{0j} (\underbrace{1 - P_j(\Gamma_1)}_{P_j(\Gamma_0)})] \\ &= \sum_{j_0}^{1} p_j C_{0j} + \sum_{j_0}^{1} p_j (C_{1j} - C_{0j}) P_j(\Gamma_1) \\ &= \sum_{j_0}^{1} p_j C_{0j} + \int_{\Gamma_1} \left[\sum_{j_0}^{1} p_j (C_{1j} - C_{0j}) p_j(y) \right] dy. \end{aligned} \tag{1.4}$$

If we choose Γ_1 as follows, we minimize $r(\delta)$ over all $\Gamma_1 \subseteq \Gamma$:

$$\begin{aligned} \Gamma_1 &= \left\{ y \in \Gamma : \sum_{j=0}^{1} p_j (C_{1j} - C_{0j}) p_j(y) \leq 0 \right\} \\ &= \{ y \in \Gamma : p_1 (C_{11} - C_{01}) \leq p_1 (C_{00} - C_{10}) 0 \}. \end{aligned} \tag{1.5}$$

Making the reasonable assumption $C_{11} < C_{01}$, we obtain Γ_1 as follows:

$$\tau \triangleq \frac{p_0 (C_{10} - C_{00})}{p_1 (C_{01} - C_{11})}, \quad \Gamma_1 = \{ y \in \Gamma : p_1(y) \geq \tau p_0(y) \}. \tag{1.6}$$

This result leads to the *likelihood ratio test*:

$$L(y) = \frac{p_1(y)}{p_0(y)} \lessgtr \tau. \tag{1.7}$$

If $L(y) < \tau$, we choose $\mathcal{H}_0$ we choose $\mathcal{H}_1$ if $L(y) > \tau$, giving us the Bayes rule. In communication applications, special cases of this apply. These can be listed as follows:

– **Uniform Cost Assignment (UCA):** If we consider symbol decoding, the kind of error we make is not important, we either decode it correctly or incorrectly. Consequently, this cost assignment is used in communication applications:

$$C_{ij} = \begin{cases} 0 & i = j \\ 1 & i \neq j \end{cases}. \tag{1.8}$$

– **Equal Priors:** In both binary and M-ary hypothesis testing scenarios, we get a huge volume of data with high diversity. Consequently, we end up with having equally likely symbols, that is, $p_j = \frac{1}{M}$ where M is the number of possible outcomes.

For generic priors and uniform cost assignment, the Bayes rule is called the *Maximum a posteriori (MAP)* rule. Furthermore, if there are equal priors, it is called the *maximum likelihood (ML)* rule.

- **Minimax Hypothesis Testing:** In this framework, the prior probabilities are unknown. The aim is to minimize the maximum of the conditional risks. It is proven that an "equalizer rule", a rule that equates all conditional risks, solves the minimax problem, details of which are discussed in this section. The most compact formulation of the minimax rule δ_M can be expressed as

$$\delta_M = \arg\min_{\delta}(\max(R_0(\delta), R_1(\delta))). \tag{1.9}$$

Since the priors are unknown, we can consider the Bayes rule as a function of δ and p_0:

$$r(p_0, \delta) = p_0 R_0(\delta) + (1 - p_0) R_1(\delta), \tag{1.10}$$

which is maximized at either $p_0 = 0$ or $p_0 = 1$. Suppose δ_{p_0} is the Bayes rule for the prior p_0. Since there is one unique Bayes rule for each value of p_0, we essentially have a single variable. Hence we can define

$$V(p_0) = r(p_0, \delta_{p_0}) \tag{1.11}$$

$$V(0) = C_{11}, \quad V(1) = C_{00}. \tag{1.12}$$

Now let us define $p_L \triangleq \arg\max_{p_0} V(p_0)$, the least favorable prior. The minimax decision rule is the Bayes rule for the least favorable prior. An intuitive proof of this can be made as follows:

– If $p_0' < p_L$, then $\max(R_0(\delta_(p_0')), R_1(\delta_(p_0'))) = R_0(\delta_(p_0') > R_0(\delta_(p_L))$
– If $p_0' > p_L$, then $\max(R_0(\delta_(p_0')), R_1(\delta_(p_0'))) = R_1(\delta_(p_0') > R_1(\delta_(p_L))$,

hence δ_{p_L} outperforms all Bayes rules in the minimax sense.

- **Neyman-Pearson Hypothesis Testing:** In this framework, we consider binary hypothesis testing problems. In many detection problems, we cannot associate a solid cost structure with risks. In such cases, we consider the probability of a certain kind of error to happen. In binary hypothesis testing, we have two types of errors: false alarm (type 1) and miss (type 2). A Neyman-Pearson detector usually places a constraint on the probability of false alarm and aims to maximize the detection probability. We denote this as

$$\max_{\delta} P_D(\delta) \quad \text{s.t.} \quad P_F(\delta) \leq \alpha, \tag{1.13}$$

where $P_D(\delta)$ and $P_F(\delta)$ denote the detection and false-alarm probabilities for the decision rule δ and α is called the significance level of the test. We denote the miss probability as $P_M(\delta) = 1 - P_D(\delta)$, however, this framework mostly considers detection probability maximization. Based on the observation y, suppose we formulate the decision rule as

$$\delta(y) = \begin{cases} 1 & y \in \Gamma_1 \\ 0 & y \in \Gamma_0 \end{cases}. \tag{1.14}$$

If we condition the decision rule output on the null hypothesis, we can obtain the false alarm probability/rate:

$$\begin{aligned} P_F(\delta) &= P(y \in \Gamma_1 | \mathcal{H}_0) = \int_{y \in \Gamma_1} p_0(y) dy = \int_{y \in \Gamma} p_0(y) dy \\ &= \mathbb{E}[\delta(y) | \mathcal{H}_0] \triangleq \mathbb{E}_0[\delta(y)]. \end{aligned} \tag{1.15}$$

As for the detection probability we have

$$\begin{aligned} P_D(\delta) &= P(y \in \Gamma_1 | \mathcal{H}_1) = \int_{y \in \Gamma_1} p_1(y) dy = \int_{y \in \Gamma} p_1(y) dy \\ &= \mathbb{E}[\delta(y) | \mathcal{H}_1] \triangleq \mathbb{E}_1[\delta(y)]. \end{aligned} \tag{1.16}$$

The following lemma, known as the Neyman-Pearson Lemma establishes the fundamentals of Neyman-Pearson hypothesis testing:

Lemma 1. ***Neyman-Pearson Lemma:*** *For a binary hypothesis testing with $\alpha > 0$, the following hold:*

Optimality: *Let $\tilde{\delta}$ be any decision rule satisfying $P_F(\delta) \leq \alpha$ and let $\tilde{\delta}'$ be any decision rule of the form*

$$\tilde{\delta}(y) = \begin{cases} 1 & p_1(y) > \eta p_0(y) \\ \gamma(y) & p_1(y) = \eta p_0(y) \\ 0 & p_1(y) < \eta p_0(y) \end{cases}, \tag{1.17}$$

where $\eta \geq 0$ and $\gamma(y) \in [0, 1]$ are such that $P_F(\tilde{\delta}) = \alpha$. Then $P_D(\tilde{\delta}') \geq P_D(\tilde{\delta})$. That is, any decision in the form of (1.17) is a Neyman-Pearson (NP) rule.

Existence: *For every $\alpha \in (0, 1)$, there exists a Neyman-Pearson rule in the form (1.17).*

Uniqueness: *Suppose that δ'' is any α-level NP decision rule. Then, δ'' must be of the form (1.17) except possibly on a subset of Γ having zero probability under $\mathcal{H}_0$ or $\mathcal{H}_1$.*

Proof. The proof of the Neyman-Pearson Lemma can be found in [12, Proposition II.D.1]. □

- **Composite Hypothesis Testing:** So far, we have discussed the aspects of simple hypothesis testing, that is, we had a single possible distribution for each hypothesis. On the other hand, there exist many problems where there are multiple possible distributions for each hypothesis. It is quite common that the distributions of the hypotheses depend on one or more parameters that have their own distributions. Such hypothesis testing problems are called *composite hypothesis testing* problems. We can provide a simple radar detection problem as an example for this:

$$\mathcal{H}_0 : y(t) = n(t)$$
$$\mathcal{H}_1 : y(t) = As(t-\tau) + n(t),$$

where $\mathcal{H}_0$ is a simple hypothesis and $\mathcal{H}_1$ is a composite hypothesis depending on the set of parameters $\boldsymbol{\theta} = \begin{bmatrix} A & \tau \end{bmatrix}^T$.

Bayesian Formulation: Let $\Theta \in \Lambda$ be the parameter or the set of parameters governing the hypothesis testing problem. We consider Θ to be a random variable taking values within Λ. We partition this set into Λ_0 and Λ_1, over which Θ resides when $\mathcal{H}_0$ and $\mathcal{H}_1$ are true, respectively. Let $p_\theta(y)$ be the conditional distribution of y given that the parameter takes the value $\Theta = \theta$.

Cost function: $C[i, \theta]$, denoting the cost when $y \sim p_\theta$, and $i \in \{0, 1\}$.

Conditional risk: $R_\theta(\delta) = \mathbb{E}[C[\delta(Y), \theta] | \Theta = \theta]$

Bayes Risk: $r(\delta) = \mathbb{E}_\theta[R_\theta(\delta)]$. Bayes rule is the δ that minimizes $r(\delta)$.

Neyman-Pearson Formulation: We do not consider any prior distributions for the hypotheses here. False alarm and detection probabilities are denoted as

$$P_F(\tilde{\delta}; \theta) = \mathbb{E}_\theta[\tilde{\delta}(y)], \quad \theta \in \Lambda_0 \tag{1.18a}$$
$$P_D(\tilde{\delta}; \theta) = \mathbb{E}_\theta[\tilde{\delta}(y)], \quad \theta \in \Lambda_1. \tag{1.18b}$$

While we do not go into the details in this thesis, there are two important tests in the composite Neyman-Pearson formulation:

  - **Uniformly Most Powerful (UMP) Test:** This test maximizes P_D for for all $\theta \in \Lambda_1$ such that $P_F \leq \alpha$ for all $\theta \in \Lambda_0$
  - **Locally Most Powerful (LMP) Test:** Suppose that $\mathcal{H}_0 : \Theta = \theta_0$ and $\mathcal{H}_1 : \theta > \theta_1$. Consider the cases where Θ takes values very close to θ_0, for example, in weak signal detection problems. We take a Taylor series expansion around θ_0:

$$P_D(\tilde{\delta}; \theta) = \underbrace{P_D(\tilde{\delta}; \theta_0)}_{P_F(\tilde{\delta})} + (\theta - \theta_0) P'_D(\tilde{\delta}; \theta_0) + \underbrace{O((\theta - \theta_0)^2)}_{\text{rest of the terms}} \tag{1.19}$$

$$P_D(\tilde{\delta}; \theta) \approx \alpha + (\theta - \theta_0) P'_D(\tilde{\delta}; \theta_0) \tag{1.20}$$

.

From this approximation, it is possible to choose $\tilde{\delta}$ to maximize $P'_D(\tilde{\delta};\theta_0)$, resulting in a locally optimal test.

Estimation Theory

Estimation theory specializes in determining the value of an unknown parameter as accurately as possible. Depending on whether prior information on the parameter is available or not, we consider two different frameworks: Bayesian parameter estimation where the parameter is a random variable with a known prior distribution, and non-random parameter estimation where the parameter does not exhibit any probabilistic structure and is considered to be deterministic.

- **Bayesian Parameter Estimation:** Consider a random observation $Y \in \Gamma$, whose distribution depends on a random parameter $\Theta \in \Lambda$, that is $Y \sim P_\theta$. The aim is to observe Y and find a function $\hat{\theta} : \Gamma \mapsto \Lambda$ such that $\hat{\theta}(y)$ is the best guess of θ.

  The natural question at this point would be: "Best in what sense?". To determine an optimality criterion, we define a cost function.

  - For $C : \Lambda \times \Lambda \mapsto \mathbb{R}_+$, $C[a,\theta]$ denotes the cost of estimating θ as a.
  - The conditional risk discussed in detection theory can be defined here as $R_\theta(\hat{\theta}) \triangleq \mathbb{E}[C[\hat{\theta}(Y),\Theta]|\Theta = \theta]$.
  - As a result, the corresponding Bayes risk becomes $r(\theta) = \mathbb{E}_\theta[R_\theta(\hat{\theta})]$. The Bayesian estimator minimizes the Bayes risk.

  Using the law of iterated expectations, the Bayes risk can be rewritten as

$$\begin{aligned} r(\theta) &= \mathbb{E}_\theta[\mathbb{E}[C[\hat{\theta}(Y),\Theta]|\Theta]] \\ &= \mathbb{E}_\theta[\mathbb{E}[C[\hat{\theta}(Y),\Theta]] \\ &= \mathbb{E}_\theta[\mathbb{E}[C[\hat{\theta}(Y),\Theta]|Y]]. \end{aligned} \tag{1.21}$$

  Hence the Bayesian estimator minimizes the *posterior cost*. Many of the well-known Bayesian estimators differ by the considered cost function, which can be specified as follows:

  - Minimum mean squared error (MMSE) Estimator: $C[a,\theta] = (a-\theta)^2$
  - Minimum mean absolute error (MMAE) Estimator: $C[a,\theta] = |a-\theta|$
  - MAP Estimator: Uniform cost function: $C[a,\theta] = \begin{cases} 0 & |a-\theta| \leq \Delta \\ 1 & |a-\theta| > \Delta \end{cases}$ for some $\Delta > 0$.

  MMSE Estimator: In this case, the Bayes risk is

$$r(\theta) = \mathbb{E}[(\hat{\theta}(Y) - \theta)^2]. \tag{1.22}$$

We can express the posterior cost as

$$\begin{aligned}\mathbb{E}[(\hat{\theta}(Y)-\Theta)^2|Y=y] &= \mathbb{E}[(\hat{\theta}(Y))^2|Y=y] - 2\mathbb{E}[\hat{\theta}(Y)\Theta|Y=y] + \mathbb{E}[\Theta^2|Y=y] \\ &= (\hat{\theta}(y))^2 - 2\hat{\theta}(y)\mathbb{E}[\Theta|Y=y] + \mathbb{E}[\Theta^2|Y=y]. \quad (1.23)\end{aligned}$$

This is a quadratic polynomial in $\hat{\theta}(y)$, hence we can find the minimum of this point as

$$\begin{aligned}&\frac{\partial}{\partial\hat{\theta}(Y)}\mathbb{E}[(\hat{\theta}(Y)-\Theta)|Y=y] = 2\hat{\theta}(y) - 2\mathbb{E}[\Theta|Y=y] = 0 \\ &\hat{\theta}_{\text{MMSE}}(y) = \mathbb{E}[\Theta|Y=y]. \quad (1.24)\end{aligned}$$

Therefore, another name for the MMSE estimator is the *conditional mean estimator*.

MAP Estimator: In this case, the posterior cost can be expressed as

$$\begin{aligned}\mathbb{E}[C[\hat{\theta}(Y),\Theta]|Y=y] &= P(|\hat{\theta}(Y)-\Theta|>\Delta|Y=y) \\ &= 1 - P(|\hat{\theta}(Y)-\Theta|\leq\Delta|Y=y). \quad (1.25)\end{aligned}$$

Hence, the above expression is minimized when $P(|\hat{\theta}(Y)-\Theta|\leq\Delta|Y=y)$ is maximized. For small Δ and a smooth posterior distribution $w(\theta|y)$, this is maximized by

$$\hat{\theta}_{\text{MAP}}(y) = \arg\max_{\theta} w(\theta|y). \quad (1.26)$$

For discrete Θ, this corresponds to Bayesian M-ary hypothesis testing with uniform cost assignment. Since the MAP estimator maximizes the posterior density/probability, it is also known as *conditional mode estimator*. Note that using the Bayes rule, we can obtain

$$w(\theta|y) = \frac{p_\theta(y)w(\theta)}{p(y)}, \quad (1.27)$$

and also note that $p(y)$ does not depend on θ. Therefore, (1.26) can be expressed as

$$\hat{\theta}_{\text{MAP}}(y) = \arg\max_{\theta} p_\theta(y)w(\theta). \quad (1.28)$$

- **Non-random Parameter Estimation:** Contrary to the Bayesian parameter estimation framework, non-random parameter estimation framework considers the problems where the available prior information is insufficient. One of the most widely known estimators in this framework is the ML estimator, which acts like the non-random framework counterpart of the Bayesian MAP estimator in (1.28) without the prior distribution $w(\theta)$:

$$\hat{\theta}_{\text{ML}}(y) = \arg\max_{\theta} p_\theta(y). \quad (1.29)$$

Cramér-Rao Lower Bound (CRLB)

To evaluate the performance of an estimator, using lower bounds on its variance is essential. To this end, we introduce the CRLB, which provides a lower bound for the variance of any unbiased estimator. In its vector form, one can express the CRLB as

$$\mathbb{E}[(\hat{\boldsymbol{\theta}}(\mathbf{y}) - \boldsymbol{\theta})(\hat{\boldsymbol{\theta}}(\mathbf{y}) - \boldsymbol{\theta})^H] \succeq \mathbf{I}^{-1}(\mathbf{y}; \boldsymbol{\theta}), \tag{1.30}$$

where $\mathbf{I}(\mathbf{y}; \boldsymbol{\theta})$ denotes the Fisher Information Matrix (FIM), which is defined as

$$\mathbf{I}(\mathbf{y}; \boldsymbol{\theta}) \triangleq \mathbb{E}\left[\left(\frac{\partial}{\partial \boldsymbol{\theta}} \log p_{\boldsymbol{\theta}}(\mathbf{y})\right)\left(\frac{\partial}{\partial \boldsymbol{\theta}} \log p_{\boldsymbol{\theta}}(\mathbf{y})\right)^H\right]. \tag{1.31}$$

Receive Beamforming for MIMO Systems

Having multiple antenna elements has proven to be advantageous for both transmission and reception in wireless communication systems [13]. Benefits such as channel hardening, multiplexing, and diversity are the fundamental ideas behind massive MIMO systems. Among these ideas, we will focus on receive beamforming in this section. First, let's consider the uplink of a generic MIMO system with K single-antenna users and M receiver antennas. Then the system model becomes

$$\mathbf{y} = \mathbf{H}\mathbf{x} + \mathbf{w} \in \mathbb{C}^{M \times 1}, \tag{1.32}$$

where $\mathbf{x} = \begin{bmatrix} x_1 & x_2 & \dots & x_K \end{bmatrix}^T \in \mathbb{C}^{K \times 1}$ denotes the ensemble of signals transmitted by the K users, $\mathbf{H} \in \mathbb{C}^{M \times K}$ denotes the uplink MIMO channel, and $\mathbf{w}, \mathbf{y} \in \mathbb{C}^{M \times 1}$ denote the additive noise and the received signal vectors at the base station, respectively.

Maximum Ratio (MR)

MR processing focuses on capturing the maximum amount of power from the intended signal without taking interference into consideration. In the context of the system model we have provided, the combining matrix $\mathbf{V}^{MR} = \mathbf{H}^H \in \mathbb{C}^{K \times M}$. Hence the combiner output becomes

$$\tilde{\mathbf{y}}^{MR} = \mathbf{V}^{MR}\mathbf{y} = \mathbf{H}^H\mathbf{H}\mathbf{x} + \mathbf{H}^H\mathbf{w} \in \mathbb{C}^{K \times 1}. \tag{1.33}$$

Zero Forcing (ZF)

While MR focuses on capturing as much power as possible from the signal of interest, ZF focuses on eliminating the interference. To this end, ZF utilizes the pseudoinverse of the channel, that is, $\mathbf{V}^{ZF} = (\mathbf{H}^H\mathbf{H})^{-1}\mathbf{H}^H \in \mathbb{C}^{K \times M}$. This results in the combiner output

$$\tilde{\mathbf{y}}^{ZF} = \mathbf{x} + (\mathbf{H}^H\mathbf{H})^{-1}\mathbf{H}^H\mathbf{w} \in \mathbb{C}^{K \times 1}. \tag{1.34}$$

Multiple Signal Classification: A Subspace-based Method to Estimate Parameters

In this section, we focus on the MUSIC algorithm introduced in [11]. This algorithm resolves distinct transmitted signals from a noisy observation that contains a combination of these signals. This algorithm was originally developed to estimate the angle of arrivals (AoAs) of multiple signals impinging on an antenna array. Then, it has been used for more generic parameter estimation problems in contexts where the observation is a combination of these parameters. For example, in [14], a MUSIC algorithm with higher dimensionality is used to estimate not only the azimuth and elevation AoA, but also the distance between the transmitter and the receiver. For clarity, however, we shall consider a far-field system model with a uniform linear array (ULA) receiver consisting of N antennas and $K \leq N$ impinging signals. The signal received at a single time instant l can be expressed as

$$\underbrace{\begin{bmatrix} y_1[l] \\ y_2[l] \\ \vdots \\ y_N[l] \end{bmatrix}}_{\triangleq \mathbf{y}[l]} = \underbrace{\begin{bmatrix} \mathbf{a}(\theta_1) & \mathbf{a}(\theta_2) & \dots & \mathbf{a}(\theta_K) \end{bmatrix}}_{\triangleq \mathbf{A}(\boldsymbol{\theta})} \underbrace{\begin{bmatrix} s_1[l] \\ s_2[l] \\ \vdots \\ s_K[l] \end{bmatrix}}_{\triangleq \mathbf{s}[l]} + \underbrace{\begin{bmatrix} w_1[l] \\ w_2[l] \\ \vdots \\ w_N[l] \end{bmatrix}}_{\triangleq \mathbf{w}[l]}, \tag{1.35}$$

where θ_k is the azimuth AoA of the k-th impinging signal, s_k is a complex quantity denoting the combined effects of the transmitted signal and the propagation channel for the k-th signal, and $\mathbf{w}[l] \sim \mathcal{CN}(\mathbf{0}, \mathbf{I}_N)$ is the additive noise at the receiver. $\mathbf{a}(\theta_k)$ is the array response for the k-th signal with the azimuth AoA θ_k. After this step, the MUSIC algorithm considers the covariance matrix of $\mathbf{y}[l]$, which is realized by taking the sample covariance matrix of $\mathbf{y}[l]$ over L transmissions, that is,

$$\mathbf{R}_{\mathbf{y}} = \frac{1}{L} \sum_{l=1}^{L} \mathbf{y}[l]\mathbf{y}[l]\mathbf{y}^H[l]. \tag{1.36}$$

Assuming that there are sufficiently many samples and the signal & noise are independent, we state $\tilde{\mathbf{R}}_{\mathbf{y}}$ as

$$\mathbf{R}_{\mathbf{y}} = \mathbf{A}(\boldsymbol{\theta})\tilde{\mathbf{S}}\mathbf{A}^H(\boldsymbol{\theta}) + \sigma_w^2 \mathbf{I}_N, \tag{1.37}$$

where the signal component has rank K. Among the N eigenvectors of $\mathbf{R}_{\mathbf{y}}$, the span of those associated with the K largest eigenvalues is considered to be the signal subspace, and the span of the remaining $N - K$ eigenvectors is considered to be the noise subspace. From here, we can construct a matrix $\mathbf{U}_n \in \mathbb{C}^{N \times (N-K)}$ containing the eigenvectors belonging to the latter category. Recall that our aim is to find the K signals that are buried inside our observation. Since those K signals

are within the signal subspace, they must be orthogonal to all noise eigenvectors. For a given $\hat{\theta}$, we know that the signal is supposed to be $\mathbf{a}(\hat{\theta})$. Therefore, if we compute

$$S(\hat{\theta}) = \frac{1}{\mathbf{a}^H(\hat{\theta})\mathbf{U}_n\mathbf{U}_n^H\mathbf{a}(\hat{\theta})}, \tag{1.38}$$

then we will obtain a very large value for $\hat{\theta} \in \{\theta_1, \ldots, \theta_K\}$. By ensembling the values obtained from this computation, the MUSIC spectrum is constructed, and the K AoA values are obtained by peak detection.

1.3 Open Problems in RIS-Aided Wireless Communication Systems

Despite the potential of RIS as a 6G-enabling technology, it does not come without its problems. Even the comparison between active RISs and passive RISs shows that RISs not only have their problems but also introduce a plethora of system-level problems. First of all, configuring the RIS based on CSI requires a mid-haul link with the Radio Access Network (RAN). Over this link, the frequency of updating the RIS configuration also becomes a question. While updating the RIS configuration frequently over time improves the system's resilience against channel aging, frequent updates put a load on the mid-haul link between the RAN and the RIS. In addition, RIS multiplicatively increases the channel dimensions, that is, the cascaded channel's dimension is equal to the dimension of the end-to-end channel multiplied by the number of RIS elements. To use the RIS efficiently, all dimensions of the channel have to be explored. As a result, more pilots have to be transmitted, which decreases spectral efficiency.

Another problem is that as the requirement for frequent deployment increases, multiple operators start to share sites and in an RIS-aided future cellular/cell-free network, the operators' RISs will most likely be close to each other as well. As a result, the transmissions from users subscribed to a certain operator will also reflect through another operator's RIS and this unintended reflection will reach the BS as well, causing interference. Moreover, during the channel estimation phase, both operators will use sequences of pilot RIS configurations, and since these sequences will most likely be defined on the 3$^{\text{rd}}$ Generation Partnership Project (3GPP) standards, the operators might pick the same sequence. A user's uplink pilot transmission goes through not only its operator's RIS but also through the foreign operator's RIS. Effectively, the second undesired path acts as another virtual user using the same pilot sequence and the same RIS configuration. Consequently, a new kind of pilot contamination takes place, which can be called "multi-RIS pilot contamination" in the most general sense, and in a multi-operator setting, this can be called "inter-operator pilot contamination". This phenomenon was introduced in [15] and its statistical analysis was performed in [16]. This thesis focuses on this new kind of pilot contamination. To combat a newly discovered adverse phenomenon via signal processing-based

approaches, it is crucial to characterize the phenomenon mathematically. To this end, we introduce a simple multi-operator setup consisting of two single-antenna base stations, two N-element RISs, and two single-antenna users each subscribed to a different operator. In such a setup, we construct a received signal model and a misspecified signal model, the latter ignoring the transmission through the foreign RIS. We consider two cases: in the first case, the operators adopt the same sequence of RIS configurations to explore the different dimensions of the channel. In the second case, the operators double the number of transmitted pilots and choose orthogonal sequences of RIS configurations.

In the following section, the thesis outline and each chapter's contribution are explained.

1.4 Thesis Outline and Contributions

Chapter 2

In this chapter, we introduce the multi-RIS pilot contamination phenomenon. In a two-operator, two-RIS, and two-user setting, we demonstrate how multi-RIS pilot contamination arises and demonstrate why this cannot be avoided by pilot signal design. We assume that the RIS-BS channels are deterministic and known, and the user-RIS channels are deterministic and unknown. We demonstrate that doubling the pilot length and using orthogonal RIS configuration sequences resolve the problem, however, this causes a significant increase in the pilot sequence length. We analytically characterize the multi-RIS pilot contamination and show that for a deterministic estimator, this appears as an estimation bias term during the channel estimation phase. While the RISs are configured based on the channel estimates, the data transmission phase also shows that a significant degradation happens during data signal equalization due to the degraded channel estimation performance due to multi-RIS pilot contamination. This chapter is based on the following article:

- **Doğa Gürgünoğlu**, Emil Björnson, Gábor Fodor, Impact of Pilot Contamination Between Operators With Interfering Reconfigurable Intelligent Surfaces, *IEEE International Black Sea Conference on Communications and Networking 2023*, 2023.

Chapter 3

In this chapter, we extend our analysis in Chapter 2 into stochastic channels where we consider correlated Rayleigh fading. We derive the misspecified MMSE estimator for the user equipment (UE)-RIS channels and derive the resulting channel estimation mean squared error (MSE) in closed form. In the case of stochastic channels, the multi-RIS pilot contamination effect appears as an additive noise term. Based on the imperfect CSI obtained in the channel estimation phase, also

derive the capacity lower bound [13, Eq. 2.46] and compare it against the ergodic capacity of the channel. Our numerical results show that multi-RIS pilot contamination and lack of awareness of the unintended reflection significantly decrease the capacity lower bound. This chapter is based on the following article:

- **Doğa Gürgünoğlu**, Emil Björnson, Gábor Fodor, Combating Inter-Operator Pilot Contamination in Reconfigurable Intelligent Surfaces Assisted Multi-Operator Networks, *IEEE Transactions on Communications*, 2024.

Chapter 4

In this chapter, we revisit the problem of inter-operator pilot contamination that we have considered in Chapters 2 and 3. This time, we consider a multi-antenna base station that is capable of receive beamforming. We explore the use of this capability to eliminate inter-operator pilot contamination in multi-operator multi-RIS systems. To this end, we first demonstrate how inter-operator pilot contamination arises even when there is no model misspecification (as opposed to the system setup in Chapters 2 and 3). Then, we consider three different schemes, one of which is the baseline scheme. In the baseline scheme, we consider maximum ratio combining (MRC) at the BS focused on absorbing maximal power from the operator's own RIS and do not orthogonalize the RIS configurations. That is, inter-operator pilot contamination is not eliminated at either the BS or the RIS. In Scheme 1, we eliminate inter-operator pilot contamination at the RISs by orthogonalizing the configurations during the pilot transmission case. However, this comes with the price of doubling the number of pilots transmitted over time. In Scheme 2, the BS cuts off the signals coming from the other operator's RIS by null forming and hence eliminating inter-operator pilot contamination. In this chapter, we compare these schemes in terms of channel estimation and data transmission performance.

- **Doğa Gürgünoğlu**, Ziya Gülgün, Emil Björnson, Gábor Fodor, Joint Pilot-Based Localization and Channel Estimation in RIS-Aided Communication Systems, *Submitted to Signal Processing*, 2025.

Chapter 5

In this chapter, we consider a physical setup similar to that in Chapters 2 and 3, however, with a single operator. While the proposed solution to overcome the multi-RIS pilot contamination in Chapters 2 and 3 involved doubling the number of pilot transmissions, we propose a more effective method to combat the multi-RIS pilot contamination by exploiting the channel geometry, that is, parameterizing the channels in terms of angles of arrival. For a single RIS, this was done in [17], however, we investigate the feasibility of parametric channel estimation in the presence of multiple RISs. This way, we decrease the number of parameters to estimate, and we also get the opportunity to localize the user via

triangulation. We consider pure LOS channels and explore the feasibility of using positioning pilots for estimating the channels parametrically. Based on the azimuth AoA estimates, using the RIS geometry, for which we considered ULAs, we explore the possibility of estimating the UE-RIS channels by deriving the CRLB which is a lower bound on the MSE of any unbiased estimator. Furthermore, using the deployment geometry, we derive the Positioning Error Bound (PEB) using the CRLB on AoA estimation. Our numerical results show that for pure LOS channels, such a scheme is feasible as long as a proper algorithm to complete these tasks is designed. This chapter is based on the following article:

- **Doğa Gürgünoğlu**, Emil Björnson, Gábor Fodor, Joint Pilot-Based Localization and Channel Estimation in RIS-Aided Communication Systems, *IEEE Wireless Communications Letters*, 2024.

Chapter 6

In this chapter, we consider a multiuser multiple-input multiple-output (MU-MIMO) system where the users are located within the radiative near field of the base station with aperture antennas. We consider a two-dimensional multiple signal classification algorithm (2D-MUSIC) to estimate the range and azimuth angles of arrival for the users' channels, utilizing parametric radiative near-field channel models. We analyze the system performance by deriving the Cramér-Rao bound (CRB) for parametric estimation, and its effectiveness is compared against the least squares estimator, a non-parametric estimator. We derive closed-form expressions for the CRB, which has not been done for aperture arrays before. Our numerical results indicate that the 2D-MUSIC algorithm outperforms the least squares estimator. Furthermore, the results demonstrate that the performance of 2D-MUSIC achieves the parametric channel estimation CRB, which shows that the algorithm is asymptotically consistent and efficient.

- **Doğa Gürgünoğlu**, Alva Kosasih, Parisa Ramezani, Özlem Tuğfe Demir, Emil Björnson, Gábor Fodor, Performance Analysis of a 2D-MUSIC Algorithm for Parametric Near-Field Channel Estimation, *Submitted to IEEE Wireless Communications Letters*, 2024.

Chapter 2

Impact of Pilot Contamination Between Operators With Interfering Reconfigurable Intelligent Surfaces

Abstract

In this paper, we study the impact of pilot contamination in a system where two operators serve their respective users with the assistance of two wide-band reconfigurable intelligent surfaces (RIS), each belonging to a single operator. We consider one active user per operator and they use disjoint narrow frequency bands. Although each RIS is dedicated to a single operator, both users' transmissions are reflected by both RISs. We show that this creates a new kind of pilot contamination effect when pilots are transmitted simultaneously. Since combating inter-operator pilot contamination in RIS-assisted networks would require long pilot signal sequences to maintain orthogonality among the users of different operators, we propose the orthogonal configurations of the RISs. Numerical results show that this approach completely eliminates pilot contamination, and significantly improves the performance in terms of channel estimation and equalization by removing the channel estimation bias.

2.1 Introduction

Pilot contamination is a key problem that frequently arises in wireless communication systems [18]. When multiple users use the same pilot sequences simultaneously in the same band, due to the limited channel coherence time, the BS cannot distinguish their channels, which typically results in poor channel estimates and extra beamformed interference towards pilot-sharing UEs. Therefore,

pilot contamination adversely affects the coherent reception of data, and methods to mitigate pilot contamination have been widely studied in the communication literature [18–21].

In recent years, RISs have arisen as a new technology component for 6G [22]. An RIS is a surface consisting of multiple reflecting elements that have sub-wavelength spacing and controllable reflection properties [23]. This feature provides partial control of the propagation environment that can lead to better services for users, especially when their serving BS is not in their LOS. By adjusting the impedances of the individual elements via a RIS controller, the elements are capable of adding desired phase shifts to the reflected signals, thereby forming reflected beams in desired directions that can significantly boost the signal-to-interference-plus-noise ratio (SINR) at the receiver [22].

On the other hand, the addition of RISs to existing systems introduces new design and operational challenges. For example, the length of the pilot signal required by a single UE is proportional to the number of RIS elements (e.g., tens or hundreds), because the RIS must change its configuration to explore all channel dimensions [17, 24]. In addition, passive RIS causes multiplicative path losses, which increases the large-scale fading loss between the transmitter and the receiver [25]. Active RISs [10], on the other hand, are less energy efficient, and due to the presence of amplifiers, it introduces additional noise. While the aforementioned problems caused by the RIS have been recognized [26], pilot contamination caused by the presence of multiple RISs has not been studied in the literature. In this paper, however, we identify the creation of pilot contamination as another practical challenge: a UE that transmits pilots to its serving BS via multiple RIS, which change their configurations simultaneously, may cause a new kind of pilot contamination that has not been studied.

Wireless communication systems are governed by standards, and physical-layer specifications usually contain pre-defined sequences for pilot signals and codebooks for directional beamforming [27]. While the use RISs is not standardized yet, it is likely that the configuration sequences that facilitate the deployment of RISs while maintaining interoperability will be standardized. Consequently, when multiple cellular networks are deployed by different network operators in overlapping geographical areas, the RISs may adopt identical or overlapping pilot sequences and cause pilot contamination.

Due to the ability to change the environment's propagation characteristics, deploying multiple RISs in a geographical area also implies that pilot contamination can occur due to a UE's own pilot signal. Since this phenomenon may exacerbate the pilot contamination problem, it is clear that pilot contamination due to the presence of multiple RISs must be dealt with.

In this paper, we study the pilot contamination caused by the presence of multiple RISs by considering the uplink of a system consisting of two wide-band RISs, two single-antenna UEs, and two co-located single-antenna BSs, where the two UEs are subscribed to different operators with non-overlapping narrow-band channels at different frequencies. Each RIS is dedicated to a single operator,

but both UE signals are reflected from both RISs. In this scenario, although there is no interference between the two UEs, both RISs affect both frequency bands. We propose the use of orthogonal RIS configuration sequences during pilot transmission to avoid pilot contamination. First, we describe the channel estimation procedure with a lack of information on channel statistics, i.e., when the channels are characterized by deterministic parameters. Assuming identical and orthogonal RIS configurations, we derive the statistics of the ML estimates and the effect of pilot contamination on channel estimation. Then we analyze how it affects the data estimation process, and discuss how this effect can be mitigated.

2.2 System Model

We consider the uplink of a cellular system consisting of two wide-band RIS, two single-antenna UE, and two co-located single-antenna BSs, as shown in Fig. 2.1, where each RIS has N reflecting elements. The two UEs are subscribed to different operators—who use site-sharing to reduce deployment costs—and transmit over two disjoint narrow frequency bands to their respective serving BSs. Each RIS is dedicated to and controlled by a single operator but affects both bands. We consider an environment where the direct UE-BS paths are blocked, while the UE-RIS and RIS-BS paths are operational. Since the BSs and RISs have fixed deployment locations, we assume the RIS-BS channels $\mathbf{h}_k$ are known, while the UE-RIS channels $\mathbf{g}_k$ are unknown and to be estimated for $k = 1, 2$.

The signal transmitted by UE k reaches its serving BS through the channels $\mathbf{h}_k$ and $\mathbf{g}_k$, for $k = 1, 2$. Importantly, the UEs' transmitted signals are also reflected by the non-serving operator's RISs towards their serving BSs, which contaminates the pilot signal reflected by the serving RIS. This phenomenon is illustrated in Fig. 2.1, where the resulting UE-RIS and RIS-BS channels are denoted by $\mathbf{p}_k$ and $\mathbf{q}_k$, respectively, for $k = 1, 2$.

Since the BSs are unaware of the channels $\mathbf{q}_k$ and $\mathbf{p}_k$, they adopt misspecified system models for the received pilot and data signals. We also assume that the prior distributions of the channels are unavailable. Consequently, the BSs estimate the channels $\mathbf{g}_1$ and $\mathbf{g}_2$ via classical non-Bayesian parameter estimation methods during the channel estimation phase and use the channel estimates to perform data estimation [12, Section IV.C] during the data transmission phase. Defining the pilot signal of UE k as $s_k \in \mathbb{C}$, the received pilot signals on bands 1 and 2 at the BSs can be expressed as

$$y_{p1} = \sqrt{P_p}\mathbf{h}_1^T\mathbf{\Phi}_1\mathbf{g}_1 s_1 + \sqrt{P_p}\mathbf{q}_1^T\mathbf{\Phi}_2\mathbf{p}_1 s_1 + w_{p1}, \tag{2.1a}$$

$$y_{p2} = \sqrt{P_p}\mathbf{h}_2^T\mathbf{\Phi}_2\mathbf{g}_2 s_2 + \sqrt{P_p}\mathbf{q}_2^T\mathbf{\Phi}_1\mathbf{p}_2 s_2 + w_{p2}, \tag{2.1b}$$

where y_{pk} denotes the received pilot signal, $w_{pk} \sim \mathcal{CN}(0, 1)$ denotes the receiver noise for band k, and $\mathbf{\Phi}_k = \text{diag}(e^{-j\phi_{k1}}, \ldots, e^{-j\phi_{kN}})$ denotes the kth RIS's response matrix. We assume $s_1 = s_2 = 1$ without loss of generality. For channel

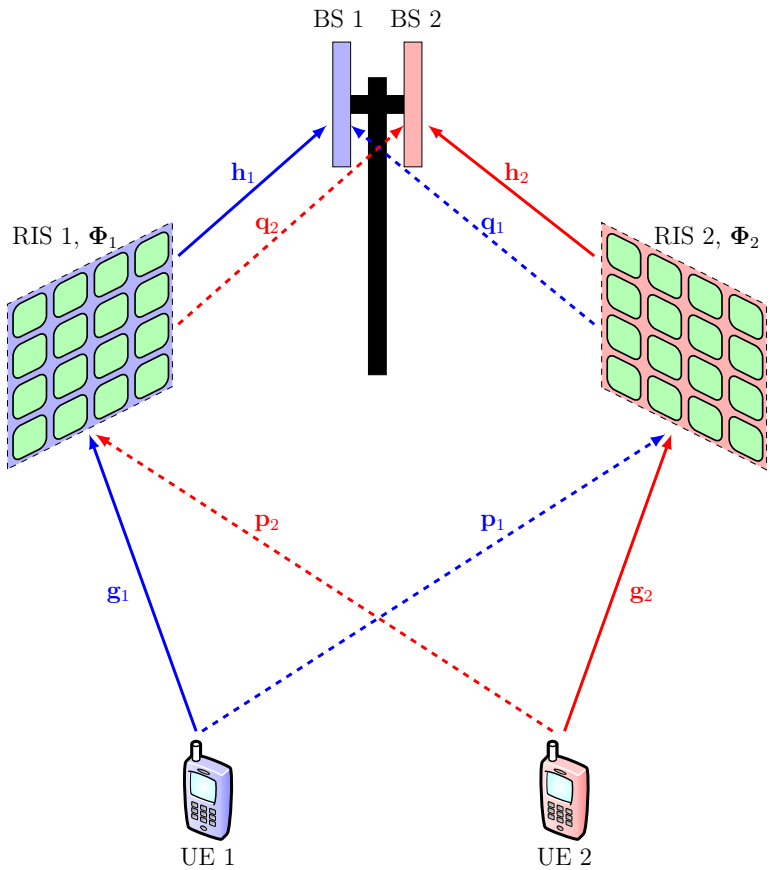

Figure 2.1: System setup with two UEs, two RISs and two co-located single-antenna BSs. The blue channels correspond to frequency band 1, and the red channels correspond to frequency band 2, subscribed by UEs 1 and 2, respectively. Desired channels are denoted by solid lines, while the undesired channels whose existence are unknown to the BSs are denoted by dashed lines. Each channel vector is N-dimensional in line with the number of elements in each RIS.

estimation, it is more convenient to rewrite (2.1) as

$$y_{p1} = \sqrt{P_p}\boldsymbol{\phi}_1^T \mathbf{D}_{\mathbf{h}_1}\mathbf{g}_1 + \sqrt{P_p}\boldsymbol{\phi}_2^T \mathbf{D}_{\mathbf{q}_1}\mathbf{p}_1 + w_{p1}, \tag{2.2a}$$

$$y_{p2} = \sqrt{P_p}\boldsymbol{\phi}_2^T \mathbf{D}_{\mathbf{h}_2}\mathbf{g}_2 + \sqrt{P_p}\boldsymbol{\phi}_1^T \mathbf{D}_{\mathbf{q}_2}\mathbf{p}_2 + w_{p2}, \tag{2.2b}$$

where $\mathbf{D}_{\mathbf{h}_k}$ and $\mathbf{D}_{\mathbf{q}_k}$ represent the diagonal matrices containing the elements of $\mathbf{h}_k$ and $\mathbf{q}_k$, and $\boldsymbol{\phi}_k$ denotes the column vectors containing the diagonal entries of $\boldsymbol{\Phi}_k$ for $k = 1, 2$.

As there are N parameters in $\mathbf{g}_1$ and $\mathbf{g}_2$, at least N linearly independent observations are needed to estimate them. To this end, we perform $L \geq N$ pilot transmissions over time, and we vertically stack the received pilot signals to obtain

$$\mathbf{y}_{p1} = \sqrt{P_p}\mathbf{B}_1\mathbf{D}_{\mathbf{h}_1}\mathbf{g}_1 + \sqrt{P_p}\mathbf{B}_2\mathbf{D}_{\mathbf{q}_1}\mathbf{p}_1 + \mathbf{w}_{p1}, \tag{2.3a}$$

$$\mathbf{y}_{p2} = \sqrt{P_p}\mathbf{B}_2\mathbf{D}_{\mathbf{h}_2}\mathbf{g}_2 + \sqrt{P_p}\mathbf{B}_1\mathbf{D}_{\mathbf{q}_2}\mathbf{p}_2 + \mathbf{w}_{p2}, \tag{2.3b}$$

where $\mathbf{y}_{pk} = [y_{pk}[1], \ldots, y_{pk}[L]]^T$ denotes the sequence of received uplink pilots from the kth UE over L time instances, and the matrices $\mathbf{B}_1$ and $\mathbf{B}_2$ represent the sequence of RIS configurations over L time instances, that is, $\mathbf{B}_k \triangleq \begin{bmatrix}\boldsymbol{\phi}_k[1] & \ldots & \boldsymbol{\phi}_k[L]\end{bmatrix}^T$ for $k = 1, 2$. Recall that BS 1 is not aware of the reflection of UE 1's signal from RIS 2 and vice versa. Consequently, the BSs assumes the following misspecified received pilot signal models:

$$\hat{\mathbf{y}}_{p1} = \sqrt{P_p}\mathbf{B}_1\mathbf{D}_{\mathbf{h}_1}\mathbf{g}_1 + \mathbf{w}_{p1}, \tag{2.4a}$$

$$\hat{\mathbf{y}}_{p2} = \sqrt{P_p}\mathbf{B}_2\mathbf{D}_{\mathbf{h}_2}\mathbf{g}_2 + \mathbf{w}_{p2}. \tag{2.4b}$$

Based on (2.4), the estimation of $\mathbf{g}_1$ and $\mathbf{g}_2$ is described and analyzed in the next section.

2.3 Maximum Likelihood Channel Estimation

To estimate $\mathbf{g}_k$, which is N-dimensional, BS k requires at least N independent observations for $k = 1, 2$. Hence, both $\mathbf{B}_1, \mathbf{B}_2 \in \mathbb{C}^{L\times N}$ must have full column rank. Furthermore, we require that the RIS configurations on different time instances be orthogonal and contain entries on the unit circle that can be realized using a reflecting element. These assumptions result in $\mathbf{B}_k^H\mathbf{B}_k = L\mathbf{I}_N$. In classical non-Bayesian parameter estimation, the ML estimator is widely used, which maximizes the likelihood function of the received observation over the unknown parameter. Since the BSs have misspecified received pilot signal models, they will instead maximize the likelihood functions obtained from the misspecified model, leading to misspecified maximum likelihood (MML) estimators. For (2.4), the

MML estimator can be expressed as

$$\begin{aligned}\hat{\mathbf{g}}_k &= \arg\max_{\mathbf{g}_k} f(\mathbf{y}_{pk};\mathbf{g}_k)\\ &= \arg\max_{\mathbf{g}_k} \frac{1}{(\pi\sigma_w^2)^L}\exp\left(-\frac{\|\mathbf{y}_{pk}-\sqrt{P_p}\mathbf{B}_k\mathbf{D}_{\mathbf{h}_k}\mathbf{g}_k\|^2}{\sigma_w^2}\right)\\ &= \arg\min_{\mathbf{g}_k}\left\|\mathbf{y}_{pk}-\sqrt{P_p}\mathbf{B}_k\mathbf{D}_{\mathbf{h}_k}\mathbf{g}_k\right\|^2\\ &= \frac{1}{\sqrt{P_p}}\mathbf{D}_{\mathbf{h}_k}^{-1}(\mathbf{B}_k^H\mathbf{B}_k)^{-1}\mathbf{B}_k^H\mathbf{y}_{pk}\\ &= \frac{1}{L\sqrt{P_p}}\mathbf{D}_{\mathbf{h}_k}^{-1}\mathbf{B}_k^H\mathbf{y}_{pk}. \end{aligned} \tag{2.5}$$

In the following subsections, we describe the behavior of this estimator for two different choices of the $\mathbf{B}_k$ matrices.

Case 1: The RISs Adopt the Same Configuration Sequence

We discussed earlier that in the absence of inter-operator cooperation, it is highly likely that the RISs will use the same sequence of configurations during the channel estimation phase, which corresponds to $\mathbf{B}_1 = \mathbf{B}_2 = \mathbf{B}$.[1] In this case, (2.5) becomes

$$\hat{\mathbf{g}}_k = \mathbf{g}_k + \mathbf{D}_{\mathbf{h}_k}^{-1}\mathbf{D}_{\mathbf{q}_k}\mathbf{p}_k + \frac{1}{L\sqrt{P_p}}\mathbf{D}_{\mathbf{h}_k}^{-1}\mathbf{B}^H\mathbf{w}_{pk}. \tag{2.6}$$

Since we consider the channels as deterministic parameters, we obtain the probability distribution

$$\hat{\mathbf{g}}_k \sim \mathcal{CN}\left(\mathbf{g}_k + \mathbf{D}_{\mathbf{h}_k}^{-1}\mathbf{D}_{\mathbf{q}_k}\mathbf{p}_k, \frac{\sigma_w^2}{LP_p}(\mathbf{D}_{\mathbf{h}_k}^H\mathbf{D}_{\mathbf{h}_k})^{-1}\right) \tag{2.7}$$

We notice that $\hat{\mathbf{g}}_k$ is biased; that is, $\mathbf{b}_k \triangleq \mathbb{E}[\hat{\mathbf{g}}_k - \mathbf{g}_k] = \mathbf{D}_{\mathbf{h}_k}^{-1}\mathbf{D}_{\mathbf{q}_k}\mathbf{p}_k \neq \mathbf{0}$. The estimator bias does not vanish when increasing P_p or L, and decreasing σ_w^2, hence, it is not asymptotically unbiased. This is a new instance of an extensively studied phenomenon in the massive MIMO literature: pilot contamination [18,19]. Interestingly, the RISs cause pilot contamination even between two non-overlapping frequency bands, which has not been widely recognized in the literature so far.

[1] The analysis in this paper can be easily extended to the case when $\mathbf{B}_1 = \mathbf{U}\mathbf{B}_2$ for some unitary matrix $\mathbf{U}$, so that configuration sequences have identical spans. It is the overlap of the spans that can cause issues.

Case 2: The RISs Adopt Different Configuration Sequences

In this subsection, we consider the generic case of $\mathbf{B}_1 \neq \mathbf{B}_2$. To motivate the proposed method for configuring $\mathbf{B}_1$ and $\mathbf{B}_2$, we first consider the case where the BSs are aware of the true signal model in (2.3), and therefore can estimate both $\mathbf{g}_k$ and $\mathbf{r}_k \triangleq \mathbf{D}_{\mathbf{q}_k}\mathbf{p}_\mathbf{k}$. The resulting system model can be expressed as

$$\mathbf{y}_{p1} = \sqrt{P}_p \begin{bmatrix}\mathbf{B}_1\mathbf{D}_{\mathbf{h}_1} & \mathbf{B}_2\end{bmatrix} \begin{bmatrix}\mathbf{g}_1 \\ \mathbf{r}_1\end{bmatrix} + \mathbf{w}_{p1}, \tag{2.8a}$$

$$\mathbf{y}_{p2} = \sqrt{P}_p \begin{bmatrix}\mathbf{B}_2\mathbf{D}_{\mathbf{h}_2} & \mathbf{B}_1\end{bmatrix} \begin{bmatrix}\mathbf{g}_2 \\ \mathbf{r}_2\end{bmatrix} + \mathbf{w}_{p2}. \tag{2.8b}$$

In (2.8), a known linear transformation is applied to the parameter vector of interest in the presence of additive noise. Consequently, the ML estimates for UE 1's unknown channels become

$$\begin{bmatrix}\hat{\mathbf{g}}_1 \\ \hat{\mathbf{r}}_1\end{bmatrix} = \frac{1}{\sqrt{P_p}} \begin{bmatrix}L\mathbf{D}_{\mathbf{h}_1}^H\mathbf{D}_{\mathbf{h}_1} & \mathbf{D}_{\mathbf{h}_1}^H\mathbf{B}_1^H\mathbf{B}_2 \\ \mathbf{B}_2^H\mathbf{B}_1\mathbf{D}_{\mathbf{h}_1} & L\mathbf{I}_N\end{bmatrix}^{-1} \begin{bmatrix}\mathbf{D}_{\mathbf{h}_1}^H\mathbf{B}_1^H \\ \mathbf{B}_2^H\end{bmatrix} \mathbf{y}_{p1}. \tag{2.9}$$

Note that in this case, the total dimension of the unknown parameter vector is $2N$, hence, at least $2N$ independent observations are required for the matrix inverse to exist. The structure in (2.9) applies to UE 2 with alternated indices, and it gives the ML estimator, which is both unbiased and efficient, since (2.8) is a linear observation model with additive Gaussian noise [28, Theorem 7.3]. Hence, (2.9) is unbiased irrespective of other parameters such as σ_w^2, L, P_p, and it achieves the CRLB, which provides a lower bound on the MSE of any unbiased estimator [12]. It has to be noted that when $\mathbf{B}_1^H\mathbf{B}_2 = \mathbf{0}$, (2.9) becomes

$$\begin{aligned}\begin{bmatrix}\hat{\mathbf{g}}_1 \\ \hat{\mathbf{r}}_1\end{bmatrix} &= \frac{1}{L\sqrt{P_p}} \begin{bmatrix}\mathbf{D}_{\mathbf{h}_1}^H\mathbf{D}_{\mathbf{h}_1} & \mathbf{0} \\ \mathbf{0} & \mathbf{I}_N\end{bmatrix}^{-1} \begin{bmatrix}\mathbf{D}_{\mathbf{h}_1}^H\mathbf{B}_1^H \\ \mathbf{B}_2^H\end{bmatrix} \mathbf{y}_{p1} \\ &= \frac{1}{L\sqrt{P_p}} \begin{bmatrix}\mathbf{D}_{\mathbf{h}_1}^{-1}\mathbf{B}_1^H \\ \mathbf{B}_2^H\end{bmatrix} \mathbf{y}_{p1}.\end{aligned} \tag{2.10}$$

Note that the expression for $\hat{\mathbf{g}}_1$ in (2.10) is the same as in (2.5). This shows that when $\mathbf{B}_1^H\mathbf{B}_2 = \mathbf{0}$, the MML in (2.5) coincides with the ML estimator; that is, the misspecified model is sufficient when the configuration sequences are designed to alleviate pilot interference. The probability distribution of $\hat{\mathbf{g}}_k$ in this case can be expressed as

$$\hat{\mathbf{g}}_k \sim \mathcal{CN}\left(\mathbf{g}_k, \frac{\sigma_w^2}{LP_p}(\mathbf{D}_{\mathbf{h}_k}^H\mathbf{D}_{\mathbf{h}_k})^{-1}\right), \tag{2.11}$$

which shows that choosing the RIS configuration sequences such that $\mathbf{B}_1$ and $\mathbf{B}_2$ removes the bias from the MML estimator. However, the major setback of this approach is that the minimum number of observations required for this

channel estimation procedure is $2N$ instead of N, due to the fact that the $2N$-many L-dimensional columns must all be orthogonal to each other, for which $L \geq 2N$ is required. Considering that the estimator bias in (2.7) does not vanish with increasing L, this is a necessary sacrifice. Hence, it has to be noted that the number of pilot transmissions increases linearly with the number of RISs deployed in proximity. In the next section, data signal transmission and its estimation will be analyzed.

MSE During Channel Estimation

We consider the MSE as the channel estimation performance metric, which is the trace of the error covariance matrix that is derived in this section. In this derivation, we do not assume a particular choice of $\mathbf{B}_1, \mathbf{B}_2$, but we utilize the basic assumption $\mathbf{B}_k \mathbf{B}_k^H = L\mathbf{I}_N$. Consequently, we use $\mathbf{b}_k$ to denote the potential estimator bias. We can then compute the error covariance matrix as

$$\begin{aligned}
\boldsymbol{\Sigma}_{e,k} &= \mathbb{E}\left[(\hat{\mathbf{g}}_k - \mathbf{g}_k)(\hat{\mathbf{g}}_k - \mathbf{g}_k)^H\right] \\
&= \mathbf{b}_k \mathbf{b}_k^H + \frac{1}{LP_p} \mathbb{E}\left[\mathbf{D}_{\mathbf{h}_k}^{-1} \mathbf{w}_{pk} \mathbf{w}_{pk}^H \mathbf{D}_{\mathbf{h}_k}^{-H}\right] \\
&= \mathbf{b}_k \mathbf{b}_k^H + \frac{\sigma_w^2}{LP_p} \left(\mathbf{D}_{\mathbf{h}_k} \mathbf{D}_{\mathbf{h}_k}^H\right)^{-1}. \qquad (2.12)
\end{aligned}$$

Consequently, the trace of the error covariance matrix becomes

$$\operatorname{tr}(\boldsymbol{\Sigma}_{e,k}) = \|\mathbf{b}_k\|^2 + \frac{\sigma_w^2}{LP_p} \sum_{n=1}^{N} \frac{1}{|h_{kn}|^2} \qquad (2.13)$$

Note that for high P_p, L, and low σ_w^2, the second term in (2.13) vanishes, and the trace of the error covariance converges to $\|\mathbf{b}_k\|^2$ which depend on the configuration of $\mathbf{B}_1, \mathbf{B}_2$:

$$\|\mathbf{b}_k\|^2 = \begin{cases} \sum_{n=1}^{N} \frac{|r_{kn}|^2}{|h_{kn}|^2} & \mathbf{B}_1 = \mathbf{B}_2, \\ 0 & \mathbf{B}_1^H \mathbf{B}_2 = \mathbf{0}. \end{cases} \qquad (2.14)$$

This result shows that configuring the RISs such that $\mathbf{B}_1^H \mathbf{B}_2 = \mathbf{0}$ removes the asymptotic floor on the average MSE, which comes from the energy of the estimator bias. On the other hand, when the intended RIS-BS links $\mathbf{h}_1, \mathbf{h}_2$ are strong relative to the unintended and unknown overall link $\mathbf{r}_k$, the estimator bias will be weaker and the cost of choosing $\mathbf{B}_1 = \mathbf{B}_2$ will be lower. Nevertheless, pilot contamination results in a fundamental error floor, even if the RISs are utilized in different bands. In the next section, we consider the estimation of data based on the channel estimation performed in this section and analyze the consequence of pilot contamination in this phase.

2.4 Data Transmission

The channel estimation is followed by data transmission. We consider a data packet with a duration shorter than the channel coherence time, therefore, the channels acting on the transmitted data signals are the same as in the channel estimation part. Defining the data signal transmitted by the kth UE as $x_k \sim \mathcal{CN}(0,1)$, we can express the received data as

$$y_1 = \sqrt{P_d}(\mathbf{h}_1^T \hat{\mathbf{\Phi}}_1 \mathbf{g}_1 + \mathbf{q}_1^T \hat{\mathbf{\Phi}}_2 \mathbf{p}_1)x_1 + w_1, \tag{2.15a}$$

$$y_2 = \sqrt{P_d}(\mathbf{h}_2^T \hat{\mathbf{\Phi}}_2 \mathbf{g}_2 + \mathbf{q}_2^T \hat{\mathbf{\Phi}}_1 \mathbf{p}_2)x_2 + w_2, \tag{2.15b}$$

where $w_k \sim \mathcal{CN}(0, \sigma_w^2)$ denotes the receiver noise, P_d denotes the data transmission power, and the RIS configuration matrices $\hat{\mathbf{\Phi}}_k$ are selected based on the estimated channels to maximize the average channel gain as shown in [17, Sec. II]:

$$\begin{aligned} \hat{\phi}_{kn} &= \arg(h_{kn}) + \arg(\hat{g}_{kn}), \\ \hat{\mathbf{\Phi}}_k &= \operatorname{diag}\left(e^{-j\hat{\phi}_{k1}}, \ldots, e^{-j\hat{\phi}_{kN}}\right). \end{aligned} \tag{2.16}$$

However, since the BSs are unaware of the unintended reflections and base their data estimation on channel estimates, they assume the following misspecified received data signal models:

$$\hat{y}_1 = \sqrt{P_d}\mathbf{h}_1^T \hat{\mathbf{\Phi}}_1 \hat{\mathbf{g}}_1 x_1 + w_1, \tag{2.17a}$$

$$\hat{y}_2 = \sqrt{P_d}\mathbf{h}_2^T \hat{\mathbf{\Phi}}_2 \hat{\mathbf{g}}_2 x_2 + w_2. \tag{2.17b}$$

Introducing the notation $m_k \triangleq \sqrt{P_d}(\mathbf{h}_k^T \hat{\mathbf{\Phi}}_k \mathbf{g}_k + \mathbf{q}_k^T \hat{\mathbf{\Phi}}_j \mathbf{p}_k)$ for $j,k \in \{1,2\}, j \neq k$, and $\hat{m}_k \triangleq \sqrt{P_d}\mathbf{h}_k^T \hat{\mathbf{\Phi}}_k \hat{\mathbf{g}}_k$, (2.15) and (2.17) can be expressed as

$$y_k = m_k x_k + w_k, \quad k = 1,2, \tag{2.18a}$$

$$\hat{y}_k = \hat{m}_k x_k + w_k, \quad k = 1,2. \tag{2.18b}$$

Based on the misspecified observation model in (2.18b), the BSs estimate x_k by using the misspecified MMSE estimator

$$\hat{x}_k = \frac{\hat{m}_k^*}{|\hat{m}_k|^2 + \sigma_w^2} y_k, \quad k = 1,2. \tag{2.19}$$

In this section, we consider the MSE between x_k and $\hat{x}_k$ as the performance metric for the data transmission. We derive the data estimation MSE for UE k

as

$$\begin{aligned}
&\mathbb{E}\left[|x_k-\hat{x}_k|^2\right]=1+\mathbb{E}\left[|\hat{x}_k|^2\right]-2\mathrm{Re}(\mathbb{E}[x_k\hat{x}_k^*])\\
&=1+\mathbb{E}\left[\frac{|\hat{m}_k|^2(|m_k|^2+\sigma_w^2)}{(|\hat{m}_k|^2+\sigma_w^2)^2}\right]\\
&-2\mathrm{Re}\left(\mathbb{E}\left[\frac{\hat{m}_k m_k^*}{|\hat{m}_k|^2+\sigma_w^2}\right]\right)\\
&=1+\mathbb{E}\left[\frac{|\hat{m}_k|^2(|m_k|^2+\sigma_w^2)-2\mathrm{Re}(\hat{m}_1 m_1^*)(|\hat{m}_k|^2+\sigma_w^2)}{(|\hat{m}_k|^2+\sigma_w^2)^2}\right]\\
&=1+\mathbb{E}\left[\frac{|\hat{m}_k|^2(|m_k|^2+\sigma_w^2)-2\mathrm{Re}(\hat{m}_1 m_1^*)(|\hat{m}_k|^2+\sigma_w^2)}{(|\hat{m}_k|^2+\sigma_w^2)^2}\right]\\
&+\mathbb{E}\left[\frac{\sigma_w^2(|m_k|^2+\sigma_w^2)-\sigma_w^2(|m_k|^2+\sigma_w^2)}{(|\hat{m}_k|^2+\sigma_w^2)^2}\right]\\
&=1+\mathbb{E}\left[\frac{(|\hat{m}_k|^2+\sigma_w^2)(|m_k|^2+\sigma_w^2-2\mathrm{Re}(\hat{m}_k m_k^*))}{(\hat{m}_k^2+\sigma_w^2)^2}\right]\\
&-\mathbb{E}\left[\frac{\sigma_w^2(|m_k|^2+\sigma_w^2)}{(\hat{m}_k^2+\sigma_w^2)^2}\right]\\
&=\mathbb{E}\left[\frac{|m_k-\hat{m}_k|^2+2\sigma_w^2}{|\hat{m}_k|^2+\sigma_w^2}\right]-\mathbb{E}\left[\frac{\sigma_w^2(|m_k|^2+\sigma_w^2)}{(|\hat{m}_k|^2+\sigma_w^2)^2}\right].
\end{aligned}\tag{2.20}$$

Defining $\epsilon_k \triangleq m_k-\hat{m}_k$, (2.20) can be rewritten as

$$\mathbb{E}[|x_k-\hat{x}_k|^2]=\mathbb{E}\left[\frac{|\epsilon_k|^2+2\sigma_w^2}{|m_k-\epsilon_k|^2+\sigma_w^2}-\frac{\sigma_w^2(|m_k|^2+\sigma_w^2)}{(|m_k-\epsilon_k|^2+\sigma_w^2)^2}\right]\tag{2.21}$$

To examine the impact of pilot contamination on the data estimation performance more clearly, we now consider channel estimation at high SNRs, so that the estimation error only comes from the estimator bias, i.e., pilot contamination. This happens when L or P_p is high and/or σ_w^2 is low, which results in that the estimator covariances in (2.7) and (2.11) become zero. For notational convenience, we consider the case where P_p is arbitrarily large so that $\lim_{P_p\to\infty}\hat{\mathbf{g}}_k=\mathbf{g}_k+\mathbf{b}_k$, where

$$\mathbf{b}_k=\begin{cases}\mathbf{D}_{\mathbf{h}_k}^{-1}\mathbf{D}_{\mathbf{q}_k}\mathbf{p}_k & \mathbf{B}_1=\mathbf{B}_2,\\ \mathbf{0} & \mathbf{B}_1^H\mathbf{B}_2=\mathbf{0}.\end{cases}\tag{2.22}$$

Data MSE with Channel Estimation at High SNR

In (2.21), ϵ_k and m_k are functions of $\hat{\mathbf{g}}_1$ and $\hat{\mathbf{g}}_2$, therefore as $\hat{\mathbf{g}}_1$ and $\hat{\mathbf{g}}_2$ converge to their means, ϵ_k and m_k become

$$\overline{m}_k=\sqrt{P_d}(\mathbf{h}_k^T\bar{\mathbf{\Phi}}_k\mathbf{g}_k+\mathbf{q}_k^T\bar{\mathbf{\Phi}}_j\mathbf{p}_k),\tag{2.23a}$$

$$\bar{\epsilon}_k=\sqrt{P_d}(\mathbf{q}_k^T\bar{\mathbf{\Phi}}_j\mathbf{p}_k-\mathbf{h}_k^T\bar{\mathbf{\Phi}}_k\mathbf{b}_k),\tag{2.23b}$$

for $j, k \in \{1, 2\}$ and $j \neq k$. $\bar{\boldsymbol{\Phi}}_k$ denotes the RIS configuration computed according to (2.16) with $\hat{\mathbf{g}}_k = \mathbf{g}_k + \mathbf{b}_k$. At high SNR, the MSE in (2.21) can be rewritten as

$$\text{MSE} = \frac{|\overline{\epsilon}_k|^2 + 2\sigma_w^2}{|\overline{m}_k - \overline{\epsilon}_k|^2 + \sigma_w^2} - \frac{\sigma_w^2(|\overline{m}_k|^2 + \sigma_w^2)}{(|\overline{m}_k - \overline{\epsilon}_k|^2 + \sigma_w^2)^2}. \tag{2.24}$$

This is a practically achievable limit since RIS-aided systems require large pilot sequences over a narrow bandwidth, so the SNR might be larger than in the data transmission phase.

Data MSE with Transmission at High SNR

In the previous subsection, we obtained the expression for data MSE when the channels are estimated at a high pilot SNR, while the data transmission is done at an arbitrary SNR. To study the case when also the data transmission a step further, we let $\sigma_w^2 \to 0$, which results in the limit

$$\lim_{\sigma_w^2 \to 0} \text{MSE} = \frac{|\overline{\epsilon}_k|^2}{|\overline{m}_k - \overline{\epsilon}_k|^2}. \tag{2.25}$$

Note that the resulting expression denotes the ratio between the estimated overall SISO channel $\hat{m}_k$'s power and the mismatch parameter ϵ_k's power. Recall that $\mathbf{b}_k$ depends on which RIS pilot sequence is utilized. For $\mathbf{B}_1 = \mathbf{B}_2$, we can obtain ϵ_k as

$$\begin{aligned}
\epsilon_k &= \sqrt{P_d}\mathbf{q}_k^T \hat{\boldsymbol{\Phi}}_j \mathbf{p}_k - \sqrt{P_d}\mathbf{h}_k^T \hat{\boldsymbol{\Phi}}_k \mathbf{D}_{\mathbf{h}_1}^{-1} \mathbf{D}_{\mathbf{q}_1} \mathbf{p}_1 \\
&= \sqrt{P_d}\mathbf{q}_k^T \hat{\boldsymbol{\Phi}}_j \mathbf{p}_k - \sqrt{P_d}\hat{\boldsymbol{\phi}}_k \mathbf{D}_{\mathbf{h}_k} \mathbf{D}_{\mathbf{h}_k}^{-1} \mathbf{D}_{\mathbf{q}_1} \mathbf{p}_1 \\
&= \sqrt{P_d}\mathbf{q}_k^T \hat{\boldsymbol{\Phi}}_j \mathbf{p}_k - \sqrt{P_d}\hat{\boldsymbol{\phi}}_k \mathbf{D}_{\mathbf{q}_1} \mathbf{p}_1 \\
&= \sqrt{P_d}\mathbf{q}_k^T \hat{\boldsymbol{\Phi}}_j \mathbf{p}_k - \sqrt{P_d}\mathbf{q}_k^T \hat{\boldsymbol{\Phi}}_k \mathbf{p}_k \\
&= \sqrt{P_d}\mathbf{q}_k^T (\hat{\boldsymbol{\Phi}}_j - \hat{\boldsymbol{\Phi}}_k) \mathbf{p}_k.
\end{aligned} \tag{2.26}$$

On the other hand, $\mathbf{B}_1^H \mathbf{B}_2 = 0$ removes $\mathbf{b}_k$ for $k \in \{1, 2\}$. Consequently, we have

$$\epsilon_k = \begin{cases} \sqrt{P_d}\mathbf{q}_k^T (\hat{\boldsymbol{\Phi}}_j - \hat{\boldsymbol{\Phi}}_k) \mathbf{p}_k & \mathbf{B}_1 = \mathbf{B}_2, \\ \sqrt{P_d}\mathbf{q}_k^T \hat{\boldsymbol{\Phi}}_j \mathbf{p}_k & \mathbf{B}_1^H \mathbf{B}_2 = \mathbf{0}. \end{cases} \tag{2.27}$$

It is possible to observe that the ϵ_k corresponds to only the unintended reflection path itself when $\mathbf{B}_1^H \mathbf{B}_2 = \mathbf{0}$. On the other hand, $\mathbf{B}_1 = \mathbf{B}_2$ yields an expression depending on the difference between the two RISs' configurations during data transmission. Since each RIS is configured based on the channels of their respective users, it is highly unlikely that the configurations will be close. Moreover, it has to be noted that the RIS configuration of the non-serving RIS is different among the two cases since the channel estimates are also different.

Table 2.1: Parameters used in the numerical results.

Parameter	Value
P_p or P_d	$-30, -25, \ldots, 40$ dBm[2]
UE-RIS path loss	-80 dB
RIS-BS path loss	-60 dB
σ_w^2	-90 dBm
N	256
L	513

2.5 Numerical Results

In this section, numerical results are provided to demonstrate the impact of pilot contamination in both the channel and data estimation phases. We consider $N = 256$ RIS elements. First, we demonstrate the results for the trace of the channel estimation error covariance matrix (i.e., the sum MSE). Then, for a single set of channel realizations, we provide the data estimation MSE for different data transmission powers. We also provide a Cumulative Distribution Function (CDF) plot for the high-SNR data estimation MSE floors under $\mathbf{B}_1 = \mathbf{B}_2$ and $\mathbf{B}_1^H \mathbf{B}_2 = \mathbf{0}$. The list of parameters used can be found in Table 2.1.

Channel Estimation

For the channel estimation, we consider the MSE as our performance metric. Moreover, we consider the results for a single UE, since the results for different UEs only differ by the channel realizations. In Fig. 2.2, we plot (2.13) for different values of P_p, and we also provide the high-SNR floor for the case where $\mathbf{B}_1 = \mathbf{B}_2$. Note that at lower transmission powers, the covariance matrix of the estimator acts dominantly, hence, both RIS configurations perform nearly the same. However, after $P_p = 20$ dBm, the power of the estimator bias starts to dominate, and the average MSE for $\mathbf{B}_1 = \mathbf{B}_2$ goes to the floor denoted by the black dashed line, which is given by (2.14). On the other hand, the average MSE for $\mathbf{B}_1^H \mathbf{B}_2 = \mathbf{0}$ does not stop there but keeps decreasing towards zero. As mentioned before, the MML estimators used by the BSs coincide with the true ML estimators when the RISs are configured such that $\mathbf{B}_1^H \mathbf{B}_2 = \mathbf{0}$.

Data Estimation

In Fig. 2.3, the data estimation MSE performance with the two RIS pilot configurations are analyzed when the channel estimation SNR is high. That is, (2.24) is plotted for $\mathbf{B}_1 = \mathbf{B}_2$ and $\mathbf{B}_1^H \mathbf{B}_2 = \mathbf{0}$. In addition, the case where all of the

[2]The results for $P_p = 45, 50, 55,$ and 60 dBm are also demonstrated in Fig. 2.2 to display the high SNR floor more clearly.

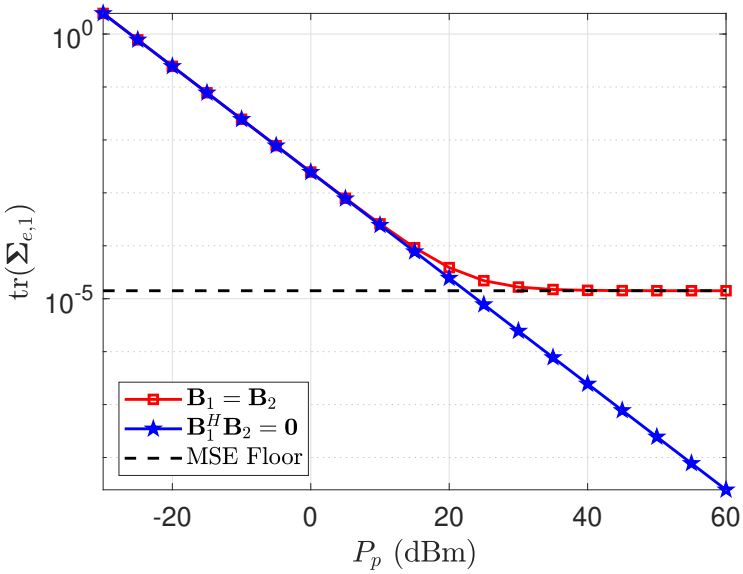

Figure 2.2: Pilot transmission power versus channel estimation MSE.

channels are perfectly known is plotted to serve as the golden standard, labeled as *Perfect CSI*. However, even when all the channels are perfectly known, each RIS is assumed to be optimized according to the subscribed UE's CSI. Note that although the channel estimation SNR is high, $\mathbf{B}_1 = \mathbf{B}_2$ yields biased estimates of $\mathbf{g}_1$ due to pilot contamination caused by self-interference. On the other hand, $\mathbf{B}_1^H\mathbf{B}_2 = \mathbf{0}$ yields the true $\mathbf{g}_1$ as the estimate, however, since BS 1 is unaware of the path through the second RIS, the data estimate is biased, hence, there is still a high data transmission SNR floor. At around $P_d = 5$ dBm, $\mathbf{B}_1 = \mathbf{B}_2$ starts to approach the high-SNR floor. On the other hand, $\mathbf{B}_1^H\mathbf{B}_2 = \mathbf{0}$ does not suffer from the lack of awareness of the second RIS path until around $P_d = 20$ dBm. Hence, Fig. 2.3 clearly shows the benefit of configuring the RIS pilot configurations sequences orthogonally.

Note that (2.25) and (2.27) do not guarantee the superiority of $\mathbf{B}_1^H\mathbf{B}_2 = \mathbf{0}$ over $\mathbf{B}_1 = \mathbf{B}_2$, since if both RISs were configured identically during the data transmission phase, $\mathbf{B}_1 = \mathbf{B}_2$ would not suffer from a high-SNR data estimation MSE floor. To demonstrate that this scenario is highly unlikely, empirical CDFs of the MSE floors at high SNR are provided. We generate each channel according to $\mathcal{CN}(\mathbf{0}, \mathbf{I}_N)$, and then scale them according to the path losses given in Table 2.1. The resulting CDFs are provided in Fig. 2.4. This figure is generated by using 10^6 different sets of channel realizations for $N = 32$ RIS elements. With a probability less then 10^{-6}, the high-SNR floor under $\mathbf{B}_1^H\mathbf{B}_2 = \mathbf{0}$ is much lower than that of $\mathbf{B}_1 = \mathbf{B}_2$, clearly demonstrating the benefit of using orthogonal RIS

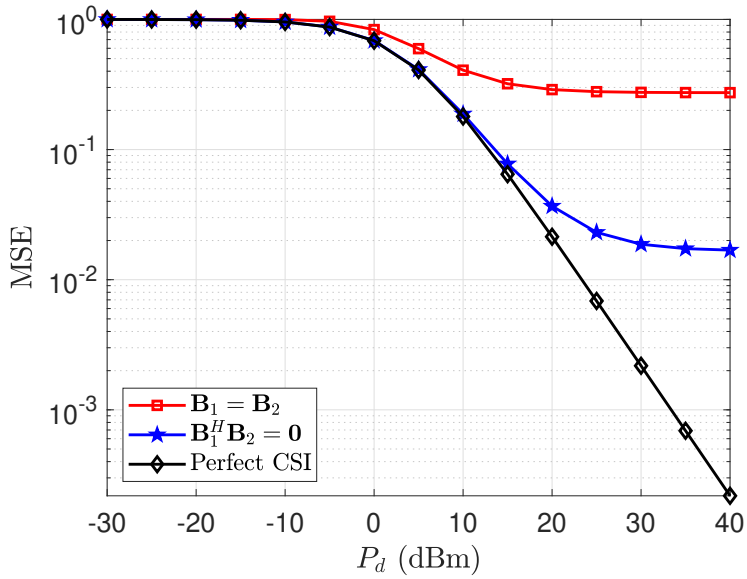

Figure 2.3: Data transmission power versus data estimation MSE with high channel estimation SNR.

pilot configurations over identical configurations.

2.6 Conclusions

In this paper, we have studied the impact of pilot contamination in a system consisting of two wide-band RISs, two single-antenna UEs, and two co-located single-antenna BSs. We have demonstrated that the presence of multiple RISs in the same area causes pilot contamination, although the UEs are subscribed to different operators and transmit over disjoint narrow frequency bands. To combat this new type of pilot contamination, we proposed the use of orthogonal RIS configurations during pilot transmission. In the numerical results, we have clearly shown that the proposed approach eliminates pilot contamination completely, and decreases data estimation MSE significantly. While increasing the number of pilots to configure RISs orthogonally alleviates pilot contamination, more efficient ways of dealing with this problem are needed in the future.

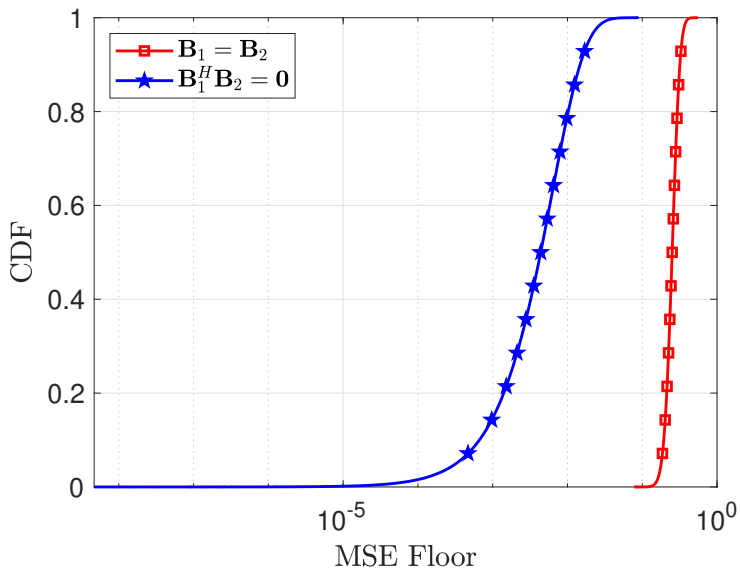

Figure 2.4: CDF of the data-MSE floors for two RIS pilot configurations for i.i.d. Rayleigh fading.

Chapter 3

Combating Inter-Operator Pilot Contamination in Reconfigurable Intelligent Surfaces Assisted Multi-Operator Networks

Abstract

In this paper, we study a new kind of pilot contamination appearing in multi-operator reconfigurable intelligent surfaces (RIS) assisted networks, where multiple operators provide services to their respective served users. The operators use dedicated frequency bands, but each RIS inadvertently reflects the transmitted uplink signals of the user equipment devices in multiple bands. Consequently, the concurrent reflection of pilot signals during the channel estimation phase introduces a new inter-operator pilot contamination effect. We investigate the implications of this effect in systems with either deterministic or correlated Rayleigh fading channels, specifically focusing on its impact on channel estimation quality, signal equalization, and channel capacity. The numerical results demonstrate the substantial degradation in system performance caused by this phenomenon and highlight the pressing need to address inter-operator pilot contamination in multi-operator RIS deployments. To combat the negative effect of this new type of pilot contamination, we propose to use orthogonal RIS configurations during uplink pilot transmission, which can mitigate or eliminate the negative effect of inter-operator pilot contamination at the expense of some inter-operator information exchange and orchestration.

3.1 Introduction

Pilot contamination is a key problem that frequently arises in wireless communication systems [18]. When multiple users use the same pilot sequences simul-

taneously in the same band, due to the limited channel coherence time, the BS cannot distinguish their channels. This typically results in poor channel estimates and extra beamformed interference from or towards the UEs that reuse the same pilot sequence. Therefore, pilot contamination adversely affects the coherent reception of data, and methods to mitigate pilot contamination—including adaptive pilot reuse, power control, user grouping, multi-cell coordination, and coded random access techniques—have been widely studied in the communication literature [18–21, 29].

In recent years, RISs have arisen as a new technology component for 6G [22]. An RIS is a surface consisting of multiple reflecting elements that have sub-wavelength spacing and controllable reflection properties [23]. This feature provides partial control of the propagation environment that can lead to better services for users, especially when their serving BS is not in their LOS. By adjusting the impedances of the individual elements via a RIS controller, the elements are capable of adding desired phase shifts to the reflected signals, thereby forming reflected beams in desired directions that can significantly boost the SINR and reduce the symbol estimation error at the receiver [22, 30].

On the other hand, the addition of RISs to existing systems introduces new design and operational challenges [31]. For example, the length of the pilot signal required by a single UE is proportional to the number of RIS elements (e.g., tens or hundreds), because the RIS must change its configuration to explore all channel dimensions [17, 24]. In addition, the path loss of the reflected path through a passive RIS is proportional to the multiplication of the path losses to and from the RIS [25], so a larger surface is needed to achieve a decent SNR improvement. Active RISs, on the other hand, use amplifiers to overcome the large path loss but have the traditional issues of relays: increased power consumption, higher cost, and additional noise [32, 33]. While the aforementioned problems caused by the RIS have been recognized [26], pilot contamination caused by the presence of multiple RISs has not been studied in the literature.

Wireless communication systems use standardized protocols, interfaces, and well-defined pilot sequences and codebooks to ensure inter-operability [27]. While employing RISs in cellular networks have not been studied by the relevant standards organizations yet, it may be expected that the configuration sequences that facilitate the deployment of RISs while maintaining interoperability will be specified. Consequently, when multiple cellular networks are deployed by different network operators in overlapping geographical areas, the RISs may adopt identical or overlapping pilot sequences and cause pilot contamination. The number of orthogonal pilot sequences is limited by the length of the pilot sequence, and increasing the pilot sequence length not only creates more channel estimation overhead but also is infeasible due to the limited coherence budget of the channel. As a consequence, the need for repeating pilot sequences comes up very often. In this paper, we argue that when multiple RISs are deployed for the purpose of shaping the propagation characteristics of the environment, the propagation characteristics might change in unintended ways. For example, an RIS belonging

to another operator might modify the propagation of a UE's own pilot signal, leading to pilot contamination even in the absence of any interfering signals or intra-band pilot reuse. The underlying reason is that an RIS element—although designed for a particular frequency—does not act as a bandpass filter, but reflects all frequencies with varying amplitude and phase. Indeed, as pointed out in [34], due to the lack of baseband signal processing, the RIS reflects the impinging broadband signal with frequency-flat reflection coefficients. Therefore, in realistic system models of, for example, passive RIS assisted 5G New Radio systems, we need to take into account that the RIS inadvertently reflects the transmitted uplink signals of the user equipment devices in multiple bands as in [35], [36].

Specifically, in this paper, we identify this new pilot contamination phenomenon as a major practical challenge when multiple RIS assisted operator networks are deployed over a geographical area, including the important practical scenario of inter-operator site sharing [37], [38, 39]. In such an environment, a UE that transmits pilots to its serving BS via multiple RIS, which may change their configurations simultaneously, is exposed to new pilot-related ambiguities that have not been studied before. Since this phenomenon exacerbates the pilot contamination problem, it is clear that pilot contamination due to the presence of multiple RISs must be dealt with.

To the best of the authors' knowledge, the problem of inter-operator pilot contamination in RIS-aided wireless communication systems has not been addressed before, except in the preliminary version of this manuscript [15], which assumed deterministic rather than stochastically fading channels. In this paper, we derive the capacity lower bound of the system under pilot contamination and imperfect CSI assuming Rayleigh fading. Our major contributions can be summarized as follows:

- For the case when inter-operator pilot contamination is neglected, we provide a misspecified ML estimator under the assumption that all the channels in the system setup are deterministic. We also derive the resulting channel estimation MSE for different choices of the RIS configurations.
- Based on the obtained results for the channel estimation error under inter-operator pilot contamination, we provide the data signal estimation MSE for a misspecified MMSE estimator.
- In addition to deterministic channels, we also consider the case where the channels are Rayleigh fading with spatial correlation. For generic channel spatial covariances, we derive the misspecified MMSE estimator and the resulting MSE.
- Based on the channel estimation error model, obtained for spatially correlated Rayleigh fading channels, we derive a capacity lower bound given the channel estimates. Our numerical results show that the choice of RIS configurations during channel estimation makes a significant impact on the capacity lower bound.

The rest of the manuscript is organized as follows: in Section 3.2, we provide the received signal model, in Section 3.3, we provide the misspecified ML estimator where the inter-operator pilot contamination is neglected and the channels are assumed to be deterministic. Section 3.4 builds on top of section 3.3 by providing the data estimation MSE as a result of inter-operator pilot contamination. In Section 3.5, we derive the impact of inter-operator pilot contamination in closed-form for the case of spatially correlated Rayleigh-fading channels by considering the channel estimation MSE as our performance metric. Since the data estimation MSE has a dependence on individual channel realizations, an alternative performance metric for data transmission is needed to capture the behavior of fading channels. To this end, we derive the capacity lower bound under channel side information in Section 3.6. We provide the numerical results in Section 3.7, and conclude the manuscript in Section 3.8.

3.2 System Model

In this paper, we study the pilot contamination caused by the presence of multiple RISs by considering the uplink of a system consisting of two wide-band RISs, two single-antenna UEs, and two co-located single-antenna BSs. The UEs are subscribed to different operators and use non-overlapping frequency bands. Each RIS is dedicated to and controlled by a single operator, but both UE signals are reflected from both RISs. In this scenario, although there is no interference between the two UEs, both RISs affect both frequency bands.

Although the two BSs are closely located, their coupling effects are ignored due to their casings providing enough electromagnetic shielding. For co-located BSs, the coupling can be avoided by separating the BSs by 1.5 meters [40]. Inter-RIS coupling is also ignored since the RISs are far apart. While the coupling among the elements in a dense RIS affects the system behavior, it can generally be treated as part of the spatial channel correlation. We consider arbitrary spatial correlation in this paper and are not explicitly modeling the coupling to avoid convoluting the notation but focus on the inter-operator pilot contamination effect. However, explicit modeling of the coupling effect among the RIS elements can be done as in [41, 42] and is recommended for future work.

In Fig. 3.1, we graphically describe the system that we consider. The components associated with the two different operators are depicted in two different colors: blue BS, RIS, UE and the channels belong to operator 1, while the red ones belong to operator 2. The operators can potentially use site-sharing (as in the figure) to reduce deployment costs but transmit over two disjoint narrow frequency bands to their respective serving BSs. Each RIS has N reflecting elements, and is dedicated to and controlled by a single operator but affects both bands. To focus on the fundamentals of pilot contamination, we consider an environment where the direct UE-BS paths are blocked, while the UE-RIS and RIS-BS paths are operational. Since the BSs and RISs have fixed deployment locations, we

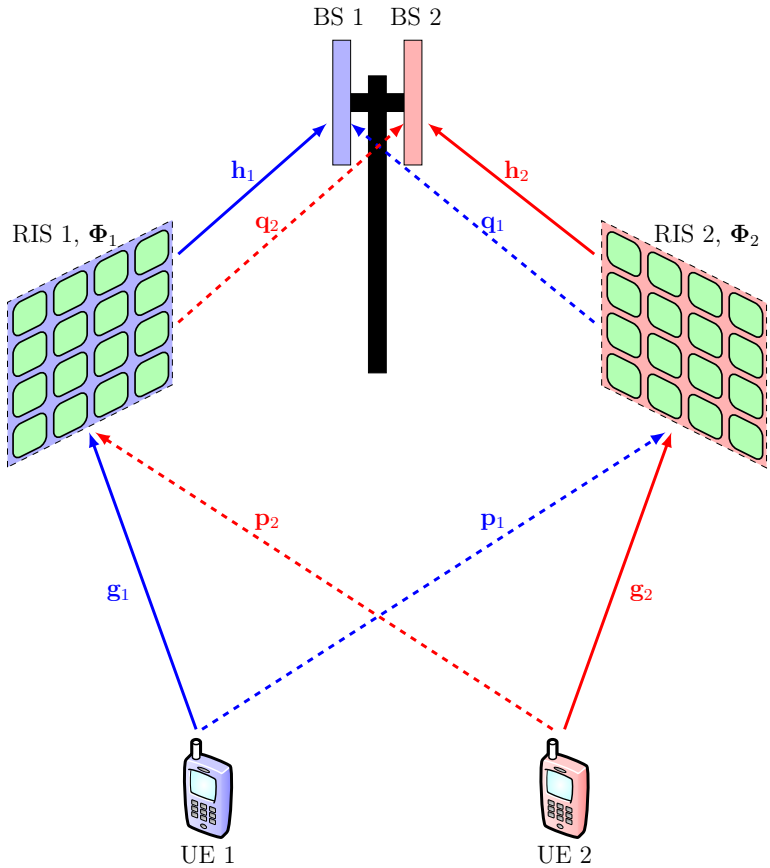

Figure 3.1: The considered setup with two UEs, two RISs, and two co-located single-antenna BSs. The blue channels correspond to frequency band 1, and the red channels correspond to frequency band 2, subscribed by UEs 1 and 2, respectively. The desired channels are denoted by solid lines, while the undesired channels (whose existences might be unknown to the BSs) are denoted by dashed lines. Each channel vector is N-dimensional because each RIS has N elements.

assume the RIS-BS channels $\mathbf{h}_k \in \mathbb{C}^N$ are known, while the UE-RIS channels $\mathbf{g}_k \in \mathbb{C}^N$ are unknown and to be estimated, for $k = 1, 2$.

The signal transmitted by UE k reaches its serving BS through the channels $\mathbf{h}_k$ and $\mathbf{g}_k$, for $k = 1, 2$. Importantly, each UE's transmitted signal is also reflected by the non-serving operator's RIS and parts of the reflected signal will reach the serving BS. This effect contaminates the pilot signal reflected by the serving RIS and we will study the implications. The phenomenon is illustrated in Fig. 3.1,

where the resulting UE-RIS and RIS-BS channels are denoted by $\mathbf{p}_k \in \mathbb{C}^N$ and $\mathbf{q}_k \in \mathbb{C}^N$, respectively, for $k = 1, 2$. Defining the pilot signal of UE k as $s_k \in \mathbb{C}$, the received signals on bands 1 and 2 at the BSs can be expressed as

$$y_{p1} = \sqrt{P_p}\mathbf{h}_1^T\mathbf{\Phi}_1\mathbf{g}_1 s_1 + \sqrt{P_p}\mathbf{q}_1^T\mathbf{\Phi}_2\mathbf{p}_1 s_1 + w_{p1}, \tag{3.1a}$$

$$y_{p2} = \sqrt{P_p}\mathbf{h}_2^T\mathbf{\Phi}_2\mathbf{g}_2 s_2 + \sqrt{P_p}\mathbf{q}_2^T\mathbf{\Phi}_1\mathbf{p}_2 s_2 + w_{p2}, \tag{3.1b}$$

where $y_{pk} \in \mathbb{C}$ denotes the received signal, $w_{pk} \sim \mathcal{CN}(0, 1)$ denotes the receiver noise for band k, and $\mathbf{\Phi}_k = \text{diag}(e^{-j\phi_{k1}}, \ldots, e^{-j\phi_{kN}})$ denotes the kth RIS's reflection matrix, and P_p denotes the pilot signal's transmission power. We assume $s_1 = s_2 = 1$ without loss of generality. When analyzing channel estimation, it is more convenient to rewrite (3.1) as

$$y_{p1} = \sqrt{P_p}\boldsymbol{\phi}_1^T\mathbf{D}_{\mathbf{h}_1}\mathbf{g}_1 + \sqrt{P_p}\boldsymbol{\phi}_2^T\mathbf{D}_{\mathbf{q}_1}\mathbf{p}_1 + w_{p1}, \tag{3.2a}$$

$$y_{p2} = \sqrt{P_p}\boldsymbol{\phi}_2^T\mathbf{D}_{\mathbf{h}_2}\mathbf{g}_2 + \sqrt{P_p}\boldsymbol{\phi}_1^T\mathbf{D}_{\mathbf{q}_2}\mathbf{p}_2 + w_{p2}, \tag{3.2b}$$

where $\mathbf{D}_{\mathbf{h}_k}$ and $\mathbf{D}_{\mathbf{q}_k}$ represent the $N \times N$ diagonal matrices containing the elements of $\mathbf{h}_k$ and $\mathbf{q}_k$, and $\boldsymbol{\phi}_k \in \mathbb{C}^N$ denotes the column vectors containing the diagonal entries of $\mathbf{\Phi}_k$ for $k = 1, 2$.

As there are N parameters in $\mathbf{g}_1$ and $\mathbf{g}_2$, at least N linearly independent observations are needed to estimate them uniquely. To this end, we perform $L \geq N$ pilot transmissions over time, and we vertically stack the received signals to obtain

$$\mathbf{y}_{p1} = \sqrt{P_p}\mathbf{B}_1\mathbf{D}_{\mathbf{h}_1}\mathbf{g}_1 + \sqrt{P_p}\mathbf{B}_2\mathbf{D}_{\mathbf{q}_1}\mathbf{p}_1 + \mathbf{w}_{p1}, \tag{3.3a}$$

$$\mathbf{y}_{p2} = \sqrt{P_p}\mathbf{B}_2\mathbf{D}_{\mathbf{h}_2}\mathbf{g}_2 + \sqrt{P_p}\mathbf{B}_1\mathbf{D}_{\mathbf{q}_2}\mathbf{p}_2 + \mathbf{w}_{p2}, \tag{3.3b}$$

where $\mathbf{y}_{pk} = [y_{pk}[1], \ldots, y_{pk}[L]]^T \in \mathbb{C}^L$ denotes the sequence of received signals from the kth UE over L time instances, and the matrices $\mathbf{B}_1$ and $\mathbf{B}_2$ represent the sequence of RIS configurations over L time instances; that is, $\mathbf{B}_k \triangleq \begin{bmatrix}\boldsymbol{\phi}_k[1] & \ldots & \boldsymbol{\phi}_k[L]\end{bmatrix}^T \in \mathbb{C}^{L\times N}$ for $k = 1, 2$.

Construction of $\mathbf{B}_1$ and $\mathbf{B}_2$

We consider $\mathbf{B}_1$ and $\mathbf{B}_2$ to be orthogonal matrices, that is, $\mathbf{B}_k^H\mathbf{B}_k = L\mathbf{I}_N$. Each entry of the matrices must have a unit modulus, and there are multiple designs that perform equally well. One way to design such matrices is to start from an L-dimensional Discrete Fourier Transform (DFT) matrix $\tilde{\mathbf{B}} \in \mathbb{C}^{L\times L}$. We need $L \geq N$ to estimate all channel components. After constructing $\tilde{\mathbf{B}}$, we perform the following operation:

- For $\mathbf{B}_1 = \mathbf{B}_2$, we assign the sub-matrix consisting of the first N column vectors of $\tilde{\mathbf{B}}$ to both $\mathbf{B}_1$ and $\mathbf{B}_2$.

- To obtain $\mathbf{B}_1^H \mathbf{B}_2 = \mathbf{0}$, we need at least $2N$ vectors that are orthogonal to each other, therefore, we need at least $L \geq 2N$. With this in mind, we assign the sub-matrix consisting of the first N columns of $\tilde{\mathbf{B}}$ and assign it to $\mathbf{B}_1$. Then we assign the sub-matrix consisting of the second N column vectors of $\tilde{\mathbf{B}}$ to $\mathbf{B}_2$. Consequently, for $L = 2N$, for example, we obtain

$$\tilde{\mathbf{B}} = \begin{bmatrix} \mathbf{B}_1 & \mathbf{B}_2 \end{bmatrix}. \tag{3.4}$$

Extension to Multiple-Antenna BSs

While we considered single-antenna base stations to focus on the multi-RIS pilot contamination phenomenon more, it is indeed possible to consider multi-antenna base stations. For example, suppose both base stations have M antennas. In this case, the pilot signal received at a single time instant at the k'th base station can be expressed as

$$\mathbf{y}_p = \sqrt{P_p}(\mathbf{H}_k \mathbf{\Phi}_k \mathbf{g}_k + \mathbf{Q}_k \mathbf{\Phi}_j \mathbf{p}_k) s_k + \mathbf{w}_k \in \mathbb{C}^{M \times 1}, \tag{3.5}$$

where $\mathbf{H}_k, \mathbf{Q}_k \in \mathbb{C}^{M \times N}$ denote the channel between RIS k and BS k and the channel between RIS j and BS k, respectively. Since $\mathbf{H}_k$ and $\mathbf{Q}_k$ are matrices (as opposed to vectors used in the manuscript), it is non-trivial to make the transition from (1) to (2). To this end, we define $\bar{\boldsymbol{\phi}}_n \triangleq \phi_n \mathbf{I}_{M \times M}$, $\boldsymbol{\phi}_k \triangleq [\bar{\boldsymbol{\phi}}_1, \ldots, \bar{\boldsymbol{\phi}}_N]$ and $\mathbf{D}_{\mathbf{H}_k} \triangleq \text{diag}(\mathbf{h}_k^{(1)}, \ldots, \mathbf{h}_k^{(N)})$ with $\mathbf{h}_k^{(n)}$ denoting the n'th $M \times 1$ column of

$$\mathbf{y}_p = \sqrt{P_p}(\boldsymbol{\phi}_k \mathbf{D}_{\mathbf{H}_k} \mathbf{g}_k + \boldsymbol{\phi}_j \mathbf{D}_{\mathbf{Q}_k} \mathbf{p}_k) s_k + \mathbf{w}_k \in \mathbb{C}^{M \times 1}, \tag{3.6}$$

which corresponds to eq. (3.2) in the multi-antenna BS setting. Without loss of generality, we assume that $s_k = 1$. After this step, we stack the $M \times 1$ received pilot observations over time vertically to obtain a $LM \times 1$ collection of pilot observations:

$$\mathbf{Y}_p = \sqrt{P_p}(\mathbf{B}_k \mathbf{D}_{\mathbf{H}_k} \mathbf{g}_k + \mathbf{B}_j \mathbf{D}_{\mathbf{Q}_k} \mathbf{p}_k) + \mathbf{W}_k \in \mathbb{C}^{LM \times 1}. \tag{3.7}$$

This equation corresponds to (3.3) in our manuscript. Note that the "cascaded" channels going over each RIS in this case correspond to $\mathbf{D}_{\mathbf{H}_k} \mathbf{g}_k \in \mathbb{C}^{MN \times 1}$, that is, the true dimensions of the channels are represented. It also has to be noted that $\mathbf{B}_k \in \mathbb{C}^{LM \times MN}$ in this case. Compared to the original $\mathbf{B}_k$ matrices in our manuscript, these $\mathbf{B}_k$ matrices are their Kronecker-multiplied versions, therefore, using the same dynamics with $L \geq 2N$ and DFT matrices, it is possible to obtain both $\mathbf{B}_1 = \mathbf{B}_2$ and $\mathbf{B}_1^H \mathbf{B}_2 = \mathbf{0}$. Since we assume that the static channels $\mathbf{H}_k$ and $\mathbf{Q}_k$ are known, we still have N unknown channel dimensions, hence we do not have additional complexity in configuring the RISs to estimate the unknown channels coming from having multiple antennas at the BSs.

In the remainder of this paper, we will analyze channel estimation and the resulting communication performance for deterministic and fading channels, respectively.

3.3 Maximum Likelihood Estimation of Deterministic Channels

In this section, we will consider channel estimation for deterministic channels. The same assumptions and results will then be considered in Section 3.4 for data transmission.

We assume that $\mathbf{g}_k$ is a deterministic and unknown channel without any known structure. That is, $\mathbf{g}_k$ is an $N \times 1$ vector of complex deterministic parameters to be estimated. In addition, we assume that $\mathbf{h}_k$ is perfectly known. On the other hand, the BSs do not know the existence of $\mathbf{q}_k$ and $\mathbf{p}_k$. We assume that the BSs are unable to obtain enough fading observations to construct a statistical model, therefore, the BSs employ the classical estimation framework. In contrast, we assume that statistics of the fading channels of interest $\mathbf{g}_1$ and $\mathbf{g}_2$ are available in Section 3.5, and we consider $\mathbf{h}_1$, $\mathbf{h}_2$, $\mathbf{q}_1$, and $\mathbf{q}_2$ to be deterministic since those links are between fixed deployments. On the other hand, we consider the statistics of the fading channels $\mathbf{p}_1$ and $\mathbf{p}_2$ only for MSE analysis, and assume that the BSs are unaware of these channels. We can denote the received signal models assumed by the BSs as

$$\hat{\mathbf{y}}_{p1} = \sqrt{P_p}\mathbf{B}_1\mathbf{D}_{\mathbf{h}_1}\mathbf{g}_1 + \mathbf{w}_{p1}, \tag{3.8a}$$

$$\hat{\mathbf{y}}_{p2} = \sqrt{P_p}\mathbf{B}_2\mathbf{D}_{\mathbf{h}_2}\mathbf{g}_2 + \mathbf{w}_{p2}. \tag{3.8b}$$

Since $\mathbf{g}_k$ does not have a known structure and hence consists of N scalars, BS k requires at least N independent observations to estimate it. To this end, both $\mathbf{B}_1, \mathbf{B}_2 \in \mathbb{C}^{L\times N}$ must have full column rank. Furthermore, we require that the RIS configurations used at different time instances are mutually orthogonal and contain entries on the unit circle that can be realized using a reflecting element. These assumptions result in $\mathbf{B}_k^H\mathbf{B}_k = L\mathbf{I}_N$. In classical non-Bayesian parameter estimation, the ML estimator is widely used, which maximizes the likelihood function of the received observation over the unknown parameter. Since the BSs have misspecified received pilot signal models, they will instead maximize the likelihood functions obtained from the misspecified model, leading to MML estimators. For (3.8), the MML estimator can be expressed as

$$\begin{aligned}
\hat{\mathbf{g}}_k &= \arg\max_{\mathbf{g}_k} f(\mathbf{y}_{pk}; \mathbf{g}_k) \\
&= \arg\max_{\mathbf{g}_k} \frac{1}{(\pi\sigma_w^2)^L} \exp\left(-\frac{\|\mathbf{y}_{pk} - \sqrt{P_p}\mathbf{B}_k\mathbf{D}_{\mathbf{h}_k}\mathbf{g}_k\|^2}{\sigma_w^2}\right) \\
&= \arg\min_{\mathbf{g}_k} \left\|\mathbf{y}_{pk} - \sqrt{P_p}\mathbf{B}_k\mathbf{D}_{\mathbf{h}_k}\mathbf{g}_k\right\|^2
\end{aligned} \tag{3.9}$$

$$= \frac{1}{\sqrt{P_p}} \mathbf{D}_{\mathbf{h}_k}^{-1} (\mathbf{B}_k^H \mathbf{B}_k)^{-1} \mathbf{B}_k^H \mathbf{y}_{pk}$$
$$= \frac{1}{L\sqrt{P_p}} \mathbf{D}_{\mathbf{h}_k}^{-1} \mathbf{B}_k^H \mathbf{y}_{pk}. \tag{3.10}$$

In the following subsections, we describe the behavior of this estimator for two different choices of the $\mathbf{B}_k$ matrices.

Case 1: The RISs Adopt the Same Configuration Sequence

We discussed in the introduction that in the absence of inter-operator cooperation, it is highly likely that the RISs will use the same standardized sequence of configurations during the channel estimation phase, which corresponds to $\mathbf{B}_1 = \mathbf{B}_2 = \mathbf{B}$.[1] In this case, (3.10) becomes

$$\hat{\mathbf{g}}_k = \mathbf{g}_k + \mathbf{D}_{\mathbf{h}_k}^{-1} \mathbf{D}_{\mathbf{q}_k} \mathbf{p}_k + \frac{1}{L\sqrt{P_p}} \mathbf{D}_{\mathbf{h}_k}^{-1} \mathbf{B}^H \mathbf{w}_{pk}. \tag{3.11}$$

Since we consider the channels as deterministic parameters, we obtain the probability distribution

$$\hat{\mathbf{g}}_k \sim \mathcal{CN}\left(\mathbf{g}_k + \mathbf{D}_{\mathbf{h}_k}^{-1} \mathbf{D}_{\mathbf{q}_k} \mathbf{p}_k, \frac{\sigma_w^2}{LP_p} (\mathbf{D}_{\mathbf{h}_k}^H \mathbf{D}_{\mathbf{h}_k})^{-1} \right). \tag{3.12}$$

We notice that $\hat{\mathbf{g}}_k$ is biased; that is, $\mathbf{b}_k \triangleq \mathbb{E}[\hat{\mathbf{g}}_k - \mathbf{g}_k] = \mathbf{D}_{\mathbf{h}_k}^{-1} \mathbf{D}_{\mathbf{q}_k} \mathbf{p}_k \neq \mathbf{0}$. The estimator bias does not vanish when increasing P_p or L, or decreasing σ_w^2. Hence, this estimator is not asymptotically unbiased. This is a new instance of an extensively studied phenomenon in the massive MIMO literature, namely pilot contamination [18, 19]. Interestingly, the RISs cause pilot contamination even between two non-overlapping frequency bands, which has not been recognized in the previous literature.

Case 2: The RISs Adopt Different Configuration Sequences

In this section, we consider the generic case of $\mathbf{B}_1 \neq \mathbf{B}_2$. To motivate the proposed method for configuring $\mathbf{B}_1$ and $\mathbf{B}_2$, we first consider the case where the BSs are aware of the true signal model in (3.3), and therefore can estimate both $\mathbf{g}_k$ and $\mathbf{r}_k \triangleq \mathbf{D}_{\mathbf{q}_k} \mathbf{p}_\mathbf{k}$. The resulting system model can be expressed as

$$\mathbf{y}_{p1} = \sqrt{P_p} \begin{bmatrix} \mathbf{B}_1 \mathbf{D}_{\mathbf{h}_1} & \mathbf{B}_2 \end{bmatrix} \begin{bmatrix} \mathbf{g}_1 \\ \mathbf{r}_1 \end{bmatrix} + \mathbf{w}_{p1}, \tag{3.13a}$$

$$\mathbf{y}_{p2} = \sqrt{P_p} \begin{bmatrix} \mathbf{B}_2 \mathbf{D}_{\mathbf{h}_2} & \mathbf{B}_1 \end{bmatrix} \begin{bmatrix} \mathbf{g}_2 \\ \mathbf{r}_2 \end{bmatrix} + \mathbf{w}_{p2}. \tag{3.13b}$$

[1] The analysis in this paper can be easily extended to the case when $\mathbf{B}_1 = \mathbf{U}\mathbf{B}_2$ for some unitary matrix $\mathbf{U}$, so that the configuration sequences have identical spans. It is the overlap of the spans that can cause issues.

In (3.13), a known linear transformation is applied to the parameter vector of interest in the presence of additive noise. Consequently, the ML estimates of UE 1's channels become

$$\begin{bmatrix}\hat{\mathbf{g}}_1\\ \hat{\mathbf{r}}_1\end{bmatrix} = \frac{1}{\sqrt{P_p}}\begin{bmatrix}L\mathbf{D}_{\mathbf{h}_1}^H\mathbf{D}_{\mathbf{h}_1} & \mathbf{D}_{\mathbf{h}_1}^H\mathbf{B}_1^H\mathbf{B}_2\\ \mathbf{B}_2^H\mathbf{B}_1\mathbf{D}_{\mathbf{h}_1} & L\mathbf{I}_N\end{bmatrix}^{-1}\begin{bmatrix}\mathbf{D}_{\mathbf{h}_1}^H\mathbf{B}_1^H\\ \mathbf{B}_2^H\end{bmatrix}\mathbf{y}_{p1}. \tag{3.14}$$

Note that in this case, the total dimension of the unknown parameter vector is $2N$, hence, at least $2N$ independent observations are required for the matrix inverse to exist.[2] The structure in (3.14) applies to UE 2 with alternated indices, and it gives the ML estimator, which is both unbiased and efficient, since (3.13) is a linear observation model with additive Gaussian noise [28, Th. 7.3]. Hence, (3.14) is unbiased irrespective of other parameters such as σ_w^2, L, and P_p, and it achieves the CRLB, which provides a lower bound on the MSE of any unbiased estimator [12]. It has to be noted that when $\mathbf{B}_1^H\mathbf{B}_2 = \mathbf{0}$, (3.14) becomes

$$\begin{aligned}\begin{bmatrix}\hat{\mathbf{g}}_1\\ \hat{\mathbf{r}}_1\end{bmatrix} &= \frac{1}{L\sqrt{P_p}}\begin{bmatrix}\mathbf{D}_{\mathbf{h}_1}^H\mathbf{D}_{\mathbf{h}_1} & \mathbf{0}\\ \mathbf{0} & \mathbf{I}_N\end{bmatrix}^{-1}\begin{bmatrix}\mathbf{D}_{\mathbf{h}_1}^H\mathbf{B}_1^H\\ \mathbf{B}_2^H\end{bmatrix}\mathbf{y}_{p1}\\ &= \frac{1}{L\sqrt{P_p}}\begin{bmatrix}\mathbf{D}_{\mathbf{h}_1}^{-1}\mathbf{B}_1^H\\ \mathbf{B}_2^H\end{bmatrix}\mathbf{y}_{p1}.\end{aligned} \tag{3.15}$$

Note that the expression for $\hat{\mathbf{g}}_1$ in (3.15) is the same as in (3.10). This shows that when $\mathbf{B}_1^H\mathbf{B}_2 = \mathbf{0}$, the MML in (3.10) coincides with the ML estimator; that is, the misspecified model is sufficient when the configuration sequences are designed to alleviate pilot interference because the missing terms anyway vanish in the receiver processing. The probability distribution of $\hat{\mathbf{g}}_k$ in this case can be expressed as

$$\hat{\mathbf{g}}_k \sim \mathcal{CN}\left(\mathbf{g}_k, \frac{\sigma_w^2}{LP_p}(\mathbf{D}_{\mathbf{h}_k}^H\mathbf{D}_{\mathbf{h}_k})^{-1}\right), \tag{3.16}$$

which shows that choosing the RIS configuration sequences such that $\mathbf{B}_1$ and $\mathbf{B}_2$ remove the bias from the MML estimator. However, the major setback of this approach is that the minimum number of observations required for this channel estimation procedure is $2N$ instead of N, due to the fact that the $2N$-many L-dimensional columns must all be mutually orthogonal, for which $L \geq 2N$ is required. Considering that the estimator bias in (3.12) does not vanish with increasing L, this is a necessary sacrifice. Hence, it has to be noted that the number of pilot transmissions increases linearly with the number of RISs deployed in proximity.

MSE During Channel Estimation

The estimation error can be quantified through the MSE, which is the trace of the error covariance matrix. We will derive the MSE in this section. In this

[2]The pseudo-inverse could be used when there are fewer observations, but it will not provide a useful estimate.

derivation, we do not assume a particular choice of $\mathbf{B}_1$ and $\mathbf{B}_2$, but we utilize the basic assumption $\mathbf{B}_k\mathbf{B}_k^H = L\mathbf{I}_N$. Consequently, we use $\mathbf{b}_k$ to denote the potential estimator bias. We can then compute the error covariance matrix as

$$\begin{aligned}\boldsymbol{\Sigma}_{e,k} &= \mathbb{E}\left[(\hat{\mathbf{g}}_k - \mathbf{g}_k)(\hat{\mathbf{g}}_k - \mathbf{g}_k)^H\right] \\ &= \mathbf{b}_k\mathbf{b}_k^H + \frac{1}{LP_p}\mathbb{E}\left[\mathbf{D}_{\mathbf{h}_k}^{-1}\mathbf{w}_{pk}\mathbf{w}_{pk}^H\mathbf{D}_{\mathbf{h}_k}^{-H}\right] \\ &= \mathbf{b}_k\mathbf{b}_k^H + \frac{\sigma_w^2}{LP_p}\left(\mathbf{D}_{\mathbf{h}_k}\mathbf{D}_{\mathbf{h}_k}^H\right)^{-1}. \end{aligned} \tag{3.17}$$

Consequently, the trace of the error covariance matrix becomes

$$\mathrm{tr}(\boldsymbol{\Sigma}_{e,k}) = \|\mathbf{b}_k\|^2 + \frac{\sigma_w^2}{LP_p}\sum_{n=1}^{N}\frac{1}{|h_{kn}|^2}. \tag{3.18}$$

Note that for high P_p, L, and/or low σ_w^2, the second term in (3.18) vanishes, and the trace of the error covariance converges to $\|\mathbf{b}_k\|^2$ which depends on the configurations of $\mathbf{B}_1, \mathbf{B}_2$. For the two previously considered cases, we have

$$\|\mathbf{b}_k\|^2 = \begin{cases} \sum_{n=1}^{N}\frac{|r_{kn}|^2}{|h_{kn}|^2} & \mathbf{B}_1 = \mathbf{B}_2, \\ 0 & \mathbf{B}_1^H\mathbf{B}_2 = \mathbf{0}. \end{cases} \tag{3.19}$$

This result shows that configuring the RISs such that $\mathbf{B}_1^H\mathbf{B}_2 = \mathbf{0}$ removes the asymptotic floor on the average MSE, which comes from the energy of the estimator bias. On the other hand, when the intended RIS-BS links $\mathbf{h}_1, \mathbf{h}_2$ are strong relative to the unintended and unknown overall link $\mathbf{r}_k$, the estimator bias will be weaker and the performance loss associated with choosing $\mathbf{B}_1 = \mathbf{B}_2$ will be lower. Nevertheless, pilot contamination results in a fundamental error floor, even if the RISs are utilized in different bands. In the next section, we consider the estimation of data based on the channel estimation performed in this section and analyze the consequence of pilot contamination in this phase.

3.4 Data Signal Estimation with Deterministic Channels

The channel estimation is followed by data transmission over the same deterministic channel as in Section 3.3. The receiver can use the channel estimate derived in the last section when determining the transmitted signal. Practical channels are never fully deterministic but might have a long coherence time. Moreover, the impact of estimation errors is only relevant when the data packet has a modest size so we cannot afford to spend much resources on pilots. For this reason, we cannot consider the channel capacity as performance metric but will instead consider the MSE.

Defining the data signal transmitted by the kth UE as $x_k \sim \mathcal{CN}(0,1)$, we can express the received data as

$$y_1 = \sqrt{P_d}(\mathbf{h}_1^T \hat{\mathbf{\Phi}}_1 \mathbf{g}_1 + \mathbf{q}_1^T \hat{\mathbf{\Phi}}_2 \mathbf{p}_1)x_1 + w_1, \tag{3.20a}$$

$$y_2 = \sqrt{P_d}(\mathbf{h}_2^T \hat{\mathbf{\Phi}}_2 \mathbf{g}_2 + \mathbf{q}_2^T \hat{\mathbf{\Phi}}_1 \mathbf{p}_2)x_2 + w_2, \tag{3.20b}$$

where $w_k \sim \mathcal{CN}(0, \sigma_w^2)$ denotes the receiver noise, P_d denotes the data transmission power, and the RIS configuration matrices $\hat{\mathbf{\Phi}}_k$ are selected based on the estimated channels to maximize the average gain of the desired cascaded channel as shown in [17, Sec. II]:

$$\begin{aligned} \hat{\phi}_{kn} &= \arg(h_{kn}) + \arg(\hat{g}_{kn}), \\ \hat{\mathbf{\Phi}}_k &= \operatorname{diag}\left(e^{-j\hat{\phi}_{k1}}, \ldots, e^{-j\hat{\phi}_{kN}}\right). \end{aligned} \tag{3.21}$$

Note that we use two different notations for the noise acting upon the pilot and data transmissions to emphasize that they are two distinct i.i.d. random variables which becomes an important fact when one considers data signal estimation based on finite-SNR channel estimates. However, since the BSs are unaware of the unintended reflections and base their data reception on the previously obtained channel estimates, they assume the following misspecified received data signal models:

$$\hat{y}_1 = \sqrt{P_d}\mathbf{h}_1^T \hat{\mathbf{\Phi}}_1 \hat{\mathbf{g}}_1 x_1 + w_1, \tag{3.22a}$$

$$\hat{y}_2 = \sqrt{P_d}\mathbf{h}_2^T \hat{\mathbf{\Phi}}_2 \hat{\mathbf{g}}_2 x_2 + w_2. \tag{3.22b}$$

Introducing the notation $m_k \triangleq \sqrt{P_d}(\mathbf{h}_k^T \hat{\mathbf{\Phi}}_k \mathbf{g}_k + \mathbf{q}_k^T \hat{\mathbf{\Phi}}_j \mathbf{p}_k)$ for $j,k \in \{1,2\}, j \neq k$, and $\hat{m}_k \triangleq \sqrt{P_d}\mathbf{h}_k^T \hat{\mathbf{\Phi}}_k \hat{\mathbf{g}}_k$, (3.20) and (3.22) can be expressed as

$$y_k = m_k x_k + w_k, \quad k = 1,2, \tag{3.23a}$$

$$\hat{y}_k = \hat{m}_k x_k + w_k, \quad k = 1,2. \tag{3.23b}$$

Based on the misspecified observation model in (3.23b), the BSs estimate x_k by using the misspecified MMSE estimator

$$\hat{x}_k = \frac{\hat{m}_k^*}{|\hat{m}_k|^2 + \sigma_w^2} y_k, \quad k = 1,2. \tag{3.24}$$

In this section, we consider the MSE between x_k and $\hat{x}_k$ as the performance metric for the data transmission. We derive the data estimation MSE for UE k

as

$$\begin{aligned}
&\mathbb{E}\left[|x_k-\hat{x}_k|^2\right]=1+\mathbb{E}\left[|\hat{x}_k|^2\right]-2\mathrm{Re}(\mathbb{E}[x_k\hat{x}_k^*])\\
&=1+\mathbb{E}\left[\frac{|\hat{m}_k|^2(|m_k|^2+\sigma_w^2)}{(|\hat{m}_k|^2+\sigma_w^2)^2}\right]\\
&-2\mathrm{Re}\left(\mathbb{E}\left[\frac{\hat{m}_k m_k^*}{|\hat{m}_k|^2+\sigma_w^2}\right]\right)\\
&=1+\mathbb{E}\left[\frac{|\hat{m}_k|^2(|m_k|^2+\sigma_w^2)-2\mathrm{Re}(\hat{m}_1 m_1^*)(|\hat{m}_k|^2+\sigma_w^2)}{(|\hat{m}_k|^2+\sigma_w^2)^2}\right]\\
&=1+\mathbb{E}\left[\frac{|\hat{m}_k|^2(|m_k|^2+\sigma_w^2)-2\mathrm{Re}(\hat{m}_1 m_1^*)(|\hat{m}_k|^2+\sigma_w^2)}{(|\hat{m}_k|^2+\sigma_w^2)^2}\right]\\
&+\mathbb{E}\left[\frac{\sigma_w^2(|m_k|^2+\sigma_w^2)-\sigma_w^2(|m_k|^2+\sigma_w^2)}{(|\hat{m}_k|^2+\sigma_w^2)^2}\right]\\
&=1+\mathbb{E}\left[\frac{(|\hat{m}_k|^2+\sigma_w^2)(|m_k|^2+\sigma_w^2-2\mathrm{Re}(\hat{m}_k m_k^*))}{(\hat{m}_k^2+\sigma_w^2)^2}\right]\\
&-\mathbb{E}\left[\frac{\sigma_w^2(|m_k|^2+\sigma_w^2)}{(\hat{m}_k^2+\sigma_w^2)^2}\right]\\
&=\mathbb{E}\left[\frac{|m_k-\hat{m}_k|^2+2\sigma_w^2}{|\hat{m}_k|^2+\sigma_w^2}\right]-\mathbb{E}\left[\frac{\sigma_w^2(|m_k|^2+\sigma_w^2)}{(|\hat{m}_k|^2+\sigma_w^2)^2}\right]. \qquad (3.25)
\end{aligned}$$

Defining $\epsilon_k \triangleq m_k-\hat{m}_k$, (3.25) can be rewritten as

$$\mathbb{E}[|x_k-\hat{x}_k|^2]=\mathbb{E}\left[\frac{|\epsilon_k|^2+2\sigma_w^2}{|m_k-\epsilon_k|^2+\sigma_w^2}-\frac{\sigma_w^2(|m_k|^2+\sigma_w^2)}{(|m_k-\epsilon_k|^2+\sigma_w^2)^2}\right]. \qquad (3.26)$$

To examine the impact of pilot contamination on the data estimation performance more clearly, we now consider channel estimation at high SNRs, so that the estimation error only comes from the estimator bias, i.e., pilot contamination. This happens when L or P_p is high and/or σ_w^2 is low, which results in the estimator covariances in (3.12) and (3.16) becoming zero. For notational convenience, we consider the case where P_p is arbitrarily large so that $\lim_{P_p\to\infty}\hat{\mathbf{g}}_k=\mathbf{g}_k+\mathbf{b}_k$, where

$$\mathbf{b}_k=\begin{cases}\mathbf{D}_{\mathbf{h}_k}^{-1}\mathbf{D}_{\mathbf{q}_k}\mathbf{p}_k & \mathbf{B}_1=\mathbf{B}_2,\\ \mathbf{0} & \mathbf{B}_1^H\mathbf{B}_2=\mathbf{0}.\end{cases} \qquad (3.27)$$

Data MSE with Channel Estimation at High SNR

In (3.26), ϵ_k and m_k are functions of $\hat{\mathbf{g}}_1$ and $\hat{\mathbf{g}}_2$, therefore as $\hat{\mathbf{g}}_1$ and $\hat{\mathbf{g}}_2$ converge to their means, ϵ_k and m_k become

$$\overline{m}_k=\sqrt{P_d}(\mathbf{h}_k^T\bar{\mathbf{\Phi}}_k\mathbf{g}_k+\mathbf{q}_k^T\bar{\mathbf{\Phi}}_j\mathbf{p}_k), \qquad (3.28a)$$

$$\bar{\epsilon}_k=\sqrt{P_d}(\mathbf{q}_k^T\bar{\mathbf{\Phi}}_j\mathbf{p}_k-\mathbf{h}_k^T\bar{\mathbf{\Phi}}_k\mathbf{b}_k), \qquad (3.28b)$$

for $j, k \in \{1, 2\}$ and $j \neq k$. $\bar{\boldsymbol{\Phi}}_k$ denotes the RIS configuration computed according to (3.21) with $\hat{\mathbf{g}}_k = \mathbf{g}_k + \mathbf{b}_k$. At high SNR, the MSE in (3.26) can be rewritten as

$$\text{MSE} = \frac{|\overline{\epsilon}_k|^2 + 2\sigma_w^2}{|\overline{m}_k - \overline{\epsilon}_k|^2 + \sigma_w^2} - \frac{\sigma_w^2(|\overline{m}_k|^2 + \sigma_w^2)}{(|\overline{m}_k - \overline{\epsilon}_k|^2 + \sigma_w^2)^2}. \tag{3.29}$$

This is a practically achievable limit since RIS-aided systems require long pilot sequences over a narrow bandwidth, thus, the effective SNR (proportional to $P_p L$) during pilot transmission can be much larger than in the data transmission phase.

Data MSE with Transmission at High SNR

In the previous section, we obtained the expression for the data MSE when the channels are estimated with a high pilot SNR, while the data transmission is done at an arbitrary SNR. To study the case when also the data transmission is conducted at a high SNR, we let $\sigma_w^2 \to 0$, which results in the limit

$$\lim_{\sigma_w^2 \to 0} \text{MSE} = \frac{|\overline{\epsilon}_k|^2}{|\overline{m}_k - \overline{\epsilon}_k|^2}. \tag{3.30}$$

Note that the resulting expression denotes the ratio between the estimated overall SISO channel $\hat{m}_k$'s power and the mismatch parameter ϵ_k's power. Recall that $\mathbf{b}_k$ depends on which sequence of RIS configurations is utilized. For $\mathbf{B}_1 = \mathbf{B}_2$, we can obtain ϵ_k as

$$\begin{aligned}
\epsilon_k &= \sqrt{P_d}\mathbf{q}_k^T \hat{\boldsymbol{\Phi}}_j \mathbf{p}_k - \sqrt{P_d}\mathbf{h}_k^T \hat{\boldsymbol{\Phi}}_k \mathbf{D}_{\mathbf{h}_1}^{-1} \mathbf{D}_{\mathbf{q}_1} \mathbf{p}_1 \\
&= \sqrt{P_d}\mathbf{q}_k^T \hat{\boldsymbol{\Phi}}_j \mathbf{p}_k - \sqrt{P_d}\hat{\boldsymbol{\phi}}_k \mathbf{D}_{\mathbf{h}_k} \mathbf{D}_{\mathbf{h}_k}^{-1} \mathbf{D}_{\mathbf{q}_1} \mathbf{p}_1 \\
&= \sqrt{P_d}\mathbf{q}_k^T \hat{\boldsymbol{\Phi}}_j \mathbf{p}_k - \sqrt{P_d}\hat{\boldsymbol{\phi}}_k \mathbf{D}_{\mathbf{q}_1} \mathbf{p}_1 \\
&= \sqrt{P_d}\mathbf{q}_k^T \hat{\boldsymbol{\Phi}}_j \mathbf{p}_k - \sqrt{P_d}\mathbf{q}_k^T \hat{\boldsymbol{\Phi}}_k \mathbf{p}_k \\
&= \sqrt{P_d}\mathbf{q}_k^T (\hat{\boldsymbol{\Phi}}_j - \hat{\boldsymbol{\Phi}}_k) \mathbf{p}_k.
\end{aligned} \tag{3.31}$$

On the other hand, $\mathbf{B}_1^H \mathbf{B}_2 = \mathbf{0}$ removes $\mathbf{b}_k$ for $k \in \{1, 2\}$. Consequently, we have

$$\epsilon_k = \begin{cases} \sqrt{P_d}\mathbf{q}_k^T (\hat{\boldsymbol{\Phi}}_j - \hat{\boldsymbol{\Phi}}_k) \mathbf{p}_k & \mathbf{B}_1 = \mathbf{B}_2, \\ \sqrt{P_d}\mathbf{q}_k^T \hat{\boldsymbol{\Phi}}_j \mathbf{p}_k & \mathbf{B}_1^H \mathbf{B}_2 = \mathbf{0}. \end{cases} \tag{3.32}$$

We notice that ϵ_k corresponds to only the unintended reflection path when $\mathbf{B}_1^H \mathbf{B}_2 = \mathbf{0}$. On the other hand, $\mathbf{B}_1 = \mathbf{B}_2$ yields an expression depending on the difference between the two RISs' configurations during data transmission. Since each RIS is configured based on the (estimated) channels of their respective users, it is highly unlikely that the configurations will be close. Moreover, it has to be noted that the RIS configuration of the non-serving RIS is different between the two cases since the channel estimates are also different.

3.5 Channel Estimation based on Correlated Rayleigh Fading Priors

We now switch focus to consider fading channels that can be modeled using the Bayesian framework. In this section, we consider channel estimation and assume that all the UE-RIS channels exhibit spatially correlated Rayleigh fading: $\mathbf{g}_k \sim \mathcal{CN}(\mathbf{0}, \mathbf{\Sigma}_{\mathbf{g}_k})$ and $\mathbf{p}_k \sim \mathcal{CN}(\mathbf{0}, \mathbf{\Sigma}_{\mathbf{p}_k})$. The covariance matrices $\mathbf{\Sigma}_{\mathbf{g}_k}, \mathbf{\Sigma}_{\mathbf{p}_k} \in \mathbb{C}^{N\times N}$ are generic positive semi-definite matrices. In addition, the BSs know $\mathbf{h}_k$ perfectly while they consider $\mathbf{q}_k$ as deterministic and unknown channels for $k = 1, 2$. The pilot transmission model assumed by the BSs for $k = 1, 2$ can be expressed as

$$\hat{\mathbf{y}}_{p1} = \sqrt{P_p}\mathbf{B}_1\mathbf{D}_{\mathbf{h}_1}\mathbf{g}_1 + \mathbf{w}_{p1} \in \mathbb{C}^L, \tag{3.33a}$$
$$\hat{\mathbf{y}}_{p2} = \sqrt{P_p}\mathbf{B}_2\mathbf{D}_{\mathbf{h}_2}\mathbf{g}_2 + \mathbf{w}_{p2} \in \mathbb{C}^L. \tag{3.33b}$$

Based on (3.33), the BSs can estimate $\mathbf{g}_k$ via a misspecified MMSE estimator, which can be expressed as

$$\hat{\mathbf{g}}_1 = \frac{1}{\sqrt{P_p}}\mathbf{\Sigma}_{\mathbf{g}_1}\mathbf{D}_{\mathbf{h}_1}^H\mathbf{B}_1^H \times \left(\mathbf{B}_1\mathbf{D}_{\mathbf{h}_1}\mathbf{\Sigma}_{\mathbf{g}_1}\mathbf{D}_{\mathbf{h}_1}^H\mathbf{B}_1^H + \frac{\sigma_w^2}{P_p}\mathbf{I}_L\right)^{-1}\mathbf{y}_{p1}, \tag{3.34a}$$
$$\hat{\mathbf{g}}_2 = \frac{1}{\sqrt{P_p}}\mathbf{\Sigma}_{\mathbf{g}_2}\mathbf{D}_{\mathbf{h}_2}^H\mathbf{B}_2^H \times \left(\mathbf{B}_2\mathbf{D}_{\mathbf{h}_2}\mathbf{\Sigma}_{\mathbf{g}_2}\mathbf{D}_{\mathbf{h}_2}^H\mathbf{B}_2^H + \frac{\sigma_w^2}{P_p}\mathbf{I}_L\right)^{-1}\mathbf{y}_{p2}. \tag{3.34b}$$

The diagonal entries of the error covariance matrix represent the MSEs of the corresponding channel entry. We first define $\mathbf{r}_k \triangleq \mathbf{D}_{\mathbf{q}_k}\mathbf{p}_k$, which results in $\mathbf{r}_k \sim \mathcal{CN}(\mathbf{0}, \mathbf{\Sigma}_{\mathbf{r}_k})$ where $\mathbf{\Sigma}_{\mathbf{r}_k} \triangleq \mathbf{D}_{\mathbf{q}_k}\mathbf{\Sigma}_{\mathbf{p}_k}\mathbf{D}_{\mathbf{q}_k}^H$. To simplify the representation of the channel estimation error covariance matrix, we introduce the following notation:

$$\mathbf{C}_{\mathbf{g}\hat{\mathbf{y}}} \triangleq \mathbb{E}[\mathbf{g}_k\hat{\mathbf{y}}_{pk}^H] = \mathbb{E}[\mathbf{g}_k\mathbf{y}_{pk}^H] = \sqrt{P_p}\mathbf{\Sigma}_{\mathbf{g}_k}\mathbf{D}_{\mathbf{h}_k}^H\mathbf{B}_k^H, \tag{3.35a}$$
$$\mathbf{C}_{\hat{\mathbf{y}}\hat{\mathbf{y}}} \triangleq \mathbb{E}[\hat{\mathbf{y}}_{pk}\hat{\mathbf{y}}_{pk}^H] = P_p\mathbf{B}_k\mathbf{D}_{\mathbf{h}_k}\mathbf{\Sigma}_{\mathbf{g}_k}\mathbf{D}_{\mathbf{h}_k}^H\mathbf{B}_k^H + \sigma_w^2\mathbf{I}_L, \tag{3.35b}$$
$$\mathbf{C}_{\mathbf{y}\mathbf{y}} \triangleq \mathbb{E}[\mathbf{y}_{pk}\mathbf{y}_{pk}^H] = \mathbf{C}_{\hat{\mathbf{y}}\hat{\mathbf{y}}} + P_p\mathbf{B}_j\mathbf{\Sigma}_{\mathbf{r}_k}\mathbf{B}_j^H. \tag{3.35c}$$

With this notation, the error covariance matrix can be represented as

$$\begin{aligned}
&\mathbb{E}[(\mathbf{g}_k - \hat{\mathbf{g}}_k)(\mathbf{g}_k - \hat{\mathbf{g}}_k)^H] = \\
&= \boldsymbol{\Sigma}_{\mathbf{g}_k} + \mathbf{C}_{\mathbf{g}\hat{\mathbf{y}}}\mathbf{C}_{\hat{\mathbf{y}}\hat{\mathbf{y}}}^{-1}\mathbf{C}_{\mathbf{y}\mathbf{y}}\mathbf{C}_{\hat{\mathbf{y}}\hat{\mathbf{y}}}^{-1}\mathbf{C}_{\mathbf{g}\hat{\mathbf{y}}}^H - 2\mathbf{C}_{\mathbf{g}\hat{\mathbf{y}}}\mathbf{C}_{\hat{\mathbf{y}}\hat{\mathbf{y}}}^{-1}\mathbf{C}_{\mathbf{g}\hat{\mathbf{y}}}^H \\
&= \boldsymbol{\Sigma}_{\mathbf{g}_k} + \mathbf{C}_{\mathbf{g}\hat{\mathbf{y}}}\mathbf{C}_{\hat{\mathbf{y}}\hat{\mathbf{y}}}^{-1}(\mathbf{C}_{\hat{\mathbf{y}}\hat{\mathbf{y}}} + P_p\mathbf{B}_j\boldsymbol{\Sigma}_{\mathbf{r}_k}\mathbf{B}_j^H)\mathbf{C}_{\hat{\mathbf{y}}\hat{\mathbf{y}}}^{-1}\mathbf{C}_{\mathbf{g}\hat{\mathbf{y}}}^H \\
&- 2\mathbf{C}_{\mathbf{g}\hat{\mathbf{y}}}\mathbf{C}_{\hat{\mathbf{y}}\hat{\mathbf{y}}}^{-1}\mathbf{C}_{\mathbf{g}\hat{\mathbf{y}}}^H \\
&= \underbrace{\boldsymbol{\Sigma}_{\mathbf{g}_k} - \mathbf{C}_{\mathbf{g}\hat{\mathbf{y}}}\mathbf{C}_{\hat{\mathbf{y}}\hat{\mathbf{y}}}^{-1}\mathbf{C}_{\mathbf{g}\hat{\mathbf{y}}}^H}_{\text{error covariance for } \mathbf{y}=\hat{\mathbf{y}}} + \underbrace{P_p\mathbf{C}_{\mathbf{g}\hat{\mathbf{y}}}\mathbf{C}_{\hat{\mathbf{y}}\hat{\mathbf{y}}}^{-1}\mathbf{B}_j\boldsymbol{\Sigma}_{\mathbf{r}_k}\mathbf{B}_j^H\mathbf{C}_{\hat{\mathbf{y}}\hat{\mathbf{y}}}^{-1}\mathbf{C}_{\mathbf{g}\hat{\mathbf{y}}}^H}_{\text{term coming from pilot contamination}}.
\end{aligned} \tag{3.36}$$

Note that the additive term in (3.36) coming from pilot contamination depends on $\boldsymbol{\Sigma}_{\mathbf{r}_k}$. If we consider the case where the channel $\mathbf{r}_k$ does not exist, that is, $\boldsymbol{\Sigma}_{\mathbf{r}_k} = \mathbf{0}$, then we would obtain the error covariance in the form of a typical MMSE estimation error covariance matrix. It is also important to address the dependence of the term coming from pilot contamination on P_p: while the terms $\mathbf{C}_{\mathbf{g}\hat{\mathbf{y}}}$ scale with $\sqrt{P_p}$ each, the terms $\mathbf{C}_{\hat{\mathbf{y}}\hat{\mathbf{y}}}^{-1}$ scale with $1/P_p$ each, and along with the leading P_p multiplier, we can see that P_p-dependent terms cancel each other out, hence leaving a non-vanishing pilot contamination term.

High-SNR Channel Estimation

Now, we investigate the behavior of the error covariance matrix in (3.36) when σ_w^2 is low or P_p is high. Note that the first term in (3.36) is already the error covariance matrix for an MMSE estimator without misspecification that estimates $\mathbf{g}_k$ based on the observation $\hat{\mathbf{y}}_{pk}$. Therefore, we know that this term vanishes at high SNR. Consequently, the asymptotic error covariance matrix is governed by the high-SNR behavior of the term coming from pilot contamination, that is

$$\begin{aligned}
&\lim_{\sigma_w^2\to 0} \mathbb{E}[(\mathbf{g}_k - \hat{\mathbf{g}}_k)(\mathbf{g}_k - \hat{\mathbf{g}}_k)^H] \\
&= \lim_{\sigma_w^2\to 0} P_p\mathbf{C}_{\mathbf{g}\hat{\mathbf{y}}}\mathbf{C}_{\hat{\mathbf{y}}\hat{\mathbf{y}}}^{-1}\mathbf{B}_j\boldsymbol{\Sigma}_{\mathbf{r}_k}\mathbf{B}_j^H\mathbf{C}_{\hat{\mathbf{y}}\hat{\mathbf{y}}}^{-1}\mathbf{C}_{\mathbf{g}\hat{\mathbf{y}}}^H \\
&= P_p^2\boldsymbol{\Sigma}_{\mathbf{g}_k}\mathbf{D}_{\mathbf{h}_k}^H\mathbf{B}_k^H\left(P_p\mathbf{B}_k\mathbf{D}_{\mathbf{h}_k}\boldsymbol{\Sigma}_{\mathbf{g}_k}\mathbf{D}_{\mathbf{h}_k}^H\mathbf{B}_k^H + \sigma_w^2\mathbf{I}_L\right)^{-1} \\
&\times \mathbf{B}_j\boldsymbol{\Sigma}_{\mathbf{r}_k}\mathbf{B}_j^H\left(P_p\mathbf{B}_k\mathbf{D}_{\mathbf{h}_k}\boldsymbol{\Sigma}_{\mathbf{g}_k}\mathbf{D}_{\mathbf{h}_k}^H\mathbf{B}_k^H + \sigma_w^2\mathbf{I}_L\right)^{-1}\mathbf{B}_k\mathbf{D}_{\mathbf{h}_k}\boldsymbol{\Sigma}_{\mathbf{g}_k} \\
&= \lim_{\sigma_w^2\to 0} \boldsymbol{\Sigma}_{\mathbf{g}_k}\mathbf{D}_{\mathbf{h}_k}^H\mathbf{B}_k^H\left(\mathbf{B}_k\mathbf{D}_{\mathbf{h}_k}\boldsymbol{\Sigma}_{\mathbf{g}_k}\mathbf{D}_{\mathbf{h}_k}^H\mathbf{B}_k^H + \frac{\sigma_w^2}{P_p}\mathbf{I}_L\right)^{-1} \\
&\times \mathbf{B}_j\boldsymbol{\Sigma}_{\mathbf{r}_k}\mathbf{B}_j^H\left(\mathbf{B}_k\mathbf{D}_{\mathbf{h}_k}\boldsymbol{\Sigma}_{\mathbf{g}_k}\mathbf{D}_{\mathbf{h}_k}^H\mathbf{B}_k^H + \frac{\sigma_w^2}{P_p}\mathbf{I}_L\right)^{-1}\mathbf{B}_k\mathbf{D}_{\mathbf{h}_k}\boldsymbol{\Sigma}_{\mathbf{g}_k}.
\end{aligned} \tag{3.37}$$

Note that since $\mathbf{B}_k^H\mathbf{B}_k = L\mathbf{I}_N$, the pseudoinverse corresponds to $\mathbf{B}_k^\dagger = \frac{1}{L}\mathbf{B}_k^H$. Consequently, we have

$$\begin{aligned}
&\lim_{\sigma_w^2\to 0}\mathbb{E}[(\mathbf{g}_k-\hat{\mathbf{g}}_k)(\mathbf{g}_k-\hat{\mathbf{g}}_k)^H]\\
&=\frac{1}{L^4}\boldsymbol{\Sigma}_{\mathbf{g}_k}\mathbf{D}_{\mathbf{h}_k}^H\mathbf{B}_k^H\mathbf{B}_k\mathbf{D}_{\mathbf{h}_k}^{-H}\boldsymbol{\Sigma}_{\mathbf{g}_k}^{-1}\mathbf{D}_{\mathbf{h}_k}^{-1}\mathbf{B}_k^H\\
&\quad\times\mathbf{B}_j\boldsymbol{\Sigma}_{\mathbf{r}_k}\mathbf{B}_j^H\mathbf{B}_k\mathbf{D}_{\mathbf{h}_k}^{-H}\boldsymbol{\Sigma}_{\mathbf{g}_k}^{-1}\mathbf{D}_{\mathbf{h}_k}^{-1}\mathbf{B}_k^H\mathbf{B}_k\mathbf{D}_{\mathbf{h}_k}\boldsymbol{\Sigma}_{\mathbf{g}_k}\\
&=\frac{1}{L^2}\mathbf{D}_{\mathbf{h}_k}^{-1}\mathbf{B}_k^H\mathbf{B}_j\boldsymbol{\Sigma}_{\mathbf{r}_k}\mathbf{B}_j^H\mathbf{B}_k\mathbf{D}_{\mathbf{h}_k}^{-H}. \qquad (3.38)
\end{aligned}$$

From (3.38), one can observe that the asymptotic behavior of the pilot contamination depends on the choice of $\mathbf{B}_1$ and $\mathbf{B}_2$. To analyze this, we consider two cases.

Case 1: $\mathbf{B}_1 = \mathbf{B}_2$

In this case, we have that $\mathbf{B}_k^H\mathbf{B}_j = L\mathbf{I}_N$ for $j,k = 1,2$ and $j \neq k$. Consequently, (3.38) becomes

$$\frac{1}{L^2}\mathbf{D}_{\mathbf{h}_k}^{-1}\mathbf{B}_k^H\mathbf{B}_j\boldsymbol{\Sigma}_{\mathbf{r}_k}\mathbf{B}_j^H\mathbf{B}_k\mathbf{D}_{\mathbf{h}_k}^{-H} = \mathbf{D}_{\mathbf{h}_k}^{-1}\boldsymbol{\Sigma}_{\mathbf{r}_k}\mathbf{D}_{\mathbf{h}_k}^{-H}. \qquad (3.39)$$

Note that this result does not depend on L, which implies that this channel estimation error caused by pilot contamination cannot be eliminated by increasing the number of pilots when $\mathbf{B}_1 = \mathbf{B}_2$.

The RISs are configured such that $\mathbf{B}_1^H\mathbf{B}_2 = \mathbf{0}$

In this case, $\mathbf{B}_k^H\mathbf{B}_j = \mathbf{0}$ for $k \neq j$ and $k,j \in \{1,2\}$. This implies that (3.38) is zero; thus, BS k can estimate $\mathbf{g}_k$ even without being aware of $\mathbf{r}_k$. Also note that (3.38) implies that any choice of $\mathbf{B}_1$ and $\mathbf{B}_2$ that does not satisfy $\mathbf{B}_1^H\mathbf{B}_2 = \mathbf{0}$ will result in pilot contamination while estimating correlated Rayleigh fading channels. We can summarize the high-SNR behavior of the channel estimation error covariance matrix as

$$\begin{aligned}
&\lim_{\sigma_w^2\to 0}\mathbb{E}[(\mathbf{g}_k-\hat{\mathbf{g}}_k)(\mathbf{g}_k-\hat{\mathbf{g}}_k)^H]\\
&\qquad=\begin{cases}\mathbf{D}_{\mathbf{h}_k}^{-1}\boldsymbol{\Sigma}_{\mathbf{r}_k}\mathbf{D}_{\mathbf{h}_k}^{-H} & \mathbf{B}_1=\mathbf{B}_2,\\ \mathbf{0} & \mathbf{B}_1^H\mathbf{B}_2=\mathbf{0}.\end{cases} \qquad (3.40)
\end{aligned}$$

This result shows that in order to estimate $\mathbf{g}_k$ reliably, it is necessary to configure the RISs such that $\mathbf{B}_1^H\mathbf{B}_2 = \mathbf{0}$. Note that (3.40) shows us that the cascaded channel over the foreign operator's RIS acts as channel estimation noise that does not vanish with high transmission power. Additionally, the link between the operator's own RIS and BS counteracts the noise component. This result is

also in line with the result obtained in Section 3.3, in (3.17), that is, when the channels get a prior distribution, $\mathbf{b}_k$ becomes a complex Gaussian random vector with the covariance matrix provided in (3.40).

3.6 Capacity Lower Bound for Reliable Communication under Imperfect CSI

In this section, we compute a lower bound on the ergodic capacity based on the imperfect CSI obtained in the previous section via channel estimation. In particular, we consider the impact of pilot contamination and the effect of the signal model misspecification on the channel capacity. We derive the channel capacity lower bound for the two cases considered in Section 3.5.

Capacity Lower Bound of a SISO Channel with Channel Side Information

Consider a generic SISO system with the following received signal model:

$$y = hx + w \tag{3.41}$$

with $w \sim \mathcal{CN}(0, \sigma_w^2)$ and $x \sim \mathcal{CN}(0, 1)$. Suppose that the receiver has partial information on h, denoted by Ω. Then the capacity lower bound is [13, Eq. 2.46]

$$C \geq \mathbb{E}_\Omega \left[\log_2 \left(1 + \frac{|\mathbb{E}[h|\Omega]|^2}{\mathrm{Var}(h|\Omega) + \mathrm{Var}(w|\Omega)} \right) \right]. \tag{3.42}$$

This bound is valid under certain conditions, which can be listed as follows [13, Section 2.3.5]:

- The noise w has zero-mean conditioned on Ω, that is, $\mathbb{E}[w|\Omega] = 0$.
- The transmitted signal x and the noise w are uncorrelated conditioned on Ω, that is, $\mathbb{E}[xw^*|\Omega] = \mathbb{E}[x|\Omega]\mathbb{E}[w^*|\Omega]$.
- The received signal hx and the noise w are uncorrelated conditioned on Ω, that is, $\mathbb{E}[hxw^*|\Omega] = \mathbb{E}[hx|\Omega]\mathbb{E}[w^*|\Omega]$.

In our setup, the data signal model for the two users can be expressed as

$$y_1 = \sqrt{P_d}(\mathbf{h}_1^T \mathbf{\Phi}_1 \mathbf{g}_1 + \mathbf{q}_1^T \mathbf{\Phi}_2 \mathbf{p}_1)x_1 + w_1, \tag{3.43a}$$

$$y_2 = \sqrt{P_d}(\mathbf{h}_2^T \mathbf{\Phi}_2 \mathbf{g}_2 + \mathbf{q}_2^T \mathbf{\Phi}_1 \mathbf{p}_2)x_2 + w_2, \tag{3.43b}$$

where $x_k \sim \mathcal{CN}(0, 1)$ denotes the transmitted data for $k = 1, 2$ and P_d denotes the data transmission power. During the data transmission phase, both RISs are configured to phase-align the cascaded channel, that is:

$$\phi_{kn} = \arg(h_{kn}) + \arg(\hat{g}_{kn}). \tag{3.44}$$

For both BSs, we consider the side information Ω as the knowledge of $\mathbf{\Phi}_1$, $\mathbf{\Phi}_2$, $\mathbf{h}_1$, $\mathbf{h}_2$, $\hat{\mathbf{g}}_1$, and $\hat{\mathbf{g}}_2$. Consequently, the outer expectation in (3.42) refers to the expectation with respect to the marginal distributions of $\hat{\mathbf{g}}_1$ and $\hat{\mathbf{g}}_2$.

Lemma 2. *The system setup described by the signal model in* (3.43) *that uses the RIS configurations described in* (3.44) *satisfies the three regularity conditions required by the capacity bound in* (3.42).

Proof. First, let us identify the h and w that we had defined in our system setup in (3.43):

$$h = \sqrt{P_d}(\mathbf{h}_k^T \mathbf{\Phi}_k \mathbf{g}_k + \mathbf{q}_k^T \mathbf{\Phi}_j \mathbf{p}_k) \tag{3.45a}$$

$$w = w_k \tag{3.45b}$$

We can now prove that the conditional mean of the noise conditioned on the channel side information, which we can describe as $\Omega = \hat{\mathbf{g}}_k$, is zero. Note that $\hat{\mathbf{g}}_k$ and w_k are independent: for $\mathbf{B}_1 = \mathbf{B}_2$, the less trivial case, we have that $\hat{\mathbf{g}_k} = \mathbf{g}_k + \mathbf{D}_{\mathbf{h}_k}^{-1}\mathbf{r}_k$, that is, no dependence on the noise. At lower SNRs, the vanishing components contain the realizations of the noise received during channel estimation, and considering the fact that the receiver noise is white over time, that does not affect the independence between $\hat{\mathbf{g}}_k$ and w_k either. Therefore, $\mathbb{E}[w_k|\hat{\mathbf{g}}_k] = \mathbb{E}[w_k] = 0$.

It is also straightforward to prove that the transmitted signal is uncorrelated with the noise conditioned on Ω due to the fact that x_k and w_k are independent of Ω individually. So the expression $\mathbb{E}[x_k w_k^*|\Omega]$ does not have anything that depends on Ω, i.e., $\mathbb{E}[x_k w_k^*|\Omega] = \mathbb{E}[x_k w_k^*] = \mathbb{E}[x_k]\mathbb{E}[w_k^*] = \mathbb{E}[x_k|\Omega]\mathbb{E}[w_k^*|\Omega]$ can be obtained, proving that x and w are uncorrelated with each other conditioned on Ω.

The last point is also quite straightforward since Ω does not contain any relations between the overall channel, the receiver noise, and the transmitted signal. Therefore it is easy to claim that this regularity condition also holds, hence the capacity bound provided in (3.42) is applicable to our system setup. □

Capacity Lower Bound with High-SNR Channel Estimates Available at the BSs

If we assume that the channel estimation is performed at a high SNR, we can model the channel estimation error according to (3.40). Consequently, we can express the channel estimates in terms of the true channels and the channel estimation error as

$$\hat{\mathbf{g}}_k = \mathbf{g}_k + \mathbf{e}_k, \tag{3.46}$$

where the channel estimation error is

$$\mathbf{e}_k = \begin{cases} \mathbf{0} & \mathbf{B}_1^H \mathbf{B}_2 = \mathbf{0}, \\ \mathbf{D}_{\mathbf{h}_k}^{-1}\mathbf{r}_k & \mathbf{B}_1 = \mathbf{B}_2. \end{cases} \tag{3.47}$$

Hence, BS k knows $\mathbf{g}_k$ perfectly if the RISs are configured such that $\mathbf{B}_1^H\mathbf{B}_2 = \mathbf{0}$ during channel estimation, and $\mathbf{e}_k = \mathbf{D}_{\mathbf{h}_k}^{-1}\mathbf{r}_k$ when $\mathbf{B}_1 = \mathbf{B}_2$. Also note that even when we have $\mathbf{B}_1 = \mathbf{B}_2$, the channel and the channel estimation error are independent. Consequently, we can rewrite the overall SISO channel as

$$v_k \triangleq \sqrt{P_d}(\boldsymbol{\phi}_k^T\mathbf{D}_{\mathbf{h}_k}\mathbf{g}_k + \boldsymbol{\phi}_j^T\mathbf{r}_k). \tag{3.48}$$

The mean of the overall SISO channel conditioned on the side information can be expressed as

$$\mathbb{E}[v_k|\Omega] = \sqrt{P_d}(\boldsymbol{\phi}_k^T\mathbf{D}_{\mathbf{h}_k}\mathbb{E}[\mathbf{g}_k|\hat{\mathbf{g}}_k] + \boldsymbol{\phi}_j^T\mathbb{E}[\mathbf{r}_k|\hat{\mathbf{g}}_k]) \tag{3.49}$$

Here, we can utilize the channel estimate structure provided by (3.46) and (3.47). Note that when we consider $\mathbb{E}[\mathbf{g}_k|\hat{\mathbf{g}}_k]$, it can be thought as estimating $\mathbf{g}_k$ based on observing $\hat{\mathbf{g}}_k$ since both $\mathbf{g}_k$ and $\mathbf{e}_k$ and they are independent from each other. The same goes for computing $\mathbb{E}[\mathbf{r}_k|\hat{\mathbf{g}}_k]$. Since the $\mathbf{g}_k - \hat{\mathbf{g}}_k$ and $\mathbf{r}_k - \hat{\mathbf{g}}_k$ are jointly Gaussian, the MMSE estimate, also known as the conditional mean estimate coincides with the linear minimum mean squared error (LMMSE) estimate, therefore, we can use the LMMSE formulation here:

$$\mathbb{E}[\mathbf{g}_k|\hat{\mathbf{g}}_k] = \mathbb{E}[\mathbf{g}_k\hat{\mathbf{g}}_k^H](\mathbb{E}[\hat{\mathbf{g}}_k\hat{\mathbf{g}}_k^H])^{-1}\hat{\mathbf{g}}_k \tag{3.50a}$$

$$\mathbb{E}[\mathbf{r}_k|\hat{\mathbf{g}}_k] = \mathbb{E}[\mathbf{r}_k\hat{\mathbf{g}}_k^H](\mathbb{E}[\hat{\mathbf{g}}_k\hat{\mathbf{g}}_k^H])^{-1}\hat{\mathbf{g}}_k \tag{3.50b}$$

which can be expressed more explicitly as

$$\mathbb{E}[\mathbf{g}_k|\hat{\mathbf{g}}_k] = \boldsymbol{\Sigma}_{\mathbf{g}_k}(\boldsymbol{\Sigma}_{\mathbf{g}_k} + \mathbf{D}_{\mathbf{h}_k}^{-1}\boldsymbol{\Sigma}_{\mathbf{r}_k}\mathbf{D}_{\mathbf{h}_k}^{-H})^{-1}\hat{\mathbf{g}}_k, \tag{3.51a}$$

$$\mathbb{E}[\mathbf{r}_k|\hat{\mathbf{g}}_k] = \begin{cases} \boldsymbol{\Sigma}_{\mathbf{r}_k}\mathbf{D}_{\mathbf{h}_k}^{-H}(\boldsymbol{\Sigma}_{\mathbf{g}_k} + \mathbf{D}_{\mathbf{h}_k}^{-1}\boldsymbol{\Sigma}_{\mathbf{r}_k}\mathbf{D}_{\mathbf{h}_k}^{-H})^{-1}\hat{\mathbf{g}}_k & \mathbf{B}_1 = \mathbf{B}_2, \\ \mathbf{0} & \mathbf{B}_1^H\mathbf{B}_2 = \mathbf{0}. \end{cases} \tag{3.51b}$$

On the other hand, the variance of v_k conditioned on $\hat{\mathbf{g}}_k$ can be expressed as

$$\begin{aligned} &\mathrm{Var}(v_k|\hat{\mathbf{g}}_k) = P_d\boldsymbol{\phi}_k^T\mathbf{D}_{\mathbf{h}_k}\mathrm{Var}(\mathbf{g}_k|\hat{\mathbf{g}}_k)\mathbf{D}_{\mathbf{h}_k}^H\boldsymbol{\phi}_k^* \\ &+ P_d\boldsymbol{\phi}_j^T\mathrm{Var}(\mathbf{r}_k|\hat{\mathbf{g}}_k)\boldsymbol{\phi}_j^* + 2\mathrm{Re}(\boldsymbol{\phi}_k^T\mathbf{D}_{\mathbf{h}_k}\mathbb{E}[\mathbf{g}_k\mathbf{r}_k^H|\hat{\mathbf{g}}_k]\boldsymbol{\phi}_j^*) \\ &- 2\mathrm{Re}(\boldsymbol{\phi}_k^T\mathbf{D}_{\mathbf{h}_k}\mathbb{E}[\mathbf{g}_k|\hat{\mathbf{g}}_k]\mathbb{E}[\mathbf{r}_k^H|\hat{\mathbf{g}}_k]\boldsymbol{\phi}_j^*) \end{aligned} \tag{3.52}$$

where $\mathbb{E}[\mathbf{g}_k|\hat{\mathbf{g}}_k]$ and $\mathbb{E}[\mathbf{r}_k|\hat{\mathbf{g}}_k]$ are provided by (3.51). In addition, we can use LMMSE formulation results for $\mathrm{Var}(\mathbf{g}_k|\hat{\mathbf{g}}_k)$ and $\mathrm{Var}(\mathbf{r}_k|\hat{\mathbf{g}}_k)$ which correspond to the error covariance matrices as a result of estimating $\mathbf{g}_k$ and $\mathbf{r}_k$ with an LMMSE estimator based on the observation $\hat{\mathbf{g}}_k$. Consequently, these two terms can be expressed as

$$\mathrm{Var}(\mathbf{g}_k|\hat{\mathbf{g}}_k) = \mathbb{E}[\mathbf{g}_k\mathbf{g}_k^H] - \mathbb{E}[\mathbf{g}_k\hat{\mathbf{g}}_k^H](\mathbb{E}[\mathbf{g}_k\hat{\mathbf{g}}_k^H])^{-1}\mathbb{E}[\hat{\mathbf{g}}_k\mathbf{g}_k^H], \tag{3.53a}$$

$$\mathrm{Var}(\mathbf{r}_k|\hat{\mathbf{g}}_k) = \mathbb{E}[\mathbf{r}_k\mathbf{r}_k^H] - \mathbb{E}[\mathbf{r}_k\hat{\mathbf{g}}_k^H](\mathbb{E}[\mathbf{r}_k\hat{\mathbf{g}}_k^H])^{-1}\mathbb{E}[\hat{\mathbf{g}}_k\mathbf{r}_k^H]. \tag{3.53b}$$

Computing the expectations above and also the cross-term $\mathbb{E}[\mathbf{g}_k\mathbf{r}_k^H|\hat{\mathbf{g}}_k]$, we can obtain the implicit expressions in (3.52) as

$$\mathrm{Var}(\mathbf{g}_k|\hat{\mathbf{g}}_k) = \boldsymbol{\Sigma}_{\mathbf{g}_k} - \boldsymbol{\Sigma}_{\mathbf{g}_k}(\boldsymbol{\Sigma}_{\mathbf{g}_k} + \mathbf{D}_{\mathbf{h}_k}^{-1}\boldsymbol{\Sigma}_{\mathbf{r}_k}\mathbf{D}_{\mathbf{h}_k}^{-H})^{-1}\boldsymbol{\Sigma}_{\mathbf{g}_k} \tag{3.54a}$$

$$\mathrm{Var}(\mathbf{r}_k|\hat{\mathbf{g}}_k) = \boldsymbol{\Sigma}_{\mathbf{r}_k} - \boldsymbol{\Sigma}_{\mathbf{r}_k}\mathbf{D}_{\mathbf{h}_k}^{-H}(\boldsymbol{\Sigma}_{\mathbf{g}_k} + \mathbf{D}_{\mathbf{h}_k}^{-1}\boldsymbol{\Sigma}_{\mathbf{r}_k}\mathbf{D}_{\mathbf{h}_k}^{-H})^{-1}\mathbf{D}_{\mathbf{h}_k}^{-1}\boldsymbol{\Sigma}_{\mathbf{r}_k} \tag{3.54b}$$

$$\mathbb{E}[\mathbf{g}_k\mathbf{r}_k^H|\hat{\mathbf{g}}_k] = \hat{\mathbf{g}}_k\hat{\mathbf{g}}_k^H(\boldsymbol{\Sigma}_{\mathbf{g}_k} + \mathbf{D}_{\mathbf{h}_k}^{-1}\boldsymbol{\Sigma}_{\mathbf{r}_k}\mathbf{D}_{\mathbf{h}_k}^{-H})^{-1}\boldsymbol{\Sigma}_{\mathbf{r}_k}\mathbf{D}_{\mathbf{h}_k}^{-H} - \mathbf{D}_{\mathbf{h}_k}^{-1}\boldsymbol{\Sigma}_{\mathbf{r}_k} \tag{3.54c}$$

for $\mathbf{B}_1 = \mathbf{B}_2$ and

$$\mathrm{Var}(\mathbf{g}_k|\hat{\mathbf{g}}_k) = \mathbf{0} \tag{3.55a}$$

$$\mathrm{Var}(\mathbf{r}_k|\hat{\mathbf{g}}_k) = \boldsymbol{\Sigma}_{\mathbf{r}_k} \tag{3.55b}$$

$$\mathbb{E}[\mathbf{g}_k\mathbf{r}_k^H|\hat{\mathbf{g}}_k] = \mathbf{0} \tag{3.55c}$$

for $\mathbf{B}_1^H\mathbf{B}_2 = \mathbf{0}$. Obtaining $\mathrm{Var}(w_k|\Omega) = \sigma_w^2$ is straightforward since w_k is independent from Ω. Also note that $\hat{\mathbf{g}}_k$ depends on the choice of $\mathbf{B}_1$ and $\mathbf{B}_2$. As a result, the capacity lower bound can be expressed as

$$C_k \geq \mathbb{E}_\Omega\left[\log_2\left(1 + \frac{|\mathbb{E}[v_k|\Omega]|^2}{\mathrm{Var}(v_k|\Omega) + \sigma_w^2}\right)\right] \tag{3.56}$$

with $\mathbb{E}[v_k|\Omega]$ and $\mathrm{Var}(v_k|\Omega)$ taking values according to the choice of $\mathbf{B}_1$ and $\mathbf{B}_2$.

3.7 Numerical Results

In this section, we provide numerical examples to demonstrate the implications of the analytical results obtained in Sections 3.3-3.6. First, we provide the numerical results for the channel and data estimation MSEs when deterministic channels are considered. For correlated Rayleigh fading, we demonstrate the impact of pilot contamination on channel estimation MSE and the resulting capacity lower bound.

Estimation Performance With Deterministic Channels

For deterministic channel estimation, we consider the normalized mean squared error (NMSE) as our performance metric. Moreover, we consider the results for a single UE, since the results for different UEs only differ by the channel realizations. For the deterministic channel $\mathbf{g}_k$, we obtain the NMSE as

$$\mathrm{NMSE} = \frac{\mathrm{MSE}}{\|\mathbf{g}_k\|^2}. \tag{3.57}$$

In Fig. 3.2, we plot (3.18) for different values of P_p, and we also provide the

Table 3.1: Parameters used in Figures 3.2 and 3.3.

Parameter	Value
P_p or P_d	$-30, -25, \ldots, 40$ dBm[3]
UE-RIS path loss	-80 dB
RIS-BS path loss	-60 dB
σ_w^2	-90 dBm
N	256
L	513

high-SNR floor for the case where $\mathbf{B}_1 = \mathbf{B}_2$. The set of parameters used to generate Fig. 3.2 and 3.3 are provided in Table 3.1. On the other hand, the range of transmission power in Fig. 3.6 is between -10 and 60 dBm. In addition, for Figs. 3.4, 3.5 and 3.6, we consider a 8×8 uniform rectangular array (URA) geometry with $\lambda/2$ spacing in both vertical and horizontal axes. Therefore, the parameter values $N = 64$ and $L = 128$ apply to those figures. Note that at lower transmission powers, the covariance matrix of the estimator acts dominantly, hence, both RIS configurations perform nearly the same. However, after $P_p = 20$ dBm, the power of the estimator bias starts to dominate, and the average MSE for $\mathbf{B}_1 = \mathbf{B}_2$ converges to the floor denoted by the black dashed line, which is given by (3.19). On the other hand, the average MSE for $\mathbf{B}_1^H \mathbf{B}_2 = \mathbf{0}$ does not stop there but keeps decreasing towards zero. As mentioned before, the MML estimators used by the BSs coincide with the true ML estimators when the RISs are configured such that $\mathbf{B}_1^H \mathbf{B}_2 = \mathbf{0}$.

Data Estimation with Deterministic Channels

In Fig. 3.3, the data estimation MSE performance with the two RIS pilot configurations is analyzed when the channel estimation SNR is high as in Section 3.4. That is, (3.29) is plotted for $\mathbf{B}_1 = \mathbf{B}_2$ and $\mathbf{B}_1^H \mathbf{B}_2 = \mathbf{0}$. In addition, the case where all of the channels are perfectly known is plotted to serve as the golden standard, labeled as *Perfect CSI*. However, even when all the channels are perfectly known, each RIS is assumed to be optimized independently according to the subscribed UE's CSI. Note that although the channel estimation SNR is high, $\mathbf{B}_1 = \mathbf{B}_2$ yields biased estimates of $\mathbf{g}_1$ due to pilot contamination caused by self-interference. On the other hand, $\mathbf{B}_1^H \mathbf{B}_2 = \mathbf{0}$ yields the true $\mathbf{g}_1$ as the estimate, however, since BS 1 is unaware of the path through the second RIS, the data estimate is biased, hence, there is still a high data transmission SNR floor. At around $P_d = 5$ dBm, $\mathbf{B}_1 = \mathbf{B}_2$ starts to approach the high-SNR floor. On the other hand, $\mathbf{B}_1^H \mathbf{B}_2 = \mathbf{0}$ does not suffer from the lack of awareness of the second

[3]The results for $P_p = 45, 50, 55,$ and 60 dBm are also demonstrated in Fig. 3.2 to display the high SNR floor more clearly.

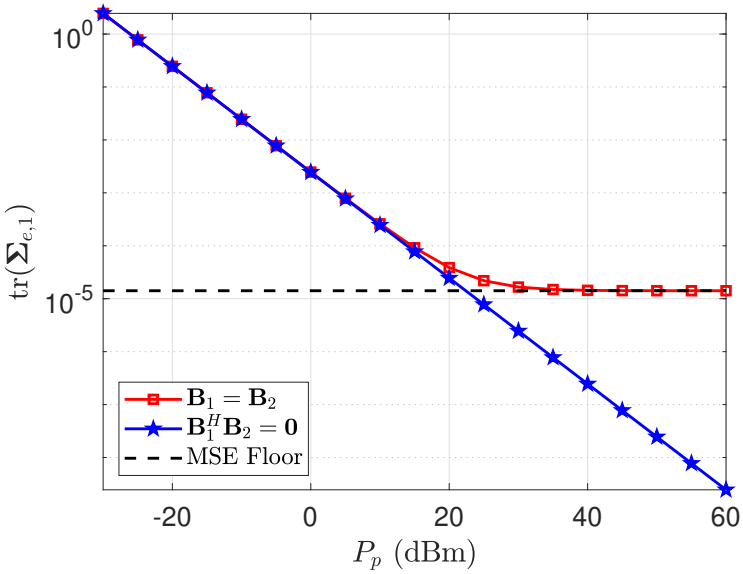

Figure 3.2: Pilot transmission power versus the channel estimation NMSE for deterministic channels. Since the prior distribution of the parameter vector is not considered in the non-random parameter estimation framework, it is highly likely to obtain NMSEs greater than 1.

RIS path until around $P_d = 20$ dBm. Hence, Fig. 3.3 clearly shows the benefit of configuring the RIS pilot configurations sequences orthogonally.

Channel Estimation Based on Correlated Rayleigh Fading Priors

In Fig. 3.4, the channel estimation performance with the two RIS pilot configurations are analyzed for correlated Rayleigh fading channels. Fig. 3.4 is generated by computing the trace of the channel estimation error covariance matrix provided in (3.36) and normalizing it by the factor of $\mathrm{tr}(\mathbf{\Sigma}_{\mathbf{g}_k})$ for different P_p values and different spatial channel correlation matrices. The spatial channel correlation matrices are computed for isotropic scattering based on the different RIS element geometries according to [43, Prop. 1]. Note that configuring the RISs such that $\mathbf{B}_1 = \mathbf{B}_2$ causes severe problems in channel estimation, that is, the MSE increases as pilot transmission power increases for all geometries while $\mathbf{B}_1^H\mathbf{B}_2 = \mathbf{0}$ completely eliminates pilot contamination. In addition, one can note that as the spatial correlation increases, channel estimation performance also increases since different channel parameters contain more information from one another.

Furthermore, in Fig. 3.5, we demonstrate the two different components of the channel estimation error in the presence of inter-operator pilot contamination.

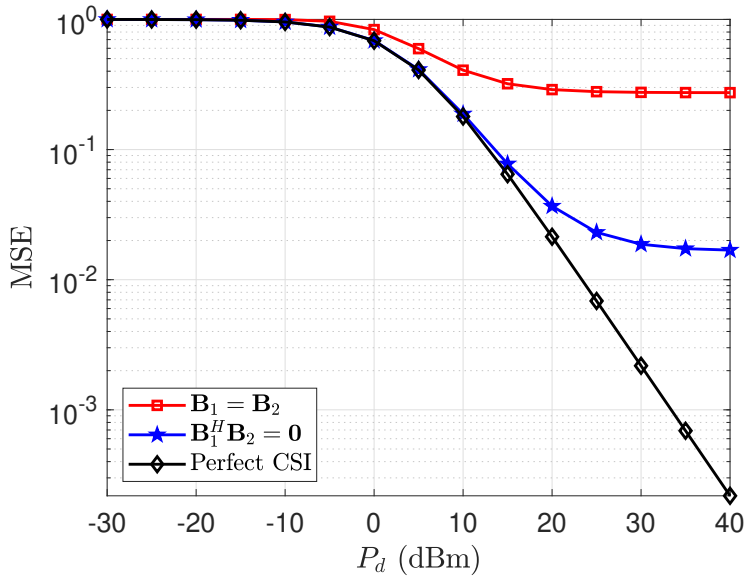

Figure 3.3: Data transmission power versus the data estimation NMSE for deterministic channels with high channel estimation SNR.

While the red curve corresponds to the total NMSE and the blue curve corresponds to the NMSE in the absence of pilot contamination as usual, the green curve demonstrates the term coming from pilot contamination, as in (3.36). On the other hand, the black dashed line represents the asymptote of the channel estimation NMSE in the presence of pilot contamination, which is provided by (3.40). Note that as the transmission power increases, the NMSE coming from pilot contamination also increases up to a certain point, and converges to the trace of (3.40) for $\mathbf{B}_1 = \mathbf{B}_2$ due to the fact that at very high transmission powers, the increase in pilot contamination cancels out with the increasing ability to estimating the channel.

Capacity Lower Bound for Reliable Communication Under Imperfect CSI

In Fig. 3.6, the capacity lower bound derived in Section 3.6 is plotted against the data transmission power. This is performed by generating several channel realizations and computing (3.42). Note that when $\mathbf{B}_1 = \mathbf{B}_2$, the capacity lower bound stops increasing after $P_d = 30$ dBm while this happens at around $P_d = 40$ dBm for $\mathbf{B}_1^H\mathbf{B}_2 = \mathbf{0}$ when the effect of the misspecified channel during data transmission starts to appear. In any case, it is clear that configuring the RISs such that $\mathbf{B}_1^H\mathbf{B}_2 = \mathbf{0}$ almost doubles the capacity lower bound. In addition,

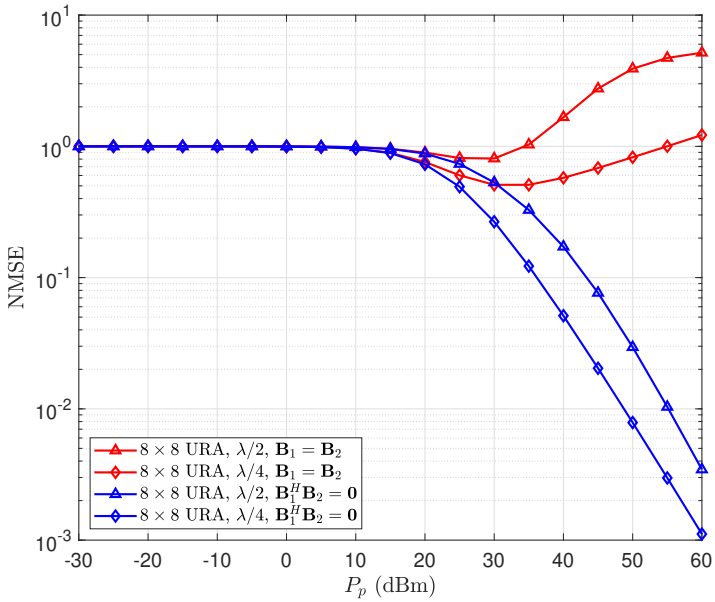

Figure 3.4: Pilot transmission power versus channel estimation MSE for different RIS geometries.

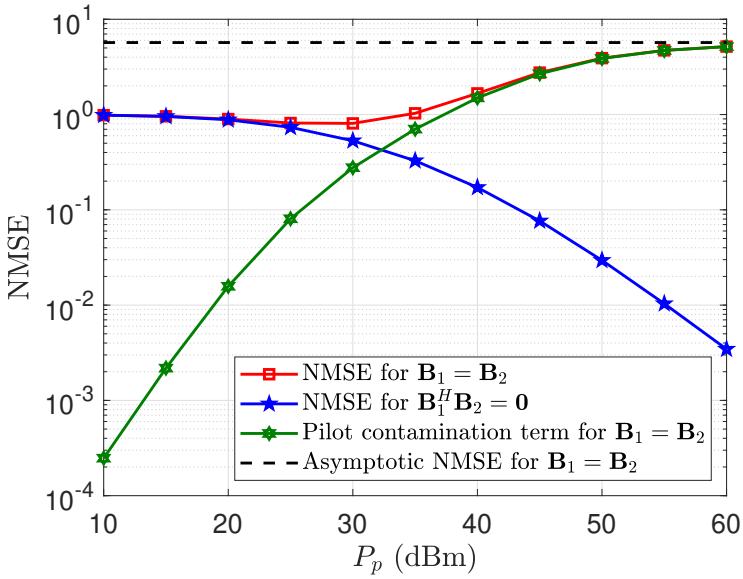

Figure 3.5: Different components of the channel estimation NMSE

we plotted the ergodic capacity to show the gap between the capacity bound and the achievable gold standard. We assume that each operator configures its RIS to maximize its user's capacity, and they ignore the inter-operator pilot contamination, that is:

$$\boldsymbol{\phi}_1 = \exp(-j(\arg(\mathbf{h}_1) + \arg(\mathbf{g}_1))), \tag{3.58a}$$
$$\boldsymbol{\phi}_2 = \exp(-j(\arg(\mathbf{h}_2) + \arg(\mathbf{g}_2))). \tag{3.58b}$$

With this in mind, we consider the overall SISO channels to be perfectly known, which we define as

$$v_1 \triangleq \mathbf{h}_1^T \boldsymbol{\Phi}_1 \mathbf{g}_1 + \mathbf{q}_1 \boldsymbol{\Phi}_2 \mathbf{p}_1, \tag{3.59a}$$
$$v_2 \triangleq \mathbf{h}_2^T \boldsymbol{\Phi}_2 \mathbf{g}_2 + \mathbf{q}_2 \boldsymbol{\Phi}_1 \mathbf{p}_2. \tag{3.59b}$$

Recall that while we consider $\mathbf{h}_k$ and $\mathbf{q}_k$ channels to be static, we consider $\mathbf{g}_k$ and $\mathbf{p}_k$ channels to be stochastic, therefore, the ergodic capacity expression contains an expectation with respect to these channels [44]:

$$C_k = \mathbb{E}_{\mathbf{g}_k, \mathbf{g}_j, \mathbf{p}_k} \left[\log_2 \left(1 + P_d \frac{|v_k|^2}{\sigma_w^2} \right) \right]. \tag{3.60}$$

Note that after $P_d = 30$ dBm, the gap in Fig. 3.6 between the ergodic capacity of the channel and the capacity lower bound based on the channel estimates grows significantly. At low transmission power, the dominant impeding factor is the noise, while as we transmit at higher powers, pilot contamination, and the signal model misspecification take over. This shows that inter-operator interference significantly degrades the system performance.

3.8 Conclusions

In this paper, we have studied the impact of pilot contamination in a system consisting of two wide-band RISs, two single-antenna UEs, and two co-located single-antenna BSs. We have demonstrated that the presence of multiple RISs in the same area causes pilot contamination, although the UEs are subscribed to different operators and transmit over disjoint narrow frequency bands. To combat this new type of pilot contamination, we have proposed the use of orthogonal RIS configurations during pilot transmission. For two different sets of assumptions, that is, deterministic and correlated Rayleigh-fading channel models, we have derived the channel and data estimation MSEs and the capacity lower bound in closed-form. In the numerical results, we have clearly shown that the proposed approach eliminates pilot contamination completely, and decreases data estimation MSE significantly for deterministic channels. On the other hand, we have also shown that the capacity lower bound almost doubles when the RISs are configured orthogonally during the pilot transmission step. While one might argue that this

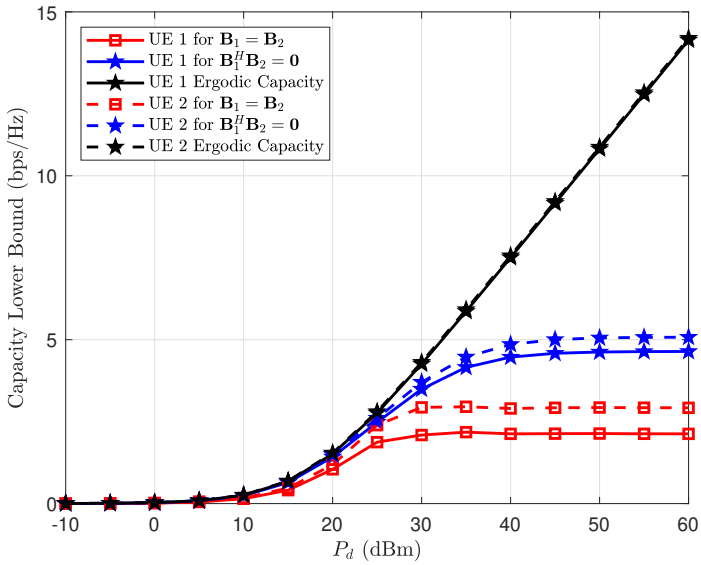

Figure 3.6: Data transmission power versus capacity lower bound and the ergodic capacity for the two users. Note that after $P_d = 30$ dBm, the gap between the ergodic capacity of the channel and the capacity lower bound based on the channel estimates grows significantly.

doubling comes at the expense of doubling the number of pilots, the estimates can be used for many data transmissions if the channel is static enough, resulting in a higher overall data rate. While this study covers the channel estimation performance in multi-operator RIS-based pilot contamination scenarios for both deterministic and stochastic channels, further analysis is needed for parametric channel models, which opens a new set of possibilities.

Chapter 4

Receive Beamforming Schemes to Mitigate Inter-Operator Pilot Contamination in RIS-Aided MIMO Networks

Abstract

When reconfigurable intelligent surfaces (RISs) are integrated into cellular networks, they can give rise to inter-operator pilot contamination, severely degrading network performance. While combatting this effect is possible by orthogonalizing the RIS configurations, it requires inter-operator coordination and limits the degree of configuration freedom per RIS. Therefore, in this work, we explore the use of receive beamforming to mitigate inter-operator pilot contamination in RIS-aided multiple input multiple output (MIMO) systems, where two operators share infrastructure and deploy RISs to enhance network coverage. We focus on uplink channel estimation and data transmission and propose a method in which the base stations (BSs) apply a novel kind of receive beamforming to suppress pilot-contaminated interference. We compare our proposed method with the previous RIS orthogonalization approach and an approach that does not eliminate inter-operator pilot contamination by formulating two schemes: In Scheme 1, the BS beamforms towards its intended channel without nulling the interfering channel while orthogonal RIS configurations mitigate pilot contamination. In Scheme 2, the BS nulls the interfering channel, removing the need for orthogonalized RIS configurations and halving the number of pilots. In the baseline scheme, the BS uses the same beamformer as Scheme 1 and the same RIS configurations as Scheme 2, hence does not eliminate pilot contamination. We assess the performance of both schemes under different channel conditions, in terms of channel estimation mean square error (MSE) and capacity bounds with imperfect channel state information. Our numerical results indicate that Scheme 2 offers a superior

rate at high signal-to-noise ratios (SNRs) due to fewer pilots and comparable channel estimation accuracy, while Scheme 1 performs better at very low SNRs due to capturing more energy. However, the reduced number of pilots in Scheme 2 makes it a favorable choice for practical systems, with minimal performance loss at low SNR. Overall, the proposed beamforming approach effectively mitigates inter-operator pilot contamination.

4.1 Introduction

In the past few decades, MIMO systems have changed the way we communicate [45], [46]. As they became prevalent due to the large-scale deployments by multiple operators, they made a revolutionary impact on the achievable performance of mobile broadband services [47]. Thanks to the multiple antennas, wireless channels gained multiple spatial degrees-of-freedom allowing for spatial diversity and multiplexing schemes that improve signal quality and enable to serve multiple users using fewer resources over time and frequency [48]. In addition, the presence of multiple antennas gave rise to an effect called channel hardening, which made the channels with more antennas less random, resulting in lower outage probabilities and hence increased reliability [43]. As a result, MIMO technology became a game changer in communication systems allowing for higher spectral efficiency and increased throughput. As a result, it allowed data-heavy use cases – such as high-quality audio and video streaming services – to become a reality. In the 5G era, MIMO has evolved into massive MIMO with a larger number of antennas, where the beamforming and spatial multiplexing capabilities of MIMO systems can be further utilized [29, 49, 50].

Receive beamforming techniques for interference cancellation and performance enhancement have been extensively studied in various wireless communication scenarios. The MRC introduced in [51] gives the beamforming vector that maximizes the received power for a particular channel. This approach focuses the receiver beam toward the incoming signals and adjusts its focus according to the signals' power levels. However, MRC does not eliminate interfering signals, which proves to be problematic when the interfering signals are closely aligned with the intended signals. The concept of null forming is introduced in [52] to overcome this problem. In the context of modern wireless communication systems involving MIMO channels, beamforming to collect the maximum power from a channel involves beamforming according to the dominant singular vectors of the channel of interest. In contrast, null forming involves orthogonalizing the beamforming vector to the singular vectors of the interfering channel corresponding to its nonzero singular values. While this approach eliminates interference, it sacrifices the power collected from the intended channel depending on how closely the intended signal and the interference are aligned. Since both MRC and null forming depend on the channel responses, they rely on high-quality channel estimates. It is typical to see a tradeoff between the two goals and MMSE methods are developed to achieve a balance between them.

While the benefits of massive MIMO systems are numerous and obvious, they have to deal with a potential problem that may limit their performance in practice, namely pilot contamination [18]. When multiple users use the same pilot sequences simultaneously in the same band, due to the limited channel coherence time, the BS cannot distinguish their channels. This typically results in poor channel estimates and extra beamformed interference from or towards the UEs that reuse the same pilot sequence. Therefore, pilot contamination adversely affects the coherent reception of data, and methods to mitigate pilot contamination –including adaptive pilot reuse, power control, user grouping, multi-cell coordination, and coded random access techniques– have been widely studied in the communication literature [18–21, 29].

As recent works on the techno-economic aspects of communication networks indicated [53–56], site and infrastructure sharing can help mobile network operators (MNOs) to reduce their capital and operational expenditures. For example, reference [54] concluded that infrastructure sharing between MNOs—which can involve mast or site sharing or co-locating cellular BSs on the roof of the same building— in rural or urban environments may significantly reduce expenditures. The level of cost savings due to infrastructure sharing depends on the revenue per user, service adoption rate and the amount of existing site infrastructure.

RISs are emerging as a promising technology for enhancing wireless communication systems. RISs consist of numerous controllable reflecting elements that can manipulate electromagnetic waves, enabling functions such as reflective beamforming and wireless power transfer [57]. These surfaces can be reflective, transmissive, or hybrid, operating at high frequencies to overcome signal attenuation and blockage [58], [59]. RISs offer potential applications in improving spectrum efficiency, coverage extension, and energy efficiency for wireless communications, as well as RF sensing for security and smart spaces [60]. Recent advancements include wave-controlled architectures that reduce hardware requirements while maintaining adaptability [61].

Despite their potential, RISs face challenges in implementation and integration with existing systems. One of the main reasons is the increased complexity of channel estimation due to the presence of RISs. The channel dimensions are multiplied by the number of RIS elements, hence the number of pilot transmissions to estimate the channels increases significantly [62–64]. The RIS must change its configuration to explore all channel dimensions [17, 24]. In addition, the path loss of the reflected path through a RIS is proportional to the multiplication of the path losses to and from the RIS [25], so a larger surface is needed to achieve a decent SNR improvement.

Another hurdle in front of integrating RISs into practical communication systems is a newly discovered phenomenon called inter-operator pilot contamination, which arises from multiple operators sharing sites utilizing RISs at the same time with identical sequences of RIS configurations. When a user's signal gets reflected from the other operator's RIS towards the BS, the additional reflection path cannot be resolved from the intended reflection path, resulting in inter-operator pilot

contamination. The main difference between traditional pilot contamination and inter-operator pilot contamination is that the former is caused by different users using the same pilot sequence in the same band, while the latter is caused by the reflections of a single user's pilot signal from multiple RISs belonging to different operators using neighboring bands. This problem was first identified in [15]. In that work, however, only deterministic channels were considered, and the performance metrics were not applicable to fading channels. In [16], reference [15] was extended to fading channels, and the inter-operator pilot contamination phenomenon was examined through ergodic capacity-based metrics. In [65], inter-operator pilot contamination was studied under discrete phase shifts and various channel conditions. While both [15] and [16] proposed to orthogonalize the RIS configurations by doubling the number of pilot transmissions to eliminate inter-operator pilot contamination, no practically useful methods were introduced to address this problem to the best of the authors' knowledge.

To address the lack of a practical solution to the inter-operator pilot contamination problem, in this paper, we propose the use of receive beamforming (note that [15] and [16] only considered single-antenna BSs) to eliminate inter-operator pilot contamination. Our scheme allows us to eliminate this phenomenon without doubling the number of pilots to be transmitted.

Contributions

The contributions of this paper can be summarized as follows:

- We propose a BS-based solution to the inter-operator pilot contamination problem that completely eliminates pilot contamination and allows the operators to manage their RISs independently.
- We provide the beamforming vectors necessary for the proposed scheme in closed form in both single- and multi-user cases.
- We compare the proposed scheme with a scheme inspired by [16] where the RISs are jointly configured to be orthogonal, hence eliminating the inter-operator pilot contamination at the expense of doubling the number of transmitted pilots.
- For both the proposed scheme and the alternative scheme based on [16], we provide the MMSE channel estimators and their error covariance matrices in closed form.
- Based on the channel estimators and their covariances, we provide the capacity lower bounds for both schemes under imperfect CSI, for which we provide the mean and the variance of the channel conditioned on the channel estimates in closed form.
- We provide numerical examples to compare the performances of two schemes to demonstrate their advantages and disadvantages.

Organization

We describe the system model in Section 4.2. In Section 4.4, we derive the receive beamforming vectors for both MR beamforming and for MR beamforming with null forming towards the interfering channels, when both RIS-BS channels are pure-LOS. In Section 4.5, we derive the receive beamforming vectors for unstructured RIS-BS channels based on the Singular Value Decomposition (SVD). In Section 4.6, we derive the MMSE estimators for both schemes and derive the error covariance matrices in closed form. Based on the analysis in this section, we provide the capacity lower bound under imperfect CSI for both schemes in Section 4.7, along with the ergodic capacities under perfect CSI. In Section 4.8, we demonstrate the extension of the beamforming schemes in Section 4.5 to the case of multiple users. We present our numerical results in Section 4.9 and conclude the paper in Section 4.10.

4.2 System Model

We consider a single-cell system where two operators share a single site for BS deployment. Each operator employs an M-antenna BS and serves a single user with the help of an N-element RIS where $M \geq N$. The UEs transmit L pilots over time to explore the different dimensions of the channel. A graphical description of the system is provided in Fig. 4.1.

The pilot signal $y_{pk}[l] \in \mathbb{C}$ received by the k-th operator's BS at a single time instant l after receive beamforming can be expressed as

$$y_{pk}[l] = \sqrt{P_p}\mathbf{v}_k^T(\mathbf{H}_k\mathbf{\Phi}_k[l]\mathbf{g}_k + \mathbf{Q}_k\mathbf{\Phi}_j[l]\mathbf{p}_k)s_k[l] + \underbrace{\mathbf{v}_k^T\mathbf{n}_k[l]}_{\triangleq w_k[l]}, \tag{4.1}$$

for $l = 1, \ldots, L$, where $\mathbf{H}_k, \mathbf{Q}_k \in \mathbb{C}^{M\times N}$ denote the channel between RIS k and BS k and the channel between RIS j and BS k, respectively. Although they have the potential to provide additional received signal power, the channels $\mathbf{Q}_k$ for $k = 1, 2$ are considered as interference since the behavior of another operator's RIS cannot be controlled by the operator of interest. Note that since the BSs and the RISs have fixed deployments, it is assumed that both $\mathbf{H}_k$ and $\mathbf{Q}_k$ are known by the BSs. $s_k[l]$ denotes the pilot transmitted by the UE subscribed to the k-th operator at the l-th time instant, and P_p denotes the pilot transmission power. $\mathbf{\Phi}_k[l] = \text{diag}(e^{-j\phi_{k,1}[l]}, \ldots, e^{-j\phi_{k,N}[l]})$ denotes the configuration of the RIS at the l-th time instant belonging to the k-th operator. $\mathbf{n}_k[l] \in \mathbb{C}^{M\times 1} \sim \mathcal{CN}(\mathbf{0}, \sigma_w^2\mathbf{I}_M)$ denotes the noise in the receiver. $\mathbf{v}_k \in \mathbb{C}^{M\times 1}$ denotes the receive beamforming vector employed by the k-th operator with $\|\mathbf{v}_k\| = 1$. Note that $w_k[l] = \mathbf{v}_k^T\mathbf{n}_k[l] \sim \mathcal{CN}(0, \sigma_w^2)$ since $\|\mathbf{v}_k\| = 1$. To express (4.1) in a more compact form, we define $\tilde{\mathbf{h}}_k^T \triangleq \mathbf{v}_k^T\mathbf{H}_k$ and $\tilde{\mathbf{q}}_k^T \triangleq \mathbf{v}_k^T\mathbf{Q}_k$, resulting in

$$y_{pk}[l] = \sqrt{P_p}(\tilde{\mathbf{h}}_k^T\mathbf{\Phi}_k[l]\mathbf{g}_k + \tilde{\mathbf{q}}_k^T\mathbf{\Phi}_j[l]\mathbf{p}_k)s_k[l] + w_k[l]. \tag{4.2}$$

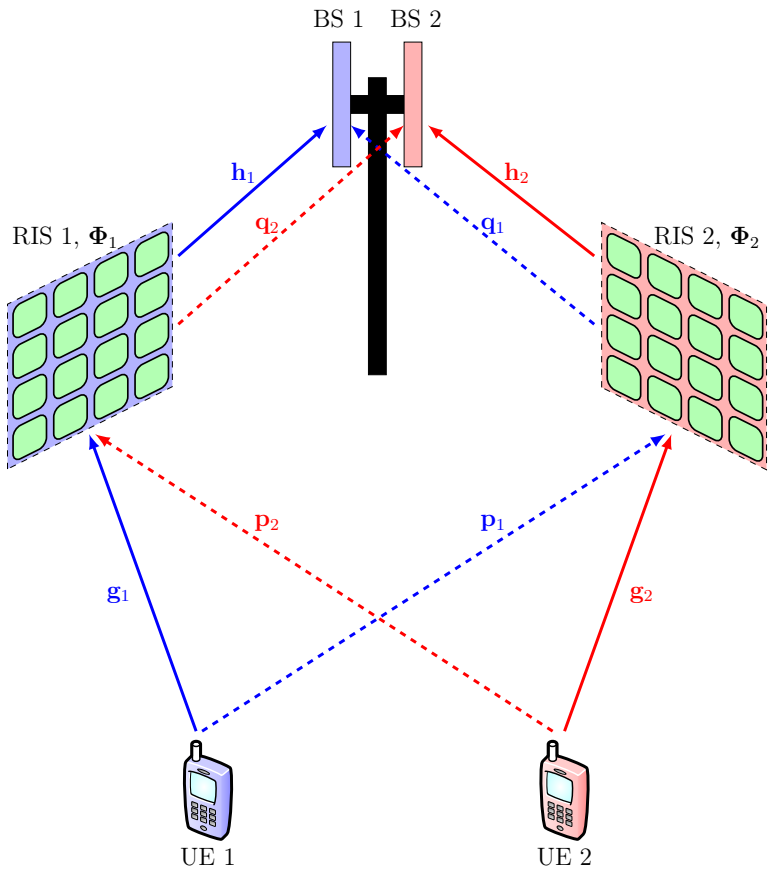

Figure 4.1: The considered setup with two UEs, two RISs, and two co-located M-antenna BSs. The blue channels correspond to frequency band 1, and the red channels correspond to frequency band 2, subscribed by UEs 1 and 2, respectively. The desired channels are denoted by solid lines, while the undesired channels (whose existences might be unknown to the BSs) are denoted by dashed lines. Each channel vector is N-dimensional because each RIS has N elements.

To obtain a more useful form of (4.2), we define $\mathbf{D}_{\tilde{\mathbf{h}}_k} = \text{diag}(\tilde{h}_{k1}, \ldots, \tilde{h}_{kN}) \in \mathbb{C}^{N\times N}$, $\mathbf{D}_{\tilde{\mathbf{q}}_k} = \text{diag}(\tilde{q}_{k1}, \ldots, \tilde{q}_{kN}) \in \mathbb{C}^{N\times N}$, $\boldsymbol{\phi}_k[l] = \begin{bmatrix} e^{-j\phi_{k,1}[l]} & \ldots & e^{-j\phi_{k,N}[l]} \end{bmatrix}^T$, and rewrite (4.2) as

$$y_{pk}[l] = \sqrt{P_p}(\boldsymbol{\phi}_k^T[l]\mathbf{D}_{\tilde{\mathbf{h}}_k}\mathbf{g}_k + \boldsymbol{\phi}_j^T[l]\mathbf{D}_{\tilde{\mathbf{q}}_k}\mathbf{p}_k)s_k[l] + w_k[l], \tag{4.3}$$

for $l = 1, \ldots, L$. Without loss of generality, we can pick $s_k[l] = 1$ for $l = 1, \ldots, L$, and vertically stack multiple pilot transmissions over time to obtain

$$\mathbf{y}_{pk} = \sqrt{P_p}(\mathbf{B}_k\mathbf{D}_{\tilde{\mathbf{h}}_k}\mathbf{g}_k + \mathbf{B}_j\mathbf{D}_{\tilde{\mathbf{q}}_k}\mathbf{p}_k) + \mathbf{w}_k \in \mathbb{C}^{L\times 1}, \tag{4.4}$$

where $\mathbf{B}_k = [\boldsymbol{\phi}_1[1], \ldots, \boldsymbol{\phi}_1[L]]^T \in \mathbb{C}^{L\times N}$ denotes the vertically stacked RIS configurations over time. It has to be noted that (4.4) is very similar to [16, Eq. 3], where the problem of inter-operator pilot contamination is introduced. In [16], however, this problem was treated in a single-antenna BS setting and was mitigated by choosing orthogonal RIS configurations at the cost of doubling the pilot transmission overhead. In this manuscript, we look into how receive beamforming at a multi-antenna BS can be used to address this problem. In the next section, we formulate the channel estimation problem and demonstrate how the use of multiple RISs by different operators causes inter-operator pilot contamination.

4.3 Problem Formulation

Based on (4.4), the BS operator k aims to estimate $\mathbf{g}_k \sim \mathcal{CN}(\mathbf{0}, \boldsymbol{\Sigma}_{\mathbf{g}_k})$ and $\mathbf{p}_k \sim \mathcal{CN}(\mathbf{0}, \boldsymbol{\Sigma}_{\mathbf{p}_k})$. To this end, the BS employs the MMSE estimator. To express the estimator in a compact form, we define the following covariance matrices:

$$\mathbf{C}_{\mathbf{gy}} = \mathbb{E}[\mathbf{g}_k\mathbf{y}_{pk}^H] \in \mathbb{C}^{N\times L}, \tag{4.5a}$$

$$\mathbf{C}_{\mathbf{py}} = \mathbb{E}[\mathbf{p}_k\mathbf{y}_{pk}^H] \in \mathbb{C}^{N\times L}, \tag{4.5b}$$

$$\mathbf{C}_{\mathbf{yy}} = \mathbb{E}[\mathbf{y}_{pk}\mathbf{y}_{pk}^H] \in \mathbb{C}^{L\times L}. \tag{4.5c}$$

As a result, the MMSE estimators for $\mathbf{g}_k$ and $\mathbf{p}_k$ become

$$\hat{\mathbf{g}}_k = \mathbf{C}_{\mathbf{gy}}\mathbf{C}_{\mathbf{yy}}^{-1}\mathbf{y}_{pk}, \tag{4.6a}$$

$$\hat{\mathbf{p}}_k = \mathbf{C}_{\mathbf{py}}\mathbf{C}_{\mathbf{yy}}^{-1}\mathbf{y}_{pk}. \tag{4.6b}$$

The resulting error covariances can be expressed as

$$\boldsymbol{\Sigma}_{\mathbf{e}_{\mathbf{g}_k}} = \mathbb{E}[(\mathbf{g}_k - \hat{\mathbf{g}}_k)(\mathbf{g}_k - \hat{\mathbf{g}}_k)^H] = \boldsymbol{\Sigma}_{\mathbf{g}_k} - \mathbf{C}_{\mathbf{gy}}\mathbf{C}_{\mathbf{yy}}^{-1}\mathbf{C}_{\mathbf{gy}}^H, \tag{4.7a}$$

$$\boldsymbol{\Sigma}_{\mathbf{e}_{\mathbf{p}_k}} = \mathbb{E}[(\mathbf{p}_k - \hat{\mathbf{p}}_k)(\mathbf{p}_k - \hat{\mathbf{p}}_k)^H] = \boldsymbol{\Sigma}_{\mathbf{p}_k} - \mathbf{C}_{\mathbf{py}}\mathbf{C}_{\mathbf{yy}}^{-1}\mathbf{C}_{\mathbf{py}}^H. \tag{4.7b}$$

Note that in the absence of pilot contamination, the covariance matrices of $\hat{\mathbf{g}}_k$ and $\hat{\mathbf{p}}_k$ approach to $\boldsymbol{\Sigma}_{\mathbf{g}_k}$ and $\boldsymbol{\Sigma}_{\mathbf{p}_k}$ as $P_p \to \infty$. Consequently, $\boldsymbol{\Sigma}_{\mathbf{e}_{\mathbf{g}_k}}$ and $\boldsymbol{\Sigma}_{\mathbf{e}_{\mathbf{p}_k}}$ approach to $\mathbf{0}$ as $P_p \to \infty$, so the estimation will be error-free.

As shown in [16], inter-operator pilot contamination arises when $\mathbf{B}_1^H\mathbf{B}_2 \neq \mathbf{0}$. In this section, we will consider the special case $\mathbf{B}_1 = \mathbf{B}_2 = \mathbf{B}$ for demonstration purposes. As a result, we can explicitly express the covariance matrices we defined in (4.5) as

$$\mathbf{C}_{\mathbf{gy}} = \sqrt{P_p}\boldsymbol{\Sigma}_{\mathbf{g}_k}\mathbf{D}_{\mathbf{h}_k}^H\mathbf{B}^H, \tag{4.8a}$$

$$\mathbf{C}_{\mathbf{py}} = \sqrt{P_p}\boldsymbol{\Sigma}_{\mathbf{p}_k}\mathbf{D}_{\mathbf{q}_k}^H\mathbf{B}^H, \tag{4.8b}$$

$$\mathbf{C}_{\mathbf{yy}} = P_p\mathbf{B}(\mathbf{D}_{\mathbf{h}_k}\boldsymbol{\Sigma}_{\mathbf{g}_k}\mathbf{D}_{\mathbf{h}_k}^H + \mathbf{D}_{\mathbf{q}_k}\boldsymbol{\Sigma}_{\mathbf{p}_k}\mathbf{D}_{\mathbf{q}_k}^H)\mathbf{B}^H + \sigma_w^2\mathbf{I}_L. \tag{4.8c}$$

The $\mathbf{B}$ and $\mathbf{B}^H$ terms can be inserted inside the inversion using their pseudoinverses. As a result, the estimator covariances in explicit form can be expressed as

$$\boldsymbol{\Sigma}_{\hat{\mathbf{g}}_k} = \boldsymbol{\Sigma}_{\mathbf{g}_k}\mathbf{D}_{\mathbf{h}_k}^H\left(\mathbf{D}_{\mathbf{h}_k}\boldsymbol{\Sigma}_{\mathbf{g}_k}\mathbf{D}_{\mathbf{h}_k}^H + \mathbf{D}_{\mathbf{q}_k}\boldsymbol{\Sigma}_{\mathbf{p}_k}\mathbf{D}_{\mathbf{q}_k}^H + \frac{\sigma_w^2}{P_p}\mathbf{I}_L\right)^{-1} \times \mathbf{D}_{\mathbf{h}_k}\boldsymbol{\Sigma}_{\mathbf{g}_k}, \tag{4.9a}$$

$$\boldsymbol{\Sigma}_{\hat{\mathbf{p}}_k} = \boldsymbol{\Sigma}_{\mathbf{p}_k}\mathbf{D}_{\mathbf{q}_k}^H\left(\mathbf{D}_{\mathbf{h}_k}\boldsymbol{\Sigma}_{\mathbf{g}_k}\mathbf{D}_{\mathbf{h}_k}^H + \mathbf{D}_{\mathbf{q}_k}\boldsymbol{\Sigma}_{\mathbf{p}_k}\mathbf{D}_{\mathbf{q}_k}^H + \frac{\sigma_w^2}{P_p}\mathbf{I}_L\right)^{-1} \times \mathbf{D}_{\mathbf{q}_k}\boldsymbol{\Sigma}_{\mathbf{p}_k}. \tag{4.9b}$$

If we take the limit as $P_p \to \infty$, we obtain

$$\boldsymbol{\Sigma}_{\hat{\mathbf{g}}_k} = \boldsymbol{\Sigma}_{\mathbf{g}_k}\mathbf{D}_{\mathbf{h}_k}^H\left(\mathbf{D}_{\mathbf{h}_k}\boldsymbol{\Sigma}_{\mathbf{g}_k}\mathbf{D}_{\mathbf{h}_k}^H + \mathbf{D}_{\mathbf{q}_k}\boldsymbol{\Sigma}_{\mathbf{p}_k}\mathbf{D}_{\mathbf{q}_k}^H\right)^{-1}\mathbf{D}_{\mathbf{h}_k}\boldsymbol{\Sigma}_{\mathbf{g}_k}, \tag{4.10a}$$

$$\boldsymbol{\Sigma}_{\hat{\mathbf{p}}_k} = \boldsymbol{\Sigma}_{\mathbf{p}_k}\mathbf{D}_{\mathbf{q}_k}^H\left(\mathbf{D}_{\mathbf{h}_k}\boldsymbol{\Sigma}_{\mathbf{g}_k}\mathbf{D}_{\mathbf{h}_k}^H + \mathbf{D}_{\mathbf{q}_k}\boldsymbol{\Sigma}_{\mathbf{p}_k}\mathbf{D}_{\mathbf{q}_k}^H\right)^{-1}\mathbf{D}_{\mathbf{q}_k}\boldsymbol{\Sigma}_{\mathbf{p}_k}. \tag{4.10b}$$

Note that in both cases, the estimator covariances fail to approach the parameter covariances due to inter-operator pilot contamination. That is, $\lim_{P_p\to\infty}\boldsymbol{\Sigma}_{\hat{\mathbf{g}}_k} \neq \boldsymbol{\Sigma}_{\mathbf{g}_k}$ and $\lim_{P_p\to\infty}\boldsymbol{\Sigma}_{\hat{\mathbf{p}}_k} \neq \boldsymbol{\Sigma}_{\mathbf{p}_k}$. To overcome this, we either have to pick $\mathbf{B}_1^H\mathbf{B}_2 = \mathbf{0}$ so that both covariances converge to their parameter covariances or we have to pick $\mathbf{v}_k$ such that one of $\tilde{\mathbf{h}}_k$ and $\tilde{\mathbf{q}}_k$ become $\mathbf{0}$. Nulling the latter is preferable as $\tilde{\mathbf{h}}_k$ goes through the operator's own RIS, whose configuration is controllable. In Sections 4.4 and 4.5, we look into the problem of designing $\mathbf{v}_k$ depending on the structures of $\mathbf{H}_k$ and $\mathbf{Q}_k$. Then, in Section 4.6, we will provide the asymptotic analysis of the estimators' behavior when pilot contamination is eliminated.

4.4 Receive Beamforming for Pure-LOS RIS-BS Channels

In this section, we look into how receive beamforming can be utilized to overcome inter-operator pilot contamination when both $\mathbf{H}_k$ and $\mathbf{Q}_k$ exhibit a pure LOS structure. We denote the angle of departure (AoD) and AoA for $\mathbf{H}_k$ and $\mathbf{Q}_k$ as $\theta_{\mathbf{H}_k}^{\text{AoD}}$, $\theta_{\mathbf{H}_k}^{\text{AoA}}$, $\theta_{\mathbf{Q}_k}^{\text{AoD}}$, and $\theta_{\mathbf{Q}_k}^{\text{AoA}}$, respectively. In addition, we denote the array

steering vectors for the k-th BSs and RISs as $\mathbf{a}_k^{\text{BS}}(\cdot) : \mathbb{R} \mapsto \mathbb{C}^{M\times 1}$ and $\mathbf{a}_k^{\text{RIS}}(\cdot) : \left[-\frac{\pi}{2}, \frac{\pi}{2}\right] \times [0, +\infty) \mapsto \mathbb{C}^{N\times 1}$. Then, we can express $\mathbf{H}_k$ and $\mathbf{Q}_k$ as

$$\mathbf{H}_k = \sqrt{\alpha_{\mathbf{H}_k}} e^{-j\beta_{\mathbf{H}_k}} \mathbf{a}_k^{\text{BS}}(\theta_{\mathbf{H}_k}^{\text{AoA}}, \lambda_k) \mathbf{a}_k^{\text{RIS}\,H}(\theta_{\mathbf{H}_k}^{\text{AoD}}, \lambda_k), \tag{4.11a}$$

$$\mathbf{Q}_k = \sqrt{\alpha_{\mathbf{Q}_k}} e^{-j\beta_{\mathbf{Q}_k}} \mathbf{a}_k^{\text{BS}}(\theta_{\mathbf{Q}_k}^{\text{AoA}}, \lambda_k) \mathbf{a}_j^{\text{RIS}\,H}(\theta_{\mathbf{Q}_k}^{\text{AoD}}, \lambda_k), \tag{4.11b}$$

where $\alpha_{\mathbf{H}_k}$ and $\alpha_{\mathbf{Q}_k}$ denote the path loss coefficients for the channels $\mathbf{H}_k$ and $\mathbf{Q}_k$, respectively, and $\beta_{\mathbf{H}_k}$ and $\beta_{\mathbf{Q}_k}$ denote the phase shifts caused by the propagation delays over the channels $\mathbf{H}_k$ and $\mathbf{Q}_k$, respectively. For simplicity, we consider ULA structures for all BSs and RISs, however, it has to be noted that the analysis in this section can be extended to any array geometry.[1] Hence, we can express the steering vectors in (4.11) as

$$\mathbf{a}_k^{\text{BS}}(\theta, \lambda) = \begin{bmatrix} 1 & e^{-j2\pi \frac{d_k}{\lambda} \sin\theta} & \dots & e^{-j2\pi \frac{d_k}{\lambda}(M-1)\sin\theta} \end{bmatrix}^T, \tag{4.12a}$$

$$\mathbf{a}_k^{\text{RIS}}(\theta, \lambda) = \begin{bmatrix} 1 & e^{-j2\pi \frac{d_k}{\lambda} \sin\theta} & \dots & e^{-j2\pi \frac{d_k}{\lambda}(N-1)\sin\theta} \end{bmatrix}^T, \tag{4.12b}$$

where d_k denotes the inter-element spacing used by the k-th operator and θ is angle measured from the broadside direction.

Aligning the Beam with the Intended Channel

Among the RIS-BS channels, note that $\mathbf{H}_k$ is the intended channel for reception. In contrast, $\mathbf{Q}_k$ is the interfering channel causing the inter-operator pilot contamination as it is the link between the intended operator's BS and the other operator's RIS. This channel is considered as interference as it involves a RIS that is not controllable by the operator of interest. To align with the intended channel, the following receive beamforming vector must be used:

$$\mathbf{v}_{k,A}^T = \frac{1}{\sqrt{M}} \mathbf{a}_k^{\text{BS}\,H} \left(\theta_{\mathbf{H}_k}^{\text{AoA}}, \lambda_k\right). \tag{4.13}$$

As a result, the following equivalent Multiple-input single-output (MISO) channels arise:

$$\tilde{\mathbf{h}}_k = \sqrt{M\alpha_{\mathbf{H}_k}} e^{-j\beta_{\mathbf{H}_k}} \mathbf{a}_k^{\text{RIS}*} \left(\theta_{\mathbf{H}_k}^{\text{AoD}}, \lambda_k\right), \tag{4.14a}$$

$$\tilde{\mathbf{q}}_k = \sqrt{\frac{\alpha_{\mathbf{Q}_k}}{M}} e^{-j\beta_{\mathbf{Q}_k}} \underbrace{\mathbf{a}_k^{\text{BS}\,H}(\theta_{\mathbf{H}_k}^{\text{AoA}}, \lambda_k) \mathbf{a}_k^{\text{BS}} \left(\theta_{\mathbf{Q}_k}^{\text{AoA}}, \lambda_k\right)}_{\triangleq \eta_k} \times \mathbf{a}_j^{\text{RIS}*}(\theta_{\mathbf{Q}_k}^{\text{AoD}}, \lambda_k). \tag{4.14b}$$

[1] This can be done by considering the relevant array steering vector and applying the formulae accordingly.

This beamforming vector aligns the BS's reception with $\mathbf{H}_k$. However, some interference will remain from $\mathbf{Q}_k$ as there is no null forming in that direction; that is, η_k will be non-zero. In the next subsection, we propose a method to remove this residual interference.

Aligning with the Intended Channel While Nulling the Interfering Channel

To combat the problem of residual interference, we can choose the receive combining to place a null towards $\mathbf{Q}_k$ by using orthogonal projection. We can first beamform towards $\mathbf{H}_k$, then subtract the correlated component to $\mathbf{Q}_k$. We can achieve this as follows:

$$\tilde{\mathbf{v}}_{k,B}^T = \mathbf{a}_k^{\mathrm{BS}\,H}(\theta_{\mathbf{H}_k}^{\mathrm{AoA}}, \lambda_k) - \eta_k \frac{\mathbf{a}_k^{\mathrm{BS}\,H}(\theta_{\mathbf{Q}_k}^{\mathrm{AoA}}, \lambda_k)}{\|\mathbf{a}_k^{\mathrm{BS}}(\theta_{\mathbf{Q}_k}^{\mathrm{AoA}}, \lambda_k)\|^2}. \tag{4.15}$$

Note that the resulting beamforming vector in (4.15) will have a different l_2 norm than 1. To normalize it, we need to multiply it with $\frac{1}{\|\tilde{\mathbf{v}}_{k,B}^T\|}$, which results in

$$\mathbf{v}_{k,B}^T = \frac{1}{\|\tilde{\mathbf{v}}_{k,B}^T\|}\tilde{\mathbf{v}}_{k,B}^T, \tag{4.16}$$

where $\|\tilde{\mathbf{v}}_{k,B}\|^2 = M - \frac{|\eta_k|^2}{M}$. To express (4.14) for $\mathbf{v}_{k,B}^T$, we need to compute $\mathbf{v}_{k,B}^T\mathbf{a}_k^{\mathrm{BS}}(\theta_{\mathbf{H}_k}^{\mathrm{AoA}})$ and $\mathbf{v}_{k,B}^T\mathbf{a}_k^{\mathrm{BS}}(\theta_{\mathbf{Q}_k}^{\mathrm{AoA}})$. These can be expressed as follows:

$$\mathbf{v}_{k,B}^T\mathbf{a}_k^{\mathrm{BS}}(\theta_{\mathbf{H}_k}^{\mathrm{AoA}}) = \sqrt{M - \frac{|\eta_k|^2}{M}}, \tag{4.17a}$$

$$\mathbf{v}_{k,B}^T\mathbf{a}_k^{\mathrm{BS}}(\theta_{\mathbf{Q}_k}^{\mathrm{AoA}}) = \sqrt{\frac{1}{M - \frac{|\eta_k|^2}{M}}}\,(\eta_k - \eta_k) = 0. \tag{4.17b}$$

Note that $\mathbf{v}_{k,B}^T$ completely eliminates the interference coming from $\mathbf{Q}_k$ and hence the inter-operator pilot contamination. On the other hand, the gain from $\mathbf{H}_k$ is multiplied by a factor of $\sqrt{1 - \frac{|\eta_k|^2}{M^2}} \in [0, 1]$. This factor takes the value 0 when $|\eta_k| = M$ and 1 when $\eta_k = 0$. This implies that when the receiver steering vectors of $\mathbf{H}_k$ and $\mathbf{Q}_k$ are orthogonal, there is no loss in the gain from $\mathbf{H}_k$, and $\mathbf{v}_{k,A}$ and $\mathbf{v}_{k,B}$ are equivalent. On the other hand, if $|\eta_k| = M$ and hence the receive steering vectors are fully correlated, then $\mathbf{v}_{k,B}$ nullforms towards both channels and $\mathbf{v}_{k,A}$ beamforms towards both channels. The former case is the best-case scenario, while the latter is the worst-case scenario, i.e., when inter-operator pilot contamination cannot be eliminated. A summary of the resulting correlations can be found in Table 4.1. As a result, we can express the effective

Table 4.1: Summary of correlations between AoA steering vectors and the two beamforming vectors where $\mathbf{v}_{k,A}$ is the beamforming vector maximizing the gain from the intended channel, and $\mathbf{v}_{k,B}$ is the beamforming vector resulting from placing nulls into the first beamformer.

	$\mathbf{a}_k^{\mathrm{BS}}(\theta_{\mathbf{H}_k}^{\mathrm{AoA}})$	$\mathbf{a}_k^{\mathrm{BS}}(\theta_{\mathbf{Q}_k}^{\mathrm{AoA}})$
$\mathbf{v}_{k,A}^T$	$\sqrt{M}$	η_k
$\mathbf{v}_{k,B}^T$	$\sqrt{M - \frac{\lvert\eta_k\rvert^2}{M}}$	0

MISO channels as follows:

$$\tilde{\mathbf{h}}_k = \sqrt{M - \frac{|\eta_k|^2}{M}}\sqrt{\alpha_{\mathbf{H}_k}} e^{-j\beta_{\mathbf{H}_k}} \mathbf{a}_k^{\mathrm{RIS}}(\theta_{\mathbf{H}_k}^{\mathrm{AoD}}, \lambda_k), \tag{4.18a}$$

$$\tilde{\mathbf{q}}_k = \mathbf{0}. \tag{4.18b}$$

Note that for pure-LOS RIS-BS channels, we can explicitly use the **DoA!** (**DoA!**) information to construct our receive beamforming vector. However, it is not always possible to keep track of all reflections in the environment spatially in the presence of multiple dominant paths. To this end, a more generic approach has to be taken. To this end, the structural assumptions on the channels have to be replaced with a more generic approach and SVD analysis has to be formed. We demonstrate this in the next section.

4.5 Receive Beamforming for Unstructured RIS-BS Channels

In this section, we look into how receive beamforming can be utilized to overcome inter-operator pilot contamination when neither $\mathbf{H}_k$ nor $\mathbf{Q}_k$ exhibits any particular structure. Unstructured MIMO channels can be expressed as a weighted sum of rank-1 matrices, which can be done by SVD. The singular values are the weights of the rank-1 matrices, and the left and right singular vectors correspond to the vectors forming the outer product. That is, for the SVD

$$\mathbf{A} = \mathbf{U}\mathbf{\Sigma}\mathbf{V}^H \in \mathbb{C}^{M\times N}, \tag{4.19}$$

we have that $\mathbf{A} = \sum_{k=1}^{N} \sigma_k \mathbf{u}_k \mathbf{v}_k^H$. We already know how to treat rank-1 channels for beamforming purposes from Section 4.4. To apply the same principles, we need to identify the dominant rank-1 channel within $\mathbf{H}_k$, and the non-zero rank-1 components of $\mathbf{Q}_k$, for which we need to take their SVDs. Suppose that $\mathbf{H}_k$ and $\mathbf{Q}_k$ have the following SVDs:

$$\mathbf{H}_k = \mathbf{\Gamma}_k \mathbf{\Sigma}_k \mathbf{\Upsilon}_k^H, \tag{4.20a}$$

$$\mathbf{Q}_k = \mathbf{\Delta}_k \mathbf{\Xi}_k \mathbf{\Omega}_k^H. \tag{4.20b}$$

We denote the singular vectors as $\mathbf{\Gamma}_k = \begin{bmatrix}\boldsymbol{\gamma}_{k,1} & \dots & \boldsymbol{\gamma}_{k,M}\end{bmatrix} \in \mathbb{C}^{M\times M}$, $\mathbf{\Delta}_k = \begin{bmatrix}\boldsymbol{\delta}_{k,1} & \dots & \boldsymbol{\delta}_{k,M}\end{bmatrix} \in \mathbb{C}^{M\times M}$, $\mathbf{\Upsilon}_k = \begin{bmatrix}\boldsymbol{\upsilon}_{k,1} & \dots & \boldsymbol{\upsilon}_{k,N}\end{bmatrix} \in \mathbb{C}^{N\times N}$, and $\mathbf{\Omega}_k = \begin{bmatrix}\boldsymbol{\omega}_{k,1} & \dots & \boldsymbol{\omega}_{k,N}\end{bmatrix} \in \mathbb{C}^{N\times N}$. Denote the singular values of $\mathbf{H}$ as $\sigma_1, \dots, \sigma_N$ and those of $\mathbf{Q}$ as $\xi_1, \dots, \xi_N$.

Aligning the Beam with the Intended Channel

To align our reception with $\mathbf{H}_k$ using a vector $\mathbf{v}_k$, we need to align $\mathbf{v}_k$ with the left singular vector of $\mathbf{H}_k$ corresponding to the largest singular value. Let us denote this singular vector as $\boldsymbol{\gamma}_{k,C}$. Then, we set $\mathbf{v}_k$ as

$$\mathbf{v}_{k,C}^T = \boldsymbol{\gamma}_{k,C}^H. \tag{4.21}$$

Based on this selection of the beamforming vector, the effective MISO channels become

$$\tilde{\mathbf{h}}_k^T = \sigma_{k,C}\boldsymbol{\upsilon}_{k,C}^H, \tag{4.22a}$$

$$\tilde{\mathbf{q}}_k^T = \boldsymbol{\gamma}_{k,C}^H\mathbf{Q}_k, \tag{4.22b}$$

where $\sigma_{k,C}$ is the largest singular value of $\mathbf{H}_k$ and $\boldsymbol{\upsilon}_{k,C}$ is the corresponding right singular vector.

Beamforming Towards the Intended Channel While Null Forming Towards the Interfering Channel

While beamforming according to the largest singular value of the intended channel $\mathbf{H}_k$ yields the maximum gain possible, it has to be noted that this scheme does not remove the interference coming from $\mathbf{Q}_k$, which causes the inter-operator pilot contamination. However, this interference has to be removed to obtain reliable channel estimates. To this end, we consider removing the components correlated to the singular vectors of $\mathbf{Q}_k$ corresponding to non-zero singular values. Suppose that $\mathbf{Q}_k$ has $R \leq N$ non-zero singular values. Then, we need to orthogonalize $\mathbf{v}_k$ to $\boldsymbol{\delta}_{k,1}, \dots, \boldsymbol{\delta}_{k,R}$. To this end, we can subtract the orthogonal projections of the singular vectors of $\mathbf{Q}_k$ on $\boldsymbol{\gamma}_{k,C}$ recursively. That is,

$$\begin{aligned}
\tilde{\mathbf{v}}_{k,D}^{(0)^T} &= \boldsymbol{\gamma}_{k,C}^H, \\
\tilde{\mathbf{v}}_{k,D}^{(1)^T} &= \tilde{\mathbf{v}}_{k,D}^{(0)^T} - \frac{\boldsymbol{\delta}_{k,1}^H\tilde{\mathbf{v}}_{k,D}^{(0)}}{\|\boldsymbol{\delta}_{k,1}\|^2}\boldsymbol{\delta}_{k,1}^H, \\
\tilde{\mathbf{v}}_{k,D}^{(2)^T} &= \tilde{\mathbf{v}}_{k,D}^{(1)^T} - \frac{\boldsymbol{\delta}_{k,2}^H\tilde{\mathbf{v}}_{k,D}^{(1)}}{\|\boldsymbol{\delta}_{k,2}\|^2}\boldsymbol{\delta}_{k,2}^H, \\
&\vdots \\
\tilde{\mathbf{v}}_{k,D}^{(R)^T} &= \tilde{\mathbf{v}}_{k,D}^{(R-1)^T} - \frac{\boldsymbol{\delta}_{k,R}^H\tilde{\mathbf{v}}_{k,D}^{(R-1)}}{\|\boldsymbol{\delta}_{k,R}\|^2}\boldsymbol{\delta}_{k,R}^H.
\end{aligned} \tag{4.23}$$

Next, we normalize (4.23) to obtain the beamforming vector towards $\mathbf{H}_k$ that also nullforms towards $\mathbf{Q}_k$ as

$$\mathbf{v}_{k,D} = \frac{1}{\|\tilde{\mathbf{v}}_{k,D}\|}\tilde{\mathbf{v}}_{k,D}^{(R)}. \tag{4.24}$$

4.6 Channel Estimation based on Correlated Rayleigh Fading Priors

Since $\mathbf{H}_k$ and $\mathbf{Q}_k$ are already known at the BS, the BS aims to estimate $\mathbf{g}_k$ and $\mathbf{p}_k$ for $k = 1, 2$. Since the beamforming vectors $\mathbf{v}_k$ are also known by the BSs, the effective RIS-BS MISO channels $\tilde{\mathbf{h}}_k$ and $\tilde{\mathbf{q}}_k$ are also known. Sections 4.4 and 4.5 focus on shaping the channels $\tilde{\mathbf{h}}_k$ and $\tilde{\mathbf{q}}_k$ using receive beamforming. Specifically, when null forming towards $\mathbf{Q}_k$ is applied, the effect of the unintended path through the other operator's RIS is essentially removed. In [16, Sec. V], a detailed analysis of the channel estimation covariances for a model equivalent to (4.4) is provided. To investigate the impact of RIS configurations on inter-operator pilot contamination, in this paper, we consider three scenarios:

1. The user transmits $L = 2N$ pilots. The operators configure their RISs such that $\mathbf{B}_1^H\mathbf{B}_2 = \mathbf{0}$, and both operators beamform towards $\mathbf{H}_k$'s without null forming towards $\mathbf{Q}_k$'s. For conciseness, we will call this *Scheme 1*.

2. The user transmits $L = N$ pilots. The operators configure their RISs such that $\mathbf{B}_1 = \mathbf{B}_2$, and both operators beamform towards $\mathbf{H}_k$'s and nullform towards $\mathbf{Q}_k$'s. For conciseness, we will call this *Scheme 2*.

3. In the baseline scheme, the user transmits $L = N$ pilots. The operators configure their RISs such that $\mathbf{B}_1 = \mathbf{B}_2$, and both operators beamform towards $\mathbf{H}_k$'s without null forming towards $\mathbf{Q}_k$'s. For conciseness, we will call this *the baseline scheme*.

For each scenario, we provide the resulting channel estimation error covariances to evaluate the data communication performance under imperfect CSI later on.

Scheme 1

In this scheme, the receive beamforming captures the maximum energy from the intended channel, but it does not suppress interference. However, the interference is canceled by separating RIS configuration sequences, which is enabled by doubling the number of transmitted pilots and picking $\mathbf{B}_1^H\mathbf{B}_2 = \mathbf{0}$. Consequently, using this scheme, the following received pilot signal models arise:

$$\mathbf{y}_{p1} = \sqrt{P_p}(\mathbf{B}_1\mathbf{D}_{\tilde{\mathbf{h}}_1}\mathbf{g}_1 + \mathbf{B}_2\mathbf{D}_{\tilde{\mathbf{q}}_1}\mathbf{p}_1) + \mathbf{w}_1 \in \mathbb{C}^{L\times 1}, \tag{4.25a}$$

$$\mathbf{y}_{p2} = \sqrt{P_p}(\mathbf{B}_2\mathbf{D}_{\tilde{\mathbf{h}}_2}\mathbf{g}_2 + \mathbf{B}_1\mathbf{D}_{\tilde{\mathbf{q}}_2}\mathbf{p}_2) + \mathbf{w}_2 \in \mathbb{C}^{L\times 1}, \tag{4.25b}$$

for $L \geq 2N$.

Scheme 2

In this scheme, the receive beamforming captures the maximum energy from the intended channel while suppressing the interference from $\mathbf{Q}_k$. This interference suppression by null forming causes the beamformer to capture less energy from $\mathbf{H}_k$. On the other hand, it is no longer necessary to orthogonalize the sequences of RIS configurations – and hence to double the number of transmitted pilots – since inter-operator pilot contamination is removed by receive beamforming. Therefore, this scheme configures the RISs without orthogonalizing them to each other, that is, $\mathbf{B}_1 = \mathbf{B}_2$. This approach uses half as many pilot transmissions as Scheme 1. Consequently, the following received pilot signal models arise:

$$\mathbf{y}_{p1} = \sqrt{P_p}\mathbf{B}_1\mathbf{D}_{\tilde{\mathbf{h}}_1}\mathbf{g}_1 + \mathbf{w}_1 \in \mathbb{C}^{L\times 1}, \tag{4.26a}$$

$$\mathbf{y}_{p2} = \sqrt{P_p}\mathbf{B}_2\mathbf{D}_{\tilde{\mathbf{h}}_2}\mathbf{g}_2 + \mathbf{w}_2 \in \mathbb{C}^{L\times 1}, \tag{4.26b}$$

for $L \geq N$.

Baseline Scheme

In this scheme, the receive beamforming is done as in Scheme 1. Unlike Scheme 1, however, the interference is not canceled by orthogonalizing the RISs, and $\mathbf{B}_1 = \mathbf{B}_2$ is adopted as in Scheme 2, but without null forming. Consequently, the following received pilot signal models arise:

$$\mathbf{y}_{p1} = \sqrt{P_p}(\mathbf{B}_1\mathbf{D}_{\tilde{\mathbf{h}}_1}\mathbf{g}_1 + \mathbf{B}_2\mathbf{D}_{\tilde{\mathbf{q}}_1}\mathbf{p}_1) + \mathbf{w}_1 \in \mathbb{C}^{L\times 1}, \tag{4.27a}$$

$$\mathbf{y}_{p2} = \sqrt{P_p}(\mathbf{B}_2\mathbf{D}_{\tilde{\mathbf{h}}_2}\mathbf{g}_2 + \mathbf{B}_1\mathbf{D}_{\tilde{\mathbf{q}}_2}\mathbf{p}_2) + \mathbf{w}_2 \in \mathbb{C}^{L\times 1}, \tag{4.27b}$$

for $L \geq N$.

Impact of choice of scheme on MMSE Channel Estimation Performance

In Section 4.3, we had demonstrated the channel estimation MSEs. The discussion so far impacts the MSE by the following means:

- The choice of scheme affects $\mathbf{C}_{\mathbf{yy}}$ as the path over the other operator's RIS is nulled when nullforming is applied.
- The gains of $\tilde{\mathbf{h}}_k$ and $\tilde{\mathbf{q}}_k$ are affected by how beamforming is carried out.

Consequently, the result of (4.7) changes depending on which scheme is adopted. Next, we consider the asymptotic behavior of the estimators' covariances for Scheme 1 and the baseline scheme to demonstrate the impact of inter-operator pilot contamination.

Asymptotic Behavior of Estimator Covariances

For all schemes, the estimator covariances can be expressed as

$$\mathbf{\Sigma}_{\hat{\mathbf{g}}_k} = \mathbf{C}_{\mathbf{gy}}\mathbf{C}_{\mathbf{yy}}^{-1}\mathbf{C}_{\mathbf{gy}}^{H}, \tag{4.28a}$$

$$\mathbf{\Sigma}_{\hat{\mathbf{p}}_k} = \mathbf{C}_{\mathbf{py}}\mathbf{C}_{\mathbf{yy}}^{-1}\mathbf{C}_{\mathbf{py}}^{H}. \tag{4.28b}$$

Note that

$$\lim_{P_p\to\infty}\frac{1}{P_p}\mathbf{C}_{\mathbf{yy}} = \mathbf{B}_k\mathbf{D}_{\mathbf{h}_k}\mathbf{\Sigma}_{\mathbf{g}_k}\mathbf{D}_{\mathbf{h}_k}^{H}\mathbf{B}_k^{H} + \mathbf{B}_j\mathbf{D}_{\mathbf{q}_k}\mathbf{\Sigma}_{\mathbf{p}_k}\mathbf{D}_{\mathbf{q}_k}^{H}\mathbf{B}_j^{H}, \tag{4.29}$$

which then translates to

$$\begin{aligned}\lim_{P_p\to\infty}\mathbf{\Sigma}_{\hat{\mathbf{g}}_k} &= \mathbf{\Sigma}_{\mathbf{g}_k}\mathbf{D}_{\mathbf{h}_k}^{H}\mathbf{B}_k^{H}\\ &\times\left(\mathbf{B}_k\mathbf{D}_{\mathbf{h}_k}\mathbf{\Sigma}_{\mathbf{g}_k}\mathbf{D}_{\mathbf{h}_k}^{H}\mathbf{B}_k^{H} + \mathbf{B}_j\mathbf{D}_{\mathbf{q}_k}\mathbf{\Sigma}_{\mathbf{p}_k}\mathbf{D}_{\mathbf{q}_k}^{H}\mathbf{B}_j\right)^{-1}\mathbf{B}_k\mathbf{D}_{\mathbf{h}_k}\mathbf{\Sigma}_{\mathbf{g}_k},\end{aligned} \tag{4.30a}$$

$$\begin{aligned}\lim_{P_p\to\infty}\mathbf{\Sigma}_{\hat{\mathbf{p}}_k} &= \mathbf{\Sigma}_{\mathbf{p}_k}\mathbf{D}_{\mathbf{q}_k}^{H}\mathbf{B}_j^{H}\\ &\times\left(\mathbf{B}_k\mathbf{D}_{\mathbf{h}_k}\mathbf{\Sigma}_{\mathbf{g}_k}\mathbf{D}_{\mathbf{h}_k}^{H}\mathbf{B}_k^{H} + \mathbf{B}_j\mathbf{D}_{\mathbf{q}_k}\mathbf{\Sigma}_{\mathbf{p}_k}\mathbf{D}_{\mathbf{q}_k}^{H}\mathbf{B}_j\right)^{-1}\mathbf{B}_j\mathbf{D}_{\mathbf{q}_k}\mathbf{\Sigma}_{\mathbf{p}_k}.\end{aligned} \tag{4.30b}$$

For Scheme 1, if we insert $\mathbf{B}_k$ and $\mathbf{B}_k^H$ inside the matrix inversion using their pseudoinverses, we get

$$\lim_{P_p\to\infty}(\mathbf{B}_k^{H}\mathbf{B}_k)^{-1}\mathbf{B}_k^{H}\mathbf{C}_{\mathbf{yy}}\mathbf{B}_k(\mathbf{B}_k^{H}\mathbf{B}_k)^{-1} = \mathbf{D}_{\mathbf{h}_k}\mathbf{\Sigma}_{\mathbf{g}_k}\mathbf{D}_{\mathbf{h}_k}^{H}, \tag{4.31a}$$

$$\lim_{P_p\to\infty}(\mathbf{B}_j^{H}\mathbf{B}_j)^{-1}\mathbf{B}_j^{H}\mathbf{C}_{\mathbf{yy}}\mathbf{B}_k(\mathbf{B}_j^{H}\mathbf{B}_j)^{-1} = \mathbf{D}_{\mathbf{q}_k}\mathbf{\Sigma}_{\mathbf{p}_k}\mathbf{D}_{\mathbf{q}_k}^{H}, \tag{4.31b}$$

since $\mathbf{B}_1^H\mathbf{B}_2 = \mathbf{0}$. Observe that this yields

$$\lim_{P_p\to\infty}\mathbf{\Sigma}_{\hat{\mathbf{g}}_k} = \mathbf{\Sigma}_{\mathbf{g}_k}\mathbf{D}_{\mathbf{h}_k}^{H}(\mathbf{D}_{\mathbf{h}_k}\mathbf{\Sigma}_{\mathbf{g}_k}\mathbf{D}_{\mathbf{h}_k}^{H})^{-1}\mathbf{D}_{\mathbf{h}_k}\mathbf{\Sigma}_{\mathbf{g}_k} = \mathbf{\Sigma}_{\mathbf{g}_k}, \tag{4.32a}$$

$$\lim_{P_p\to\infty}\mathbf{\Sigma}_{\hat{\mathbf{p}}_k} = \mathbf{\Sigma}_{\mathbf{p}_k}\mathbf{D}_{\mathbf{q}_k}^{H}(\mathbf{D}_{\mathbf{q}_k}\mathbf{\Sigma}_{\mathbf{p}_k}\mathbf{D}_{\mathbf{q}_k}^{H})^{-1}\mathbf{D}_{\mathbf{q}_k}\mathbf{\Sigma}_{\mathbf{p}_k} = \mathbf{\Sigma}_{\mathbf{p}_k}. \tag{4.32b}$$

In contrast, since $\mathbf{B}_1 = \mathbf{B}_2$ for the baseline scheme, we obtain the results shown in in Section 4.3. The resulting asymptotic covariances of the estimators are summarized in (4.33).

$$\lim_{P_p \to \infty} \boldsymbol{\Sigma}_{\hat{\mathbf{g}}_k} = \begin{cases} \boldsymbol{\Sigma}_{\mathbf{g}_k} & \text{for Scheme 1,} \\ \boldsymbol{\Sigma}_{\mathbf{g}_k} \mathbf{D}_{\mathbf{h}_k}^H \Big(\mathbf{D}_{\mathbf{h}_k} \boldsymbol{\Sigma}_{\mathbf{g}_k} \mathbf{D}_{\mathbf{h}_k}^H + \underbrace{\mathbf{D}_{\mathbf{q}_k} \boldsymbol{\Sigma}_{\mathbf{p}_k} \mathbf{D}_{\mathbf{q}_k}^H}_{\text{pilot contam.}} \Big)^{-1} \mathbf{D}_{\mathbf{h}_k} \boldsymbol{\Sigma}_{\mathbf{g}_k} & \text{for the baseline,} \end{cases} \tag{4.33a}$$

$$\lim_{P_p \to \infty} \boldsymbol{\Sigma}_{\hat{\mathbf{p}}_k} = \begin{cases} \boldsymbol{\Sigma}_{\mathbf{p}_k} & \text{for Scheme 1,} \\ \boldsymbol{\Sigma}_{\mathbf{p}_k} \mathbf{D}_{\mathbf{q}_k}^H \Big(\underbrace{\mathbf{D}_{\mathbf{h}_k} \boldsymbol{\Sigma}_{\mathbf{g}_k} \mathbf{D}_{\mathbf{h}_k}^H}_{\text{pilot contam.}} + \mathbf{D}_{\mathbf{q}_k} \boldsymbol{\Sigma}_{\mathbf{p}_k} \mathbf{D}_{\mathbf{q}_k}^H \Big)^{-1} \mathbf{D}_{\mathbf{q}_k} \boldsymbol{\Sigma}_{\mathbf{p}_k} & \text{for the baseline.} \end{cases} \tag{4.33b}$$

In Section 4.7, the statistics of the effective channel conditioned on the channel estimates will be important for determining the lower bound for channel capacity.

4.7 Capacity Lower Bound for Reliable Communication Under Imperfect CSI

While the previous section demonstrates the impact of removing pilot contamination on the channel estimation performance, examining the benefits of this for data transmission performance is also important. To this end, we compute a lower bound on the ergodic capacity based on the imperfect CSI obtained in the previous section via uplink pilot transmission in this section. In particular, we consider the channel capacity for the two schemes we have specified in Section 4.6. We first recall important results on the relation between channel capacity and CSI for SISO channels, which will be useful in the sequel.

Capacity Lower Bound of a SISO Channel with Channel Side Information

Consider a generic SISO system with the following received signal model:

$$y = hx + w. \tag{4.34}$$

Suppose that the receiver has partial information on h, denoted by Ω. Then the capacity lower bound is [13, Eq. 2.46]

$$C \geq \mathbb{E}_{\Omega} \left[\log_2 \left(1 + \frac{|\mathbb{E}[h|\Omega]|^2}{\mathrm{Var}(h|\Omega) + \mathrm{Var}(w|\Omega)} \right) \right]. \tag{4.35}$$

This bound is valid under three conditions: $\mathbb{E}[w|\Omega] = 0$, $\mathbb{E}[xw^*|\Omega] = \mathbb{E}[x|\Omega]\mathbb{E}[w^*|\Omega]$, and $\mathbb{E}[hxw^*|\Omega] = \mathbb{E}[hx|\Omega]\mathbb{E}[w^*|\Omega]$ [13, Section 2.3.5].

Capacity Lower Bound

To maximize gain over the intended channels, the operators configure the RISs based on their channel estimates. That is,

$$\begin{aligned}\hat{\phi}_{kn} &= \arg(h_{kn}) + \arg(\hat{g}_{kn}),\\ \hat{\mathbf{\Phi}}_k &= \operatorname{diag}\left(e^{-j\hat{\phi}_{k1}}, \ldots, e^{-j\hat{\phi}_{kN}}\right),\end{aligned} \tag{4.36}$$

where $\arg(\cdot)$ denotes the angle (or argument) of the complex number.

Scheme 1

When the scheme described in Section 4.6 is used during channel estimation and the beamforming vector is left unchanged throughout data transmission, the following received data signal model arises:

$$y_1 = \sqrt{P_d}(\tilde{\mathbf{h}}_1^T \mathbf{\Phi}_1 \mathbf{g}_1 + \tilde{\mathbf{q}}_1^T \mathbf{\Phi}_2 \mathbf{p}_1)x_1 + w_1, \tag{4.37a}$$

$$y_2 = \sqrt{P_d}(\tilde{\mathbf{h}}_2^T \mathbf{\Phi}_2 \mathbf{g}_2 + \tilde{\mathbf{q}}_2^T \mathbf{\Phi}_1 \mathbf{p}_2)x_2 + w_2. \tag{4.37b}$$

For this scheme, we have to consider both paths and the estimates of both $\mathbf{g}_k$ and $\mathbf{p}_k$. Therefore, we should define the overall SISO channel as

$$v_k \triangleq \sqrt{P_d}(\tilde{\mathbf{h}}_k^T \hat{\mathbf{\Phi}}_k \mathbf{g}_k + \tilde{\mathbf{q}}_k^T \hat{\mathbf{\Phi}}_j \mathbf{p}_k). \tag{4.38}$$

To derive the capacity bound, we need to identify the available channel side information Ω. For this scheme, we estimate both $\mathbf{g}_k$ and $\mathbf{p}_k$, therefore, we can deduce that Ω is $\hat{\mathbf{g}}_k$ and $\hat{\mathbf{p}}_k$. Consequently, the expressions we have to evaluate to obtain the capacity lower bound are $\mathbb{E}[v_k|\hat{\mathbf{g}}_k, \hat{\mathbf{p}}_k]$ and $\mathrm{Var}(v_k|\hat{\mathbf{g}}_k, \hat{\mathbf{p}}_k)$. First, consider the conditional mean of the overall SISO channel:

$$\begin{aligned}&\mathbb{E}[v_k|\hat{\mathbf{g}}_k, \hat{\mathbf{p}}_k] =\\ &\quad\sqrt{P_d}(\tilde{\mathbf{h}}_k^T \hat{\mathbf{\Phi}}_k \mathbb{E}[\mathbf{g}_k|\hat{\mathbf{g}}_k, \hat{\mathbf{p}}_k] + \tilde{\mathbf{q}}_k^T \hat{\mathbf{\Phi}}_j \mathbb{E}[\mathbf{p}_k|\hat{\mathbf{g}}_k, \hat{\mathbf{p}}_k]).\end{aligned} \tag{4.39}$$

Note that since $\mathbf{B}_1^H \mathbf{B}_2 = \mathbf{0}$, the estimation of $\mathbf{g}_k$ and $\mathbf{p}_k$ were separated in the channel estimation step. Therefore, $\mathbf{g}_k$ and $\hat{\mathbf{p}}_k$ are independent. As a result, we can simplify (4.39) as

$$\mathbb{E}[v_k|\hat{\mathbf{g}}_k, \hat{\mathbf{p}}_k] = \sqrt{P_d}(\tilde{\mathbf{h}}_k^T \hat{\mathbf{\Phi}}_k \mathbb{E}[\mathbf{g}_k|\hat{\mathbf{g}}_k] + \tilde{\mathbf{q}}_k^T \hat{\mathbf{\Phi}}_j \mathbb{E}[\mathbf{p}_k|\hat{\mathbf{p}}_k]). \tag{4.40}$$

What remains is to evaluate $\mathbb{E}[\mathbf{g}_k|\hat{\mathbf{g}}_k]$ and $\mathbb{E}[\mathbf{p}_k|\hat{\mathbf{p}}_k]$. To this end, we recall that the MMSE estimator is the conditional mean estimator, that is, the expectations

of interest are the MMSE estimates of $\mathbf{g}_k$ based on $\hat{\mathbf{g}}_k$ and $\mathbf{p}_k$ based on $\hat{\mathbf{p}}_k$, respectively. Since the $\mathbf{g}_k$–$\hat{\mathbf{g}}_k$ and $\mathbf{p}_k$–$\hat{\mathbf{p}}_k$ pairs are jointly Gaussian, the MMSE estimates are equivalent to the LMMSE estimates in both cases. As a result, we can evaluate these expectations as follows:

$$\begin{aligned}\mathbb{E}[\mathbf{g}_k|\hat{\mathbf{g}}_k] &= \hat{\mathbf{g}}_k,\\ \mathbb{E}[\mathbf{p}_k|\hat{\mathbf{p}}_k] &= \hat{\mathbf{p}}_k,\end{aligned} \tag{4.41}$$

since the channel estimation error is independent of the channel itself and is complex Gaussian. Next, we shall consider $\mathrm{Var}(v_k|\hat{\mathbf{g}}_k, \hat{\mathbf{p}}_k)$. We can express this as

$$\begin{aligned}\mathrm{Var}(v_k|\hat{\mathbf{g}}_k, \hat{\mathbf{p}}_k) &= \mathrm{Var}\left(\sqrt{P_d}(\tilde{\mathbf{h}}_k^T\hat{\mathbf{\Phi}}_k\mathbf{g}_k + \tilde{\mathbf{q}}_k^T\hat{\mathbf{\Phi}}_j\mathbf{p}_k)|\hat{\mathbf{g}}_k, \hat{\mathbf{p}}_k\right),\\ &= P_d\tilde{\mathbf{h}}_k^T\hat{\mathbf{\Phi}}_k\,\mathrm{Var}(\mathbf{g}_k|\hat{\mathbf{g}}_k, \hat{\mathbf{p}}_k)\hat{\mathbf{\Phi}}_k^H\tilde{\mathbf{h}}_k^*\\ &+ P_d\tilde{\mathbf{q}}_k^T\hat{\mathbf{\Phi}}_j\,\mathrm{Var}(\mathbf{p}_k|\hat{\mathbf{g}}_k, \hat{\mathbf{p}}_k)\hat{\mathbf{\Phi}}_j^H\tilde{\mathbf{q}}_k^*\\ &+ 2P_d\,\mathrm{Re}\Big\{\tilde{\mathbf{h}}_k\hat{\mathbf{\Phi}}_k\underbrace{\mathrm{Cov}(\mathbf{g}_k, \mathbf{p}_k|\hat{\mathbf{g}}_k, \hat{\mathbf{p}}_k)}_{=0}\hat{\mathbf{\Phi}}_j^H\tilde{\mathbf{q}}_k^*\Big\}.\end{aligned} \tag{4.42}$$

Note that $\mathbf{g}_k$ is independent from $\hat{\mathbf{p}}_k$, hence we can simplify (4.42) as

$$\begin{aligned}\mathrm{Var}(v_k|\hat{\mathbf{g}}_k, \hat{\mathbf{p}}_k) &= P_d\tilde{\mathbf{h}}_k^T\hat{\mathbf{\Phi}}_k\,\mathrm{Var}(\mathbf{g}_k|\hat{\mathbf{g}}_k)\hat{\mathbf{\Phi}}_k^H\tilde{\mathbf{h}}_k^*\\ &+ P_d\tilde{\mathbf{q}}_k^T\hat{\mathbf{\Phi}}_j\,\mathrm{Var}(\mathbf{p}_k|\hat{\mathbf{p}}_k)\hat{\mathbf{\Phi}}_j^H\tilde{\mathbf{q}}_k^*.\end{aligned} \tag{4.43}$$

Then, we can use the same MMSE estimation properties to evaluate $\mathrm{Var}(\mathbf{g}_k|\hat{\mathbf{g}}_k)$ and $\mathrm{Var}(\mathbf{p}_k|\hat{\mathbf{p}}_k)$, which results in

$$\begin{aligned}\mathrm{Var}(\mathbf{g}_k|\hat{\mathbf{g}}_k) &= \mathbb{E}[\mathbf{g}_k\mathbf{g}_k^H] - \mathbb{E}[\mathbf{g}_k\hat{\mathbf{g}}_k^H](\mathbb{E}[\hat{\mathbf{g}}_k\hat{\mathbf{g}}_k^H])^{-1}\mathbb{E}[\hat{\mathbf{g}}_k\mathbf{g}_k^H],\\ &= \mathbf{\Sigma}_{\mathbf{g}_k} - \mathbf{C}_{\mathbf{gy}}\mathbf{C}_{\mathbf{yy}}^{-1}\mathbf{C}_{\mathbf{gy}}^H,\end{aligned} \tag{4.44a}$$

$$\begin{aligned}\mathrm{Var}(\mathbf{p}_k|\hat{\mathbf{p}}_k) &= \mathbb{E}[\mathbf{p}_k\mathbf{p}_k^H] - \mathbb{E}[\mathbf{p}_k\hat{\mathbf{p}}_k^H](\mathbb{E}[\hat{\mathbf{p}}_k\hat{\mathbf{p}}_k^H])^{-1}\mathbb{E}[\hat{\mathbf{p}}_k\mathbf{p}_k^H],\\ &= \mathbf{\Sigma}_{\mathbf{p}_k} - \mathbf{C}_{\mathbf{py}}\mathbf{C}_{\mathbf{yy}}^{-1}\mathbf{C}_{\mathbf{py}}^H.\end{aligned} \tag{4.44b}$$

Note that the analysis for Scheme 1 can be applied to the baseline scheme by adjusting the RIS configurations.

Scheme 2

When the scheme described in Section 4.6 is used during channel estimation and the beamforming vector is left unchanged throughout data transmission, the following received data signal model arises:

$$y_1 = \sqrt{P_d}\tilde{\mathbf{h}}_1^T\mathbf{\Phi}_1\mathbf{g}_1x_1 + w_1, \tag{4.45a}$$

$$y_2 = \sqrt{P_d}\tilde{\mathbf{h}}_2^T\mathbf{\Phi}_2\mathbf{g}_2x_2 + w_2. \tag{4.45b}$$

For the signal model in (4.37), it is shown in [16, Lemma 1] that the conditions for the bound in (4.35) to hold are satisfied. The same can be shown for (4.45) following the same steps.

In this scheme, we only estimate $\mathbf{g}_k$, therefore, the channel side information Ω corresponds to $\hat{\mathbf{g}}_k$. We can express this channel estimate as

$$\hat{\mathbf{g}}_k = \mathbf{g}_k + \mathbf{e}_k, \tag{4.46}$$

where $\mathbf{e}_k \sim \mathcal{CN}(\mathbf{0}, \mathbf{\Sigma}_{\mathbf{e}_k})$ with $\mathbf{\Sigma}_{\mathbf{e}_k}$ computed according to (4.7). To compute the capacity bound, we first have to define the overall SISO channel, that is,

$$v_k \triangleq \sqrt{P_d}\tilde{\mathbf{h}}_k^T \hat{\mathbf{\Phi}}_k \mathbf{g}_k. \tag{4.47}$$

Then, we should formulate its mean conditioned on $\mathbf{g}_k$, corresponding to the channel side information Ω in (4.35):

$$\mathbb{E}[v_k|\hat{\mathbf{g}}_k] = \sqrt{P_d}\tilde{\mathbf{h}}_k^T \hat{\mathbf{\Phi}}_k \mathbb{E}[\mathbf{g}_k|\hat{\mathbf{g}}_k] = \sqrt{P_d}\tilde{\mathbf{h}}_k^T \hat{\mathbf{\Phi}}_k \hat{\mathbf{g}}_k, \tag{4.48}$$

using the same LMMSE idea as before. Next, we have to evaluate $\mathrm{Var}(v_k|\hat{\mathbf{g}}_k)$, which can be expressed as

$$\begin{aligned}\mathrm{Var}(v_k|\hat{\mathbf{g}}_k) &= \mathrm{Var}\left(\sqrt{P_d}\tilde{\mathbf{h}}_k^T \hat{\mathbf{\Phi}}_k \mathbf{g}_k|\hat{\mathbf{g}}_k\right) \\ &= P_d \tilde{\mathbf{h}}_k^T \hat{\mathbf{\Phi}}_k \,\mathrm{Var}(\mathbf{g}_k|\hat{\mathbf{g}}_k)\hat{\mathbf{\Phi}}_k^H \tilde{\mathbf{h}}_k^*. \end{aligned} \tag{4.49}$$

What remains is to evaluate $\mathrm{Var}(\mathbf{g}_k|\hat{\mathbf{g}}_k)$, which can be done by using the same LMMSE idea as before:

$$\begin{aligned}\mathrm{Var}(\mathbf{g}_k|\hat{\mathbf{g}}_k) &= \mathbb{E}[\mathbf{g}_k\mathbf{g}_k^H] - \mathbb{E}[\mathbf{g}_k\hat{\mathbf{g}}_k^H](\mathbb{E}[\hat{\mathbf{g}}_k\hat{\mathbf{g}}_k^H])^{-1}\mathbb{E}[\hat{\mathbf{g}}_k\mathbf{g}_k^H], \\ &= \mathbf{\Sigma}_{\mathbf{g}_k} - \mathbf{C}_{\mathbf{gy}}\mathbf{C}_{\mathbf{yy}}^{-1}\mathbf{C}_{\mathbf{gy}}^H, \end{aligned} \tag{4.50}$$

which provides $\mathrm{Var}(v_k|\hat{\mathbf{g}}_k)$ in closed form. Note that w_k is independent of the channels and their estimates; therefore, it is obvious that $\mathrm{Var}(w_k|\Omega) = \sigma_w^2$. Since we also provided the closed-form expressions for $\mathbb{E}[v_k|\Omega]$ and $\mathrm{Var}(v_k|\Omega)$, we have the argument of the expectation in (4.35) in closed form. The final expressions for the capacity lower bound – for Scheme 1 (upper row) and Scheme 2 (lower row) – are shown in (4.51).

Ergodic Capacity

For both schemes, achieving perfect CSI is possible when the channel estimation SNR is sufficiently large since the pilot contamination is removed. Therefore, it is meaningful to consider the channel capacity itself under perfect CSI as a benchmark. Note that we consider the ergodic capacity since there are fading

$$C_k \geq \begin{cases} \mathbb{E}\left[\log_2\left(1+\frac{\left|\tilde{\mathbf{h}}_k\hat{\mathbf{\Phi}}_k\hat{\mathbf{g}}_k+\tilde{\mathbf{q}}_k\hat{\mathbf{\Phi}}_j\hat{\mathbf{p}}_k\right|^2}{\tilde{\mathbf{h}}_k^T\hat{\mathbf{\Phi}}_k(\mathbf{\Sigma}_{\mathbf{g}_k}-\mathbf{C}_{\mathbf{gy}}\mathbf{C}_{\mathbf{yy}}^{-1}\mathbf{C}_{\mathbf{gy}}^H)\hat{\mathbf{\Phi}}_k^H\tilde{\mathbf{h}}_k^*+\tilde{\mathbf{q}}_k^T\hat{\mathbf{\Phi}}_j(\mathbf{\Sigma}_{\mathbf{p}_k}-\mathbf{C}_{\mathbf{py}}\mathbf{C}_{\mathbf{yy}}^{-1}\mathbf{C}_{\mathbf{py}}^H)\hat{\mathbf{\Phi}}_j^H\tilde{\mathbf{q}}_k^*+\frac{\sigma_w^2}{P_d}}\right)\right], \\ \mathbb{E}\left[\log_2\left(1+\frac{\tilde{\mathbf{h}}_k\hat{\mathbf{\Phi}}_k\hat{\mathbf{g}}_k\hat{\mathbf{g}}_k^H\hat{\mathbf{\Phi}}_k^H\tilde{\mathbf{h}}_k^*}{\tilde{\mathbf{h}}_k^T\hat{\mathbf{\Phi}}_k(\mathbf{\Sigma}_{\mathbf{g}_k}-\mathbf{C}_{\mathbf{gy}}\mathbf{C}_{\mathbf{yy}}^{-1}\mathbf{C}_{\mathbf{gy}}^H)\hat{\mathbf{\Phi}}_k^H\tilde{\mathbf{h}}_k^*+\frac{\sigma_w^2}{P_d}}\right)\right], \end{cases} \tag{4.51}$$

channel components. In addition, we assume that both operators configure their RISs so that

$$\boldsymbol{\phi}_1 = \exp\Big(-j(\arg(\tilde{\mathbf{h}}_1)+\arg(\mathbf{g}_1))\Big), \tag{4.52a}$$

$$\boldsymbol{\phi}_2 = \exp\Big(-j(\arg(\tilde{\mathbf{h}}_2)+\arg(\mathbf{g}_2))\Big). \tag{4.52b}$$

Recall that we had defined the effective SISO channel for the two schemes as v_k. By plugging in the definitions of v_k into

$$C_k = \mathbb{E}\left[\log_2\left(1+\frac{|v_k|^2}{\sigma_w^2}\right)\right], \tag{4.53}$$

the ergodic capacity for the scheme of interest can be obtained.

4.8 Extension to Multiple Users

The focus of this paper is on the idea of null forming towards the interfering channel to mitigate inter-operator pilot contamination. Therefore, we considered a single user per operator case to improve the readability of this manuscript. In this section, however, we briefly describe how to generalize the system model in Section 4.2 for multiple users.

Suppose that each operator serves R_k users. Note that we need to have $R_1, R_2 \leq N$ since $M \geq N$ and the overall MIMO channel's rank is limited by N. In addition, we can no longer consider the pure-LOS case since the RIS-BS links would be rank-1 and hence would be unable to support $R_k > 1$ users. Therefore, we make the assumption that $R_1, R_2 \leq N \leq M$ and $\text{rank}(\mathbf{H}_k) \geq R, \text{rank}(\mathbf{Q}_k) \geq R$ for $k = 1, 2$, that is, all RIS-BS channels have at least R non-zero singular values. With this in mind, we can express the multi-user version of (4.1), the R_k-dimensional received pilot signal, as

$$\mathbf{y}_{pk}[l] = \sqrt{P_p}\mathbf{V}_k(\mathbf{H}_k\mathbf{\Phi}_k[l]\mathbf{G}_k + \mathbf{Q}_k\mathbf{\Phi}_j[l]\mathbf{P}_k)\mathbf{s}_k[l] + \underbrace{\mathbf{V}_k\mathbf{n}_k[l]}_{\triangleq\mathbf{w}_k[l]}, \tag{4.54}$$

where the r-th row of $\mathbf{V}_k \in \mathbb{C}^{R_k\times M}$ contains the receive beamforming vector that outputs the r-th user's received signal. $\mathbf{G}_k, \mathbf{P}_k \in \mathbb{C}^{N\times R_k}$ denote the UEs-RIS channels whose columns contain the individual users' channels to the RIS.

$\mathbf{s}_k[l] \in \mathbb{C}^{R_k \times 1}$ is the vector of pilots transmitted by the UEs at the l-th time instant. By defining the effective RIS-BS channels $\tilde{\mathbf{H}}_k \triangleq \mathbf{V}_k\mathbf{H}_k \in \mathbb{C}^{R_k \times N}$ and $\tilde{\mathbf{Q}}_k \triangleq \mathbf{V}_k\mathbf{Q}_k \in \mathbb{C}^{R_k \times N}$, we can rewrite (4.54) as

$$\mathbf{y}_{pk}[l] = \sqrt{P_p}(\tilde{\mathbf{H}}_k\mathbf{\Phi}_k[l]\mathbf{G}_k + \tilde{\mathbf{Q}}_k\mathbf{\Phi}_j[l]\mathbf{P}_k)\mathbf{s}_k[l] + \mathbf{w}_k[l]. \tag{4.55}$$

This time, the individual rows of $\mathbf{V}_k$ will undergo the beamforming design processes described in Section 4.5. To separate the main lobes of the beams, each row will have to be assigned one of the right singular vectors of $\mathbf{H}_k$, and each row will undergo the null forming process in case Scheme 2 is used. If $\mathbf{V}_k = \begin{bmatrix}\mathbf{v}_{k,1}^T & \dots & \mathbf{v}_{k,R_k}^T\end{bmatrix}^T$, then the beamforming process in Section 4.5 becomes:

$$\mathbf{v}_{k,1}^T = \boldsymbol{\gamma}_{k,1}^H \tag{4.56a}$$
$$\mathbf{v}_{k,2}^T = \boldsymbol{\gamma}_{k,2}^H \tag{4.56b}$$
$$\vdots$$
$$\mathbf{v}_{k,R_k}^T = \boldsymbol{\gamma}_{k,R_k}^H, \tag{4.56c}$$

where $\boldsymbol{\gamma}_{k,1}, \dots, \boldsymbol{\gamma}_{k,R_k}$ are the R_k right singular vectors of $\mathbf{H}_k$ corresponding to the R_k largest singular values of $\mathbf{H}_k$. Starting from this point, every vector would undergo the process in Section 4.5 if null forming is to be utilized.

4.9 Numerical Results

In this section, we discuss numerical examples for the channel estimation and capacity lower bound analysis to demonstrate the benefits of mitigating inter-operator pilot contamination. In Section 4.9, we provide the numerical results for channel estimation for the two schemes for pure-LOS and unstructured RIS-BS channels. In Section 4.9, we simulate the outer expectation over multiple channel realizations and compare the two schemes for pure-LOS and unstructured channels. To show that eliminating inter-operator pilot contamination is necessary, we construct a baseline scheme that transmits $L = N$ pilots and uses the same beamformer as Scheme 1. That is, the baseline scheme does not eliminate inter-operator pilot contamination by receive beamforming or orthogonalizing RIS configurations. It has to be noted that regularized zero forcing (RZF) beamforming, a state-of-the-art method, is not included in the analysis as our numerical results (not shown here) indicate that Scheme 2 provides the same performance as the RZF approach.

Channel Estimation Based on Correlated Rayleigh Fading Priors

In this section, we provide numerical examples for estimating correlated Rayleigh fading channels. We consider the two schemes described in Sections 4.6 and 4.6, along with the baseline scheme described at the beginning of this section. For

different P_p, we compute the NMSE of MMSE channel estimation, which is given by

$$\mathrm{NMSE}_{\mathbf{g}_k} = \frac{\mathrm{tr}(\mathbf{\Sigma}_{\mathbf{e}_{\mathbf{g}_k}})}{\mathrm{tr}(\mathbf{\Sigma}_{\mathbf{g}_k})}, \tag{4.57a}$$

$$\mathrm{NMSE}_{\mathbf{p}_k} = \frac{\mathrm{tr}(\mathbf{\Sigma}_{\mathbf{e}_{\mathbf{p}_k}})}{\mathrm{tr}(\mathbf{\Sigma}_{\mathbf{p}_k})}, \tag{4.57b}$$

where $\mathbf{\Sigma}_{\mathbf{e}_{\mathbf{g}_k}}$ and $\mathbf{\Sigma}_{\mathbf{e}_{\mathbf{p}_k}}$ are as in (4.7). In Figs. 4.2 and 4.3, the channel estimation NMSEs for $\mathbf{g}_1$ and $\mathbf{p}_1$[2] are shown for $N = 64$ and $M = 256$. The list of parameters used for these figures is provided in Table 4.2. Note that although our analysis is valid for any positive definite covariance matrix of $\mathbf{g}_k$ and $\mathbf{p}_k$, we consider i.i.d. Rayleigh fading in this section. That is, $\mathbf{g}_k, \mathbf{p}_k \sim \mathcal{CN}(\mathbf{0}, \mathbf{I}_N)$.

In Fig. 4.2, note that $\mathbf{p}_1$ has a much higher NMSE than $\mathbf{g}_1$ for both Scheme 1 and the baseline scheme. This is because the BS beamforms towards $\mathbf{H}_1$ rather than $\mathbf{Q}_1$ in both schemes, therefore, the channel estimation SNR is boosted significantly. Since both $\mathbf{H}_1$ and $\mathbf{Q}_1$ are pure-LOS channels, they are also directive and are highly separated angularly. Therefore, beamforming towards $\mathbf{H}_1$ decreases the received pilot SNR along the $\mathbf{p}_1$-$\mathbf{Q}_1$ path significantly. In addition, note that $\mathbf{g}_1$ is estimated more accurately under Scheme 1 compared to Scheme 2. This is because null forming towards $\mathbf{Q}_1$ weakens the main lobe of the beam. Also note that the baseline scheme performs similarly with Scheme 2 until $P_p = 45$ dBm and starts to converge to a finite value. Also note that this is the point where the NMSEs of estimating $\mathbf{p}_1$ for Scheme 1 and the baseline scheme starts to be visible. It has to be noted that the baseline scheme uses the same beamforming vector as Scheme 1, therefore, the difference between Scheme 1 and the baseline scheme's performance in estimating $\mathbf{g}_1$ comes from the fact that $L = 2N$ pilots are used in Scheme 1 while $L = N$ pilots are used in the baseline scheme. Therefore, the gap between them is around 3 dB.

In Fig. 4.3, note that $\mathbf{p}_1$ has higher NMSE than $\mathbf{g}_1$ since the beamforming is towards the dominant singular vector of $\mathbf{H}_1$. However, the gap is not as large as that in Fig. 4.2 since both channels exhibit rich scattering in this case. For $\mathbf{g}_1$, Scheme 1 provides slightly better channel estimates than Scheme 2 since null forming towards $\mathbf{Q}_1$ takes away from the beam towards $\mathbf{H}_1$ resulting in lower gain. Note that compared to the pure-LOS case, the baseline scheme has much worse performance, starting to show the impact of inter-operator pilot contamination at around 15 dBm. After around 30 dBm, the NMSE of the baseline scheme converges to a constant, which is the pilot contamination term.

Note that when there is pure-LOS between the RISs and the BSs, the baseline scheme performs similarly to Scheme 2 up to a transmit power of $P_p = 50$ dBm as shown in Fig. 4.2. On the other hand, the baseline scheme has inferior performance when the RIS-BS links do not exhibit any structure, as shown in Fig. 4.3.

[2]Note that the same results can also be obtained for $k = 2$; however, we show the results for the first operator to keep the figures readable.

Table 4.2: Parameters used in Figures 4.2 and 4.3.

Parameter	Value
Transmit pilot power (P_p)	$-30, -25, \ldots, 60$ dBm
Carrier frequency (f_c)	30 GHz, 28 GHz[3]
UE-RIS path loss	-80 dB
RIS-BS path loss	-60 dB
Noise variance (σ_w^2)	-90 dBm
Number of BS antennas (M)	256
Number of RIS elements (N)	64
Number of pilot transmissions (L)	N, $2N$

This is a consequence of the beam structures for the two cases. For the pure-LOS case, the intended and interfering channels are already well-separated in space, and the absence of nullforming does not degrade the performance much. That is, there is much less inter-operator pilot contamination when there is pure-LOS between the RISs and the BSs when compared to the case where the RIS-BS channels do not exhibit any structure.

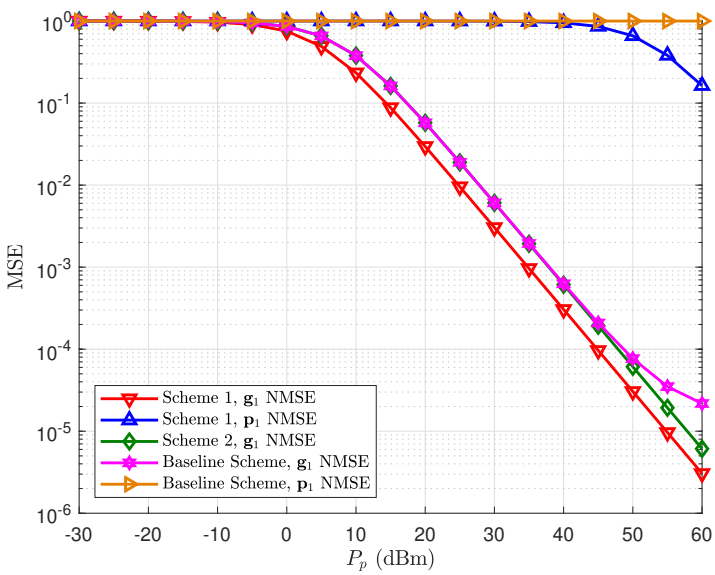

Figure 4.2: Channel estimation NMSE of $\mathbf{g}_1$ and $\mathbf{p}_1$ for the two schemes when $\mathbf{H}_k$ and $\mathbf{Q}_k$ are pure-LOS channels.

[3]Operators 1 and 2 use these frequencies and their respective BSs and RISs have $\lambda_k/2$ inter-element spacings according to these frequencies.

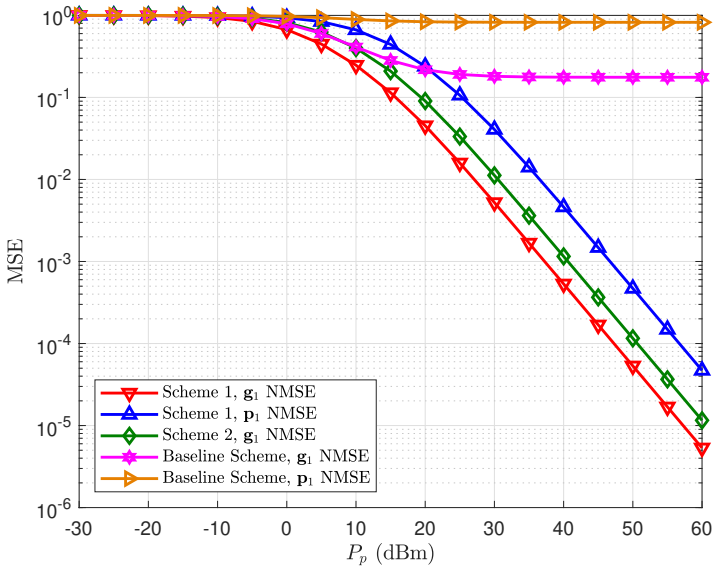

Figure 4.3: Channel estimation NMSE of $\mathbf{g}_1$ and $\mathbf{p}_1$ for the two schemes when $\mathbf{H}_k$ and $\mathbf{Q}_k$ do not exhibit any structure.

Capacity Lower Bound for Reliable Communication Under Imperfect CSI

In this section, we provide numerical examples for the capacity lower bound expression in Section 4.7. While the results in Section 4.9 demonstrated that Scheme 1 provides higher capacity, one should consider the fact that Scheme 2 and the baseline scheme uses half of the pilots used in Scheme 1, i.e., $L = N$ instead of $L = 2N$. To treat the two schemes fairly, we consider a fictitious slot structure where L pilot transmissions are followed by D data transmissions. During the data transmission phase, we assume that the capacity bounds or the ergodic capacities apply, and hence we compute the throughput over $L+D$ channel uses. We assume that a single coherence block lasts for $3N$ transmissions. For both schemes, we use the minimum number of pilots, i.e., $L = 2N$ for Scheme 1 and $L = N$ for Scheme 2 and the baseline scheme. Then, we consider the spectral efficiency (SE) and its lower bound. Suppose that the channel capacity is C, then the SE is $\frac{D}{D+L}C$ since we use the channel $D + L$ times and we transmit data in D of these instances. Since a single coherence block lasts $3N$ transmissions, we perform $D = N$ data transmissions in Scheme 1 and $D = 2N$ data transmissions in Scheme 2 and the baseline scheme. Consequently, we transmit data $1/3$ of the time in Scheme 1 and $2/3$ of the time in Scheme 2 and the baseline scheme.

Table 4.3: Parameters used in Figures 4.4 and 4.5.

Parameter	Value
Transmit data power (P_d)	$-30, -10, \ldots, 130$ dBm
Transmit pilot power (P_p)	P_d[4]
UE-RIS path loss	-80 dB
RIS-BS path loss	-60 dB
Noise variance (σ_w^2)	-90 dBm
Number of BS antennas (M)	256
Number of RIS elements (N)	64
Number of pilot transmissions (L)	N, $2N$
Number of data transmissions (D)	$2N$, N

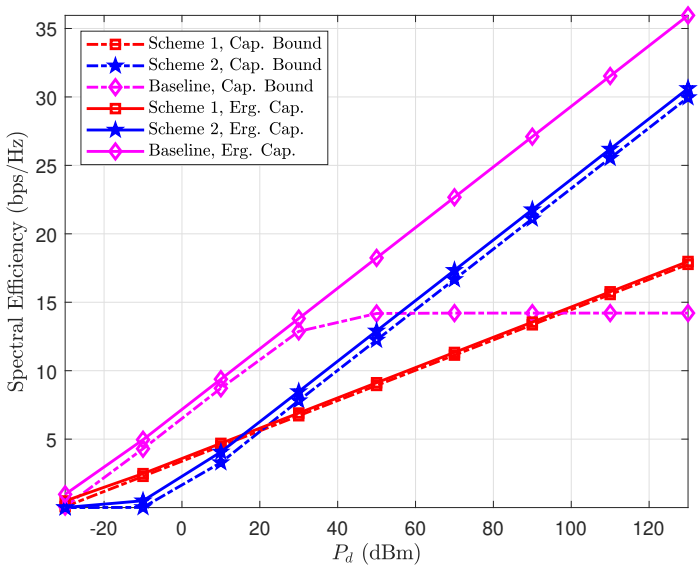

Figure 4.4: Capacity lower bound and the ergodic capacity for the two schemes and the baseline scheme when $\mathbf{H}_1$ and $\mathbf{Q}_1$ are pure-LOS. The dashed lines represent the capacity lower bound in (4.35) and the solid lines represent the ergodic capacity in (4.53).

In Figs. 4.4 and 4.5, note that the capacity bound curves for Schemes 1 and 2 follow the ergodic capacity curves closely, showing that perfect CSI is indeed achievable at sufficiently high pilot transmission power. In contrast, the capacity lower bound for the baseline scheme diverges from its corresponding

[4]Each point of the capacity bound plot in Fig. 4.4 and 4.5 corresponds to the case when the pilot and data transmission powers are equal to each other. On the other hand, ergodic capacity is based on perfect CSI.

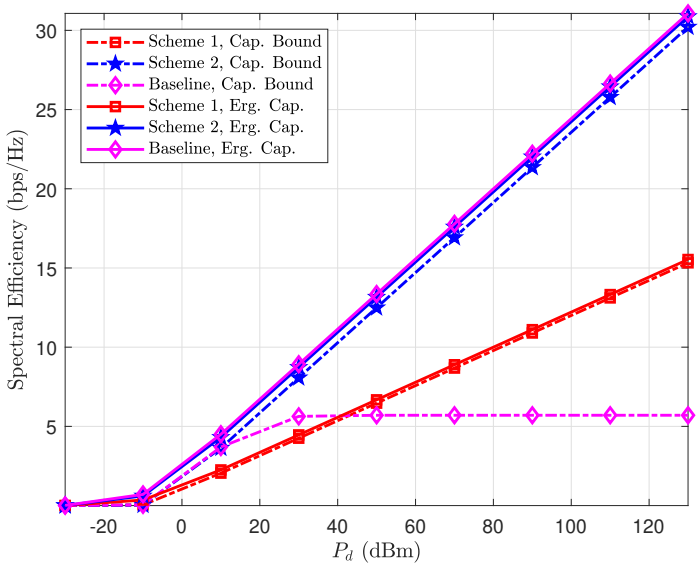

Figure 4.5: Capacity lower bound and the ergodic capacity for the two schemes and the baseline scheme when $\mathbf{H}_1$ and $\mathbf{Q}_1$ do not exhibit any structure. The dashed lines represent the capacity lower bound in (4.35) and the solid lines represent the ergodic capacity in (4.53).

ergodic capacity curve after $P_d = 30$ dBm for Fig. 4.4 and $P_d = -10$ dBm for Fig. 4.5.

In Fig. 4.4, the baseline scheme outperforms Schemes 1 and 2 at low transmit powers since the signal power is scarce, and the baseline scheme neither sacrifices its beam's main lobe nor doubles the number of pilots. After $P_d = 50$ dBm, however, the baseline scheme is penalized by the inter-operator pilot contamination despite the strong spatial separation between the intended and the interfering channels. Consequently, Schemes 1 and 2 outperform the baseline scheme starting from $P_d = 60$ dBm and $P_d = 90$ dBm, respectively. Although Scheme 1 outperforms Scheme 2 until around $P_d = 20$ dBm due to the scarcity of signal power, Scheme 2 outperforms Scheme 1 at higher transmit powers thanks to fewer pilots. Therefore, it can be inferred from Fig. 4.4 that given pure-LOS conditions between the BSs and the RISs, the baseline scheme is preferable over the two schemes when transmit power is limited. In contrast, Scheme 2 provides the best performance when the transmit power is high.

While there exists a region where baseline scheme prevails when pure-LOS RIS-BS channels exist, this is not the case when these channels do not exhibit any structure, as seen in Fig. 4.5. The two schemes that eliminate inter-operator pilot contamination consistently outperform the baseline scheme as the intended

and the interfering channels are not well-separated over space. That is, pilot contamination has to be eliminated either at the RISs or the BS. Also, note that Scheme 2 outperforms both Scheme 1 and Scheme 2 almost everywhere in Fig. 4.5. Therefore, one can infer that Scheme 2 provides the best performance when the RIS-BS channels do not exhibit any structure.

4.10 Conclusions

In this paper, we investigated the use of receive beamforming to combat inter-operator pilot contamination in RIS-aided wireless systems where two operators share a site and utilize different RISs to serve their respective users. We considered uplink channel estimation and data transmission and proposed using receive beamforming at the BSs to remove the interference coming from the other operator's RIS by placing a null towards the respective channel. We considered two different schemes. In Scheme 1, the BS beamforms towards its intended channel without placing a null towards the interfering channel. The RISs configurations during the pilot transmission phase are orthogonalized to eliminate inter-operator pilot contamination. In Scheme 2, a null is placed towards the interfering RIS-BS channel to cut off the interfering transmission and reflection path. As the inter-operator pilot contamination is removed at the BS, the RISs configurations are not orthogonalized, hence the number of pilots used in the channel estimation phase is halved. We investigated the performance of these two schemes when the RIS-BS channels are pure-LOS and when they are unstructured in terms of channel estimation MSE, the resulting capacity lower bounds under imperfect CSI and the ergodic capacities. Our numerical results show that at high transmit powers, Scheme 2 outperforms Scheme 1 and the baseline scheme in terms of capacity lower bound due to a lower number of pilots and matching channel estimation performance. While Scheme 2 prevails at high transmit powers for both pure-LOS and unstructured RIS-BS channel scenarios, this is not the case at low transmit powers. The extra energy captured by Scheme 1 and the baseline scheme gains importance when the transmit power is low. In addition, the baseline scheme uses half as many pilots as Scheme 1, and it is not affected much by the inter-operator pilot contamination when the RIS-BS channels are pure-LOS. This is because, the baseline scheme beamforms towards its intended channel, inevitably reducing its gain from the interfering channel. In contrast, Schemes 1 and 2 consistently outperform the baseline scheme when the RIS-BS channels are unstructured since beamforming towards the intended channel does not reduce the gain from the interfering channel. In addition, we also showed that Scheme 2 consistently outperforms both schemes in such scenarios. Therefore, we can conclude that the proposed scheme to eliminate inter-operator pilot contamination by receive beamforming is highly beneficial at high transmission powers, and the cases where the baseline scheme prevails are limited to pure-LOS RIS-BS channels and low transmission powers.

Since we focused on the idea of placing a null towards the interfering channel and eliminating pilot contamination in this work, we kept the rest of the system model rather simple and tractable. However, further work can be done on how this scheme performs under different channel characteristics and when multiple users are served. In Section 4.8, we provided the system model formulation for the multi-user case. However, further analysis is required to identify how to handle the multi-user beamforming problem.

Chapter 5

Joint Pilot-Based Localization and Channel Estimation in RIS-Aided Communication Systems

Abstract

In this letter, we investigate the use of reconfigurable intelligent surfaces (RISs) to jointly estimate the position and channel of a user equipment (UE) using uplink pilot signals. We consider a setup with a user and a base station (BS), where the direct path between the BS and the UE is blocked and virtual line-of-sight (LOS) links are created over two reconfigurable intelligent surfaces (RISs). We investigate the benefits of exploiting the channel geometry to estimate the user's position and the user-RIS channels jointly in terms of estimation performance and pilot overhead. To this end, we consider the Cramér-Rao Lower Bound for channel estimation and UE localization. Our numerical results show that exploiting the LOS structure of the channels improves the channel estimation performance by several orders of magnitude and reduces the channel estimation performance by reducing the number of unknown parameters.

5.1 Introduction

The rapid advancements of wireless communication systems have been driven by the ever-increasing demand for throughput, coverage, and reliability due to social habits altered by advancing technology. As a result, the current demands for the sixth generation of wireless communication systems (6G) require a set of key enabling technologies, one of which is RIS [22]. An RIS is a passive device consisting of multiple meta-material-based elements whose reflective properties are externally controllable, which allows a partial manipulation of the propagation environment in favor of communicating UEs [23, 66].

As 6G is designed as a multi-functional system offering massive connectivity, localization, and sensing services [67], there exists a multitude of studies considering RIS-aided localization systems and their synergies with communication systems. In [68], RIS-aided localization and sensing are discussed from a signal processing perspective. It is discussed that the RIS acts not only as an additional anchor node for localization but also as an entity boosting the system performance via configuration optimization. In [69], an RIS-aided near-field localization system is considered under phase-dependent amplitude variations of the RIS elements. In [70], RIS-aided localization is considered when some of the RIS elements fail with a certain probability. Such hardware impairments significantly affect localization performance since the system extracts sensitive geometric information from the observations to obtain the user location. On the other hand, for pure communication purposes, the unstructured channel estimates usually suffice. Nevertheless, localization information has the potential to boost communication performance significantly since the user location implicitly provides a significant portion of the CSI, especially in LOS-dominant channels. To utilize this potential, synergies between localization and communication are investigated throughout the literature.

In [71], a strategy to optimize the RIS for localization and sensing is proposed.. Additionally, a user tracking scheme is also proposed in this study. In [72], position estimates are used for channel estimation. In [73], location information is used to aid the communication system by estimating AoDs from Rician channel estimates.

For LOS channels in particular, there are direct relations between the geometric parameters and the channel coefficients, therefore, it is rather straightforward to estimate the channel based on the information obtained from localization. However, these relations are highly nonlinear, therefore, the achievable estimation performance is highly dependent on the values of the parameters. Therefore, theoretical analysis of the achievable estimation performance is necessary for all possible values of the parameters. To this end, we consider the uplink of a two-RIS indoor communication system, where the BS localizes a single UE and estimates its channel based on the location estimate. The BS utilizes the same set of pilot transmissions for both tasks by estimating the channel gain, propagation delay, and AoAs of the signals impinging on both RISs, and using the RIS and system geometry to estimate the channel and the UE position. As our performance metric for location and channel estimation, we consider the CRLB, which provides a lower bound on the variance of any unbiased estimator. In addition, we consider the use of parameter estimates for channel estimation as a potential solution for the additional pilot overhead caused by using multiple RISs demonstrated in [16]. Our contributions in this letter can be summarized as follows:

- For both channel estimation and user localization, we provide the CRLB on the MSE in closed form for all user locations.

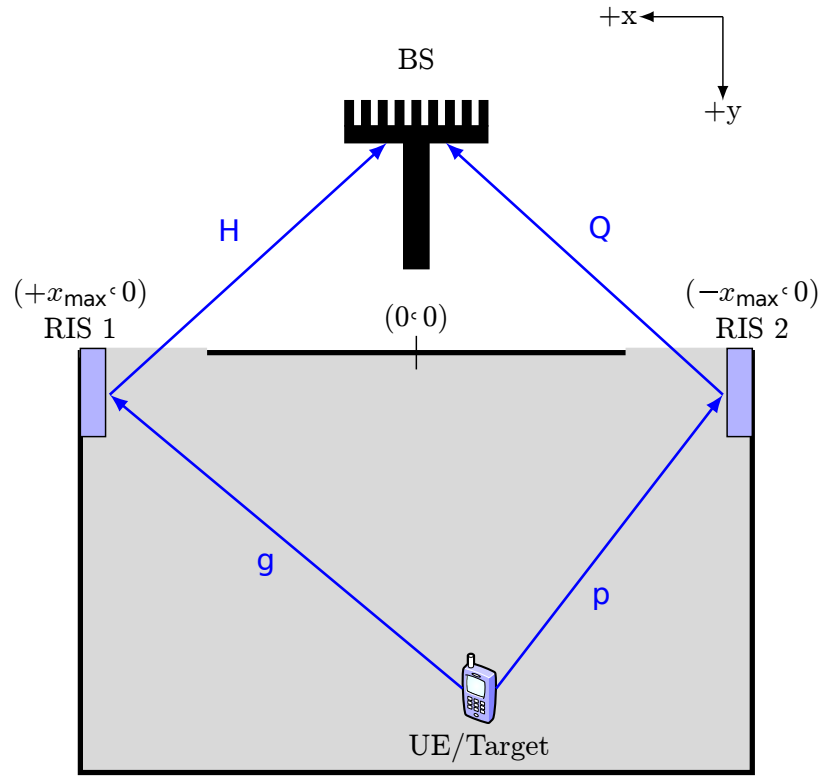

Figure 5.1: Two-RIS localization system. The coordinate system within the room is specified with the axis arrows in the upper right corner of the figure, and the origin of the coordinate system corresponds to the point marked in the middle of the two side walls on which the RISs are mounted on, and on the receiver-side wall. The room is $2x_{\max}$ meters wide, that is, RIS 1 and RIS 2 are located at the coordinates $(+x_{\max}, 0)$ and $(-x_{\max}, 0)$ respectively. The room extends down the y-axis up to $y_{\max}$ meters, i.e., the rear corners correspond to $(+x_{\max}, +y_{\max})$ and $(-x_{\max}, +y_{\max})$.

- In the presence of multiple RISs, we show that parametric channel estimation yields more accurate channel estimates with fewer pilot transmissions than non-parametric channel estimation. We demonstrate this by comparing the CRLBs on parametric and non-parametric channel estimation MSEs, where the non-parametric estimation scheme uses twice as many pilots as the parametric estimation scheme does.

5.2 System Model

We consider the indoor joint communication and localization setup aided by two RISs illustrated in Fig. 2.1. The matrices $\mathbf{H} \in \mathbb{C}^{M \times N}$ and $\mathbf{Q} \in \mathbb{C}^{M \times N}$ denote

the static and known channels between the RISs and the M-antenna BS, where N is the number of elements in each RIS. Moreover, the channels between the unknown target/UE to the RISs, assumed to be purely LOS, are denoted by $\mathbf{g} \in \mathbb{C}^N$ and $\mathbf{p} \in \mathbb{C}^N$. The signal received after a single pilot transmission can be expressed as

$$\mathbf{y}_p = \sqrt{P_p}(\mathbf{H}\boldsymbol{\Phi}_1\mathbf{g} + \mathbf{Q}\boldsymbol{\Phi}_2\mathbf{p})s + \mathbf{w} \ \in \mathbb{C}^{M\times 1}, \tag{5.1}$$

where P_p denotes the pilot transmission power, $\boldsymbol{\Phi}_k = \text{Diag}(e^{-j\phi_{k1}}, \ldots, e^{-j\phi_{kN}}) \in \mathbb{C}^{N\times N}$ denotes the diagonal response matrix of RIS k, $s \in \mathbb{C}$ denotes the transmitted positioning reference signal, and $\mathbf{w} \sim \mathcal{CN}(\mathbf{0}, \sigma_w^2\mathbf{I}_M)$ denotes the additive receiver noise. When considering the estimation of channel-related parameters, it is more convenient to rewrite (5.1) as

$$\mathbf{y}_p = \sqrt{P_p}(\boldsymbol{\phi}_1\mathbf{D}_\mathbf{H}\mathbf{g} + \boldsymbol{\phi}_2\mathbf{D}_\mathbf{Q}\mathbf{p})s + \mathbf{w} \in \mathbb{C}^{M\times 1}, \tag{5.2}$$

where $\mathbf{D}_\mathbf{H} \triangleq \text{Diag}(\mathbf{H}_1, \ldots, \mathbf{H}_N) \in \mathbb{C}^{MN\times N}$, $\mathbf{D}_\mathbf{Q} \triangleq \text{Diag}(\mathbf{Q}_1, \ldots, \mathbf{Q}_N) \in \mathbb{C}^{MN\times N}$ with $\mathbf{H}_n$ and $\mathbf{Q}_n$ denoting the n-th columns of $\mathbf{H}$ and $\mathbf{Q}$, respectively, and $\boldsymbol{\phi}_k = \text{diag}(\boldsymbol{\Phi}_k) \otimes \mathbf{I}_M \in \mathbb{C}^{MN\times M}$ for $k = 1, 2$. $\mathbf{D}_\mathbf{H}$ and $\mathbf{D}_\mathbf{Q}$ are block diagonal matrices built of $M \times 1$ blocks, and the diagonal blocks contain the individual columns of $\mathbf{H}$ and $\mathbf{Q}$. Assuming that the pilot transmission is repeated over time $L \geq N$ times with varying RIS configurations and $s[l] = 1$ for $l = 1, \ldots, L$, we can express the collection of observations $\mathbf{Y}_p \triangleq [\mathbf{y}_p^T[1], \ldots, \mathbf{y}_p^T[L]]^T$ as

$$\mathbf{Y}_p = \sqrt{P_p}(\mathbf{B}_1\mathbf{D}_\mathbf{H}\mathbf{g} + \mathbf{B}_2\mathbf{D}_\mathbf{Q}\mathbf{p}) + \mathbf{W} \in \mathbb{C}^{LM}, \tag{5.3}$$

where $\mathbf{B}_k \triangleq [\boldsymbol{\phi}_k[1], \ldots, \boldsymbol{\phi}_k[L]]^T \in \mathbb{C}^{LM\times MN}$ and $\mathbf{W} \sim \mathcal{CN}(\mathbf{0}, \sigma_w^2\mathbf{I}_{LM})$. Note that $\phi_k[l]$ also contains the pilot signals $s[l]$, however, since we choose $s[l] = 1$ for $l = 1, \ldots, L$, $\phi_k[l]$ are the same as the RIS configruations.

Since we consider purely LOS channels, the unknown $\mathbf{g}$ and $\mathbf{p}$ channels are structured based on the RIS geometries, attenuation, and propagation delay. For both RISs, we consider the ULA geometry and perform 2D localization in the far-field region. Based on the azimuth AoAs φ_1 and φ_2 on RIS 1 and RIS 2, respectively, $\mathbf{g}$ and $\mathbf{p}$ can be expressed as

$$\mathbf{g} = \sqrt{\alpha_1}e^{-j2\pi f_c\tau_1}\mathbf{a}(\varphi_1), \tag{5.4a}$$

$$\mathbf{p} = \sqrt{\alpha_2}e^{-j2\pi f_c\tau_2}\mathbf{a}(\varphi_2), \tag{5.4b}$$

where $\mathbf{a}(\varphi) = \begin{bmatrix}1 & e^{-j2\pi\frac{\Delta}{\lambda}\sin(\varphi)} & \ldots & e^{-j2\pi(N-1)\frac{\Delta}{\lambda}\sin(\varphi)}\end{bmatrix}^T$ denotes the array steering vector for the ULA geometry. In the next section, we derive the CRLB on the channel estimation MSE and the UE localization error.

5.3 CRLB on Localization and Channel Estimation

In a parameter estimation problem, it is useful to determine an achievable lower bound on the estimation performance to serve as the gold standard. The CRLB—the inverse of the FIM—provides a lower bound on the MSE of any unbiased

estimator [12] via the following matrix inequality:

$$\mathrm{Cov}(\hat{\boldsymbol{\theta}}(\mathbf{X})) \succeq \mathbf{I}^{-1}(\mathbf{X};\boldsymbol{\theta}) \tag{5.5}$$

for an estimate of a parameter vector $\boldsymbol{\theta}$ based on an observation vector $\mathbf{X}$. Here, $\mathrm{Cov}(\hat{\boldsymbol{\theta}}(\mathbf{X})) = \mathbb{E}[(\hat{\boldsymbol{\theta}}(\mathbf{X}) - \boldsymbol{\theta})(\hat{\boldsymbol{\theta}}(\mathbf{X}) - \boldsymbol{\theta})^H]$ is the covariance matrix and, consequently, the bound on the sum MSE can be expressed as

$$\mathbb{E}[\|\hat{\boldsymbol{\theta}}(\mathbf{X}) - \boldsymbol{\theta}\|^2] \geq \mathrm{tr}\left(\mathbf{I}^{-1}(\mathbf{X};\boldsymbol{\theta})\right). \tag{5.6}$$

In a generic vector parameter estimation problem, the FIM is computed via the following equation [28, Eq. 3.21]:

$$[\mathbf{I}(\mathbf{X};\boldsymbol{\theta})]_{ij} = -\mathbb{E}\left[\frac{\partial^2 \ln(f(\mathbf{X};\boldsymbol{\theta}))}{\partial\theta_i\theta_j}\right], \tag{5.7}$$

where $f(\mathbf{X};\boldsymbol{\theta})$ denotes the likelihood function of the observation $\mathbf{X}$ based on the unknown vector parameter $\boldsymbol{\theta}$. In our channel estimation problem, the received pilot signal in (5.3) can be expressed as

$$\mathbf{Y}_p = \sqrt{P_p}\underbrace{\begin{bmatrix}\mathbf{B}_1\mathbf{D}_{\mathbf{H}} & \mathbf{B}_2\mathbf{D}_{\mathbf{Q}}\end{bmatrix}}_{\triangleq\mathbf{F}}\underbrace{\begin{bmatrix}\mathbf{g}\\ \mathbf{p}\end{bmatrix}}_{\triangleq\mathbf{v}} + \mathbf{W}. \tag{5.8}$$

Here, $\mathbf{v}$ denotes the ensemble of unknown channel coefficients without any LOS parametrization. In this form, we have a linear observation model with additive complex Gaussian noise. Consequently, it is much easier to compute the FIM here than explicitly differentiating the log-likelihood function as one would do for a generic parameter-observation model. Using this special form of the observation model in (5.8), the FIM can be expressed as

$$\mathbf{I}(\mathbf{Y}_p;\mathbf{v}) = P_p\mathbf{F}^H\mathbf{I}(\mathbf{W})\mathbf{F}, \tag{5.9}$$

where $\mathbf{I}(\mathbf{W})$ denotes the FIM with respect to a translation parameter defined in [74, Eq. 8]. Since $\mathbf{w}$ is Gaussian, it satisfies the relation $\mathbf{I}(\mathbf{W}) \succeq \frac{1}{\sigma_w^2}\mathbf{I}$ in [74, Eq. 10] with equality. Therefore, (5.9) can be simplified as

$$\mathbf{I}(\mathbf{Y}_p;\mathbf{v}) = \frac{P_p}{\sigma_w^2}\mathbf{F}^H\mathbf{F} \in \mathbb{C}^{2N\times 2N}. \tag{5.10}$$

The rank of (5.10) depends on the column rank of $\mathbf{F}$, which depends on the choice of $\mathbf{B}_1$ and $\mathbf{B}_2$. To ensure that the FIM is non-singular, one must have $L \geq 2N$, and $\mathbf{F}$ must have full column rank. To this end, it is tempting to choose $\mathbf{B}_1$ and $\mathbf{B}_2$ such that $\mathbf{B}_1^H\mathbf{B}_2 = \mathbf{0}$ as this configuration allows the pilot signals to explore all the unknown dimensions of the channel. When the channels $\mathbf{g}_k$ and $\mathbf{p}_k$ do not exhibit any structure, this method provides accurate channel estimates, as shown

in [16]. For the non-parametric channel estimation problem, the signal model is as in (5.8), and the ML estimate of $\mathbf{v}$ can be expressed as

$$\hat{\mathbf{v}} = \frac{1}{\sqrt{P_p}}(\mathbf{F}^H\mathbf{F})^{-1}\mathbf{F}^H\mathbf{y}_p. \tag{5.11}$$

For (5.11) to exist, $\mathbf{F}^H\mathbf{F}$ should be invertible, which is maintained by choosing $\mathbf{B}_1^H\mathbf{B}_2 = \mathbf{0}$. This also implies that the FIM is invertible, that is the CRLB exists and can be expressed as

$$\mathbf{I}^{-1}(\mathbf{Y}_p; \mathbf{v}) = \frac{\sigma_w^2}{P_p}(\mathbf{F}^H\mathbf{F})^{-1}. \tag{5.12}$$

On the other hand, the error covariance matrix achieved by (5.11) becomes

$$\begin{aligned}
&\mathbb{E}[(\hat{\mathbf{v}} - \mathbf{v})(\hat{\mathbf{v}} - \mathbf{v})^H] = \mathbb{E}[\hat{\mathbf{v}}\hat{\mathbf{v}}^H] + \mathbf{v}\mathbf{v}^H - 2\mathrm{Re}\{\mathbb{E}[\hat{\mathbf{v}}\mathbf{v}^H]\} \\
&= \frac{1}{P_p}(\mathbf{F}^H\mathbf{F})^{-1}\mathbf{F}^H\mathbb{E}[\mathbf{y}_p\mathbf{y}_p^H]\mathbf{F}(\mathbf{F}^H\mathbf{F})^{-1} \\
&+ \mathbf{v}\mathbf{v}^H - 2\mathrm{Re}\left\{\frac{1}{\sqrt{P_p}}(\mathbf{F}^H\mathbf{F})^{-1}\mathbf{F}^H\mathbb{E}[\mathbf{y}_p\mathbf{v}^H]\right\} \\
&= \mathbf{v}\mathbf{v}^H + \frac{\sigma_w^2}{P_p}(\mathbf{F}^H\mathbf{F})^{-1} + \mathbf{v}\mathbf{v}^H - 2\mathbf{v}\mathbf{v}^H = \frac{\sigma_w^2}{P_p}(\mathbf{F}^H\mathbf{F})^{-1},
\end{aligned} \tag{5.13}$$

which shows that $\hat{\mathbf{v}}$ achieves the CRLB when $\mathbf{F}^H\mathbf{F}$ is full-rank. While this estimator works successfully when the channels of interest do not exhibit any structure, the minimum number of pilots required increases significantly with an increasing number of RIS elements.

CRLB on UE Localization Error

So far, we have derived the FIM between the observation $\mathbf{y}_p$ and the channel coefficients $\mathbf{v}$ when the UE-RIS channels do not exhibit any structure. When these channels have parametric LOS structures, however, they can be expressed in terms of much fewer parameters, as in (5.4), which is quite convenient in terms of reducing the number of pilot transmissions since the number of RIS elements N can be very large in practice. To overcome this, we can exploit our knowledge of the RISs' geometry since each N-dimensional channel can be expressed in terms of three parameters: attenuation, propagation delay, and azimuth angle of arrival While α_k, τ_k, and φ_k seem like independent parameters, they are coupled through the UE position $\mathbf{z} \triangleq \begin{bmatrix} x_t & y_t \end{bmatrix}^T$. While the propagation delays' and azimuth AoAs' relations with the UE are straightforward, we can use the free space path loss

model to relate the attenuation parameters to (x_t, y_t) as follows:

$$\alpha_1 = \left(\frac{c}{4\pi f_c \sqrt{y_t^2 + (x_{\max} - x_t)^2}} \right)^2 \tag{5.14a}$$

$$\alpha_2 = \left(\frac{c}{4\pi f_c \sqrt{y_t^2 + (x_{\max} + x_t)^2}} \right)^2 \tag{5.14b}$$

$$\tau_1 = \frac{\sqrt{y_t^2 + (x_{\max} - x_t)^2}}{c} \tag{5.14c}$$

$$\tau_2 = \frac{\sqrt{y_t^2 + (x_{\max} + x_t)^2}}{c} \tag{5.14d}$$

$$\varphi_1 = \tan^{-1}\left(\frac{y_t}{x_{\max} - x_t} \right) \tag{5.14e}$$

$$\varphi_2 = \tan^{-1}\left(\frac{y_t}{x_{\max} + x_t} \right) \tag{5.14f}$$

By combining (5.4) and (5.14), we can define the following non-linear transformation between the UE coordinates and the channels to be estimated as $\boldsymbol{\beta}(\mathbf{z}) \triangleq \mathbf{v}$.

To obtain the FIM between $\mathbf{Y}_p$ and $\mathbf{z}$, we need to use a well-known result [28, Eq. 3.30]:

$$\mathbf{I}^{-1}(\mathbf{Y}_p; \boldsymbol{\beta}(\mathbf{z})) = \mathbf{J}_{\boldsymbol{\beta}}^H \mathbf{I}^{-1}(\mathbf{Y}_p; \mathbf{z}) \mathbf{J}_{\boldsymbol{\beta}}, \tag{5.15}$$

where $\mathbf{J}_{\boldsymbol{\beta}}$ is the Jacobian of $\boldsymbol{\beta}$ w.r.t. $\mathbf{z}$, which is a $2 \times 2N$ matrix where the ijth entry is $[\mathbf{J}_{\boldsymbol{\beta}}]_{ij} = \frac{\partial \beta_j(\mathbf{z})}{\partial z_i}$. Using the Moore-Penrose pseudoinverse of the Jacobian, one can obtain $\mathbf{I}^{-1}(\mathbf{Y}_p; \mathbf{z})$ as

$$\mathbf{I}^{-1}(\mathbf{Y}_p; \mathbf{z}) = (\mathbf{J}_{\boldsymbol{\beta}} \mathbf{J}_{\boldsymbol{\beta}}^H)^{-1} \mathbf{J}_{\boldsymbol{\beta}} \mathbf{I}^{-1}(\mathbf{Y}_p; \boldsymbol{\beta}(\mathbf{z})) \mathbf{J}_{\boldsymbol{\beta}}^H (\mathbf{J}_{\boldsymbol{\beta}} \mathbf{J}_{\boldsymbol{\beta}}^H)^{-1}. \tag{5.16}$$

To obtain $\mathbf{I}^{-1}(\mathbf{Y}_p; \mathbf{z})$ in closed form, what remains is to obtain $\mathbf{J}_{\boldsymbol{\beta}}$. To this end, we can express $\mathbf{J}_{\boldsymbol{\beta}}$ as a 2×2 block matrix of $1 \times N$ entries:

$$\mathbf{J}_{\boldsymbol{\beta}} = \begin{bmatrix} \frac{\partial \mathbf{g}}{\partial x_t} & \frac{\partial \mathbf{p}}{\partial x_t} \\ \frac{\partial \mathbf{g}}{\partial y_t} & \frac{\partial \mathbf{p}}{\partial y_t} \end{bmatrix} \tag{5.17}$$

By using the chain rule for derivatives on (5.4), we obtain

$$\frac{\partial \mathbf{g}}{\partial x_t} = e^{-j2\pi f_c \tau_1}\left[\frac{1}{2\sqrt{\alpha_1}}\frac{\partial \alpha_1}{\partial x_t}\mathbf{a}(\varphi_1) - j2\pi f_c \frac{\partial \tau_1}{\partial x_t}\sqrt{\alpha_1}\mathbf{a}(\varphi_1) + \sqrt{\alpha_1}\frac{\partial \mathbf{a}(\varphi_1)}{\partial \varphi_1}\frac{\partial \varphi_1}{\partial x_t}\right], \tag{5.18a}$$

$$\frac{\partial \mathbf{p}}{\partial x_t} = e^{-j2\pi f_c \tau_2}\left[\frac{1}{2\sqrt{\alpha_2}}\frac{\partial \alpha_2}{\partial x_t}\mathbf{a}(\varphi_2) - j2\pi f_c \frac{\partial \tau_2}{\partial x_t}\sqrt{\alpha_1}\mathbf{a}(\varphi_2) + \sqrt{\alpha_2}\frac{\partial \mathbf{a}(\varphi_2)}{\partial \varphi_2}\frac{\partial \varphi_2}{\partial x_t}\right], \tag{5.18b}$$

$$\frac{\partial \mathbf{g}}{\partial y_t} = e^{-j2\pi f_c \tau_1}\left[\frac{1}{2\sqrt{\alpha_1}}\frac{\partial \alpha_1}{\partial y_t}\mathbf{a}(\varphi_1) - j2\pi f_c \frac{\partial \tau_1}{\partial y_t}\sqrt{\alpha_1}\mathbf{a}(\varphi_1) + \sqrt{\alpha_1}\frac{\partial \mathbf{a}(\varphi_1)}{\partial \varphi_1}\frac{\partial \varphi_1}{\partial y_t}\right], \tag{5.18c}$$

$$\frac{\partial \mathbf{p}}{\partial y_t} = e^{-j2\pi f_c \tau_2}\left[\frac{1}{2\sqrt{\alpha_2}}\frac{\partial \alpha_2}{\partial y_t}\mathbf{a}(\varphi_2) - j2\pi f_c \frac{\partial \tau_2}{\partial y_t}\sqrt{\alpha_1}\mathbf{a}(\varphi_2) + \sqrt{\alpha_2}\frac{\partial \mathbf{a}(\varphi_2)}{\partial \varphi_2}\frac{\partial \varphi_2}{\partial y_t}\right], \tag{5.18d}$$

In (5.18), the derivatives to be evaluated are $\frac{\partial \mathbf{a}}{\partial \varphi}$, $\frac{\partial \alpha_k}{\partial x_t}, \frac{\partial \alpha_k}{\partial y_t}$, $\frac{\partial \tau_k}{\partial x_t}, \frac{\partial \tau_k}{\partial y_t}$, $\frac{\partial \varphi_k}{\partial x_t}$, and $\frac{\partial \varphi_k}{\partial y_t}$. Using the array steering vector formula and (5.14), we can evaluate these as follows:

$$\frac{\partial \mathbf{a}}{\partial \varphi} = \begin{bmatrix} 0 & \dots & -j2\pi \frac{\Delta}{\lambda}(N-1)\cos(\varphi)e^{-j2\pi \frac{\Delta}{\lambda}(N-1)\sin(\varphi)} \end{bmatrix}^T \tag{5.19a}$$

$$\frac{\partial \alpha_k}{\partial x_t} = \frac{\pm 32\pi^2 f_c^2 c^2 (x_{\max} \mp x_t)}{\left[16\pi^2 f_c^2 (x_{\max} \mp x_t)^2 + 16\pi^2 f_c^2 y_t^2\right]^2} \tag{5.19b}$$

$$\frac{\partial \alpha_k}{\partial y_t} = \frac{-32\pi^2 f_c^2 c^2 y_t}{\left[16\pi^2 f_c^2 (x_{\max} \mp x_t)^2 + 16\pi^2 f_c^2 y_t^2\right]^2} \tag{5.19c}$$

$$\frac{\partial \tau_k}{\partial x_t} = \frac{\mp (x_{\max} \mp x_t)}{c\sqrt{(x_{\max} \mp x_t)^2 + y_t^2}} \tag{5.19d}$$

$$\frac{\partial \tau_k}{\partial y_t} = \frac{y_t}{c\sqrt{(x_{\max} \mp x_t)^2 + y_t^2}} \tag{5.19e}$$

$$\frac{\partial \varphi_k}{\partial x_t} = \frac{\mp y_t^2}{y_t^2 + (x_{\max} \mp x_t)^2} \tag{5.19f}$$

$$\frac{\partial \varphi_k}{\partial y_t} = \frac{(x_{\max} \mp x_t)}{y_t^2 + (x_{\max} \mp x_t)^2} \tag{5.19g}$$

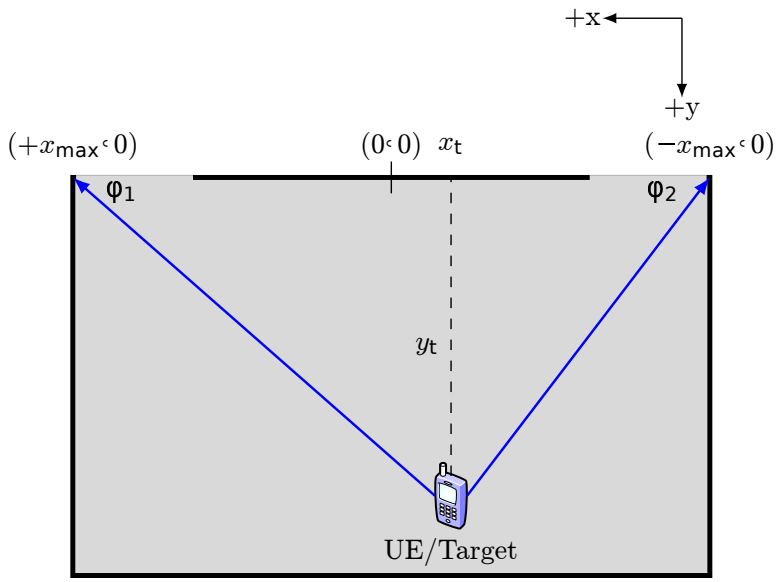

Figure 5.2: The geometrical relationship between the azimuth AoAs and the cartesian coordinates.

As a result, we obtain the Jacobian in closed form and therefore have $\mathbf{I}^{-1}(\mathbf{Y}_p; \mathbf{z})$. The diagonal entries of this matrix provide a lower bound on the squared error in estimating x_t and y_t. To obtain the localization error bound (LEB) in meters, we just have to calculate the 2-norm of the resulting error vector. Consequently, the LEB becomes

$$\text{LEB} = \sqrt{\text{tr}(\mathbf{I}^{-1}(\mathbf{Y}_p; \mathbf{z}))}. \tag{5.20}$$

CRLB on Channel Estimation MSE

The inverse FIM between $\mathbf{Y}_p$ and the cartesian coordinates of the UE we derived using the channel geometry provides the goldens standard for any unbiased location estimator. Using a similar idea, we can obtain a lower bound on the performance of unbiased parametric channel estimators by using the non-linear transformation $\mathbf{v} = \boldsymbol{\beta}(\mathbf{z})$, similar to the parametric estimation idea in [17]. While we do not derive any parametric estimators in this letter, we provide the CRLB as an indicator of what is achievable if a parametric channel estimator were to be designed for such a system. To determine the CRLB on parametric channel estimation MSE, using (5.15) suffices, that is:

$$\text{Cov}(\boldsymbol{\beta}(\hat{\mathbf{z}})) \succeq \mathbf{J}_{\boldsymbol{\beta}}^{H} \mathbf{I}^{-1}(\mathbf{Y}_p; \mathbf{z}) \mathbf{J}_{\boldsymbol{\beta}}. \tag{5.21}$$

Parameter	Value
P_p	50 dBm
σ_w^2	-104 dBm
f_c	30 GHz
M	64
N	16
L	16, 32
$x_{\max}$	20 m
$y_{\max}$	40 m

Table 5.1: System parameters used for the numerical results. The value for σ_w^2 is obtained by considering a 10 MHz transmission bandwidth and a noise power spectral density of -174dBm/Hz. In addition, the BS is located at $(10, -40)$ according to the coordinate system provided in Fig. 5.2.

5.4 Numerical Results

In this section, we provide numerical examples for the analysis we have provided. To this end, we consider the set of system parameters in Table 5.1. To capture large-scale effects, we consider the free space path loss model. Fig. 5.3 and 5.4 show the normalized channel estimation CRLB, that is, we normalize the traces of the CRLBs in (5.12) and (5.21), respectively, by $\|\mathbf{v}\|_2^2 = 2N$. Note that parametric estimation vastly outperforms the non-parametric estimation. Although the non-parametric estimation uses twice as many pilots as the parametric estimation, the knowledge of the channel structure in parametric estimation significantly reduces the number of unknown parameters and boosts the channel estimation performance by three orders of magnitude. Non-parametric channel estimation also yields very high MSE due to the high carrier frequency and severe path loss.

In Fig. 5.5, we plot the LEB (in meters) throughout the room, as provided by (5.20). Note that for a large part of the surface of the room, the localization accuracy is at the sub-decimeter level. However, the significant inaccuracy at around $y_t = 0$ must be noted. In this region, both RISs receive the UE's signal almost perpendicularly, and hence the observation is not so sensitive to the exact position of the UE, resulting in low Fisher information. Even in this region, the accuracy is between meter and decimeter levels.

5.5 Conclusion

In this letter, we investigated the use of RISs for an integrated communication and localization system in an indoor environment. We proposed a setup with a single-antenna UE and an M-antenna BS between which pure LOS links are maintained via two N-element RISs. By exploiting the channel and indoor geometries, we showed that it is possible to use the same pilot signals to estimate

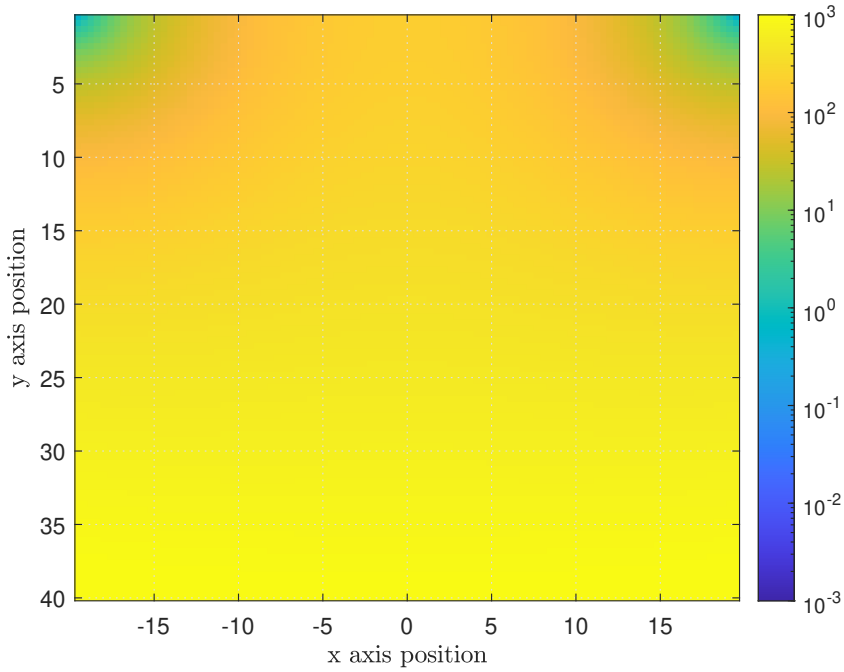

Figure 5.3: Non-parametric channel estimation MSE for $\mathbf{B}_1^H\mathbf{B}_2 = \mathbf{0}$. Note that we transmit $L = 2N$ pilots for non-parametric estimation as opposed to $L = N$ pilots for parametric estimation.

the position of the UE, and the UE-RIS channels. As the performance metric, we used the CRLB, the lower bound on the MSE of any unbiased estimator. Through numerical examples, we showed that it is feasible to use two RISs to locate an indoor user and utilize the location information to estimate the unknown channels. Considering the parametric structures of LOS channels not only brings the benefits of reducing the pilot transmission overhead, but also improves the channel estimation performance by multiple orders of magnitude and hence acts as a precursor to a plethora of possibilities in localization-aided channel estimation to develop more pilot-efficient systems. In this letter, we considered the estimation of pure-LOS channels exploiting the channel structure, which is quite significant due to the more structured nature of mmWave channels compared to the channels with μ-wave frequencies [75]. While our analysis is extendable to scenarios with a direct UE-BS path, we considered a setup where the direct path is blocked in this work, which is realistic at mmWave/THz frequencies due to high penetration losses. Although we ignored the presence of scattering clusters, the analysis provided in this paper is extendable to clustered channel models,

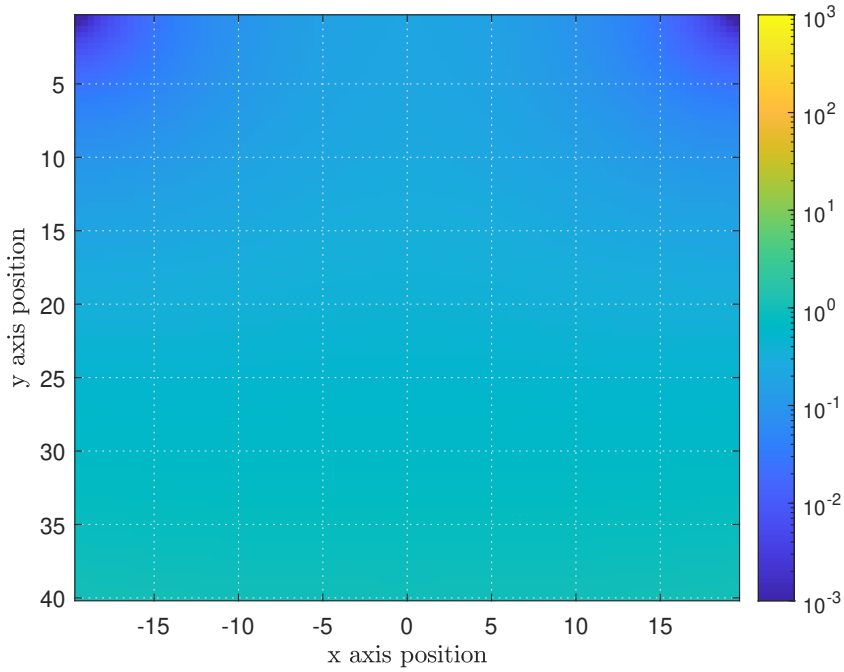

Figure 5.4: CRLB on the parametric channel estimation MSE for $\mathbf{B}_1 = \mathbf{B}_2$. Note that the channel estimation MSE is decreased by three orders of magnitude compared to Fig. 5.3 although half as many pilots are used.

which will be investigated in future work.

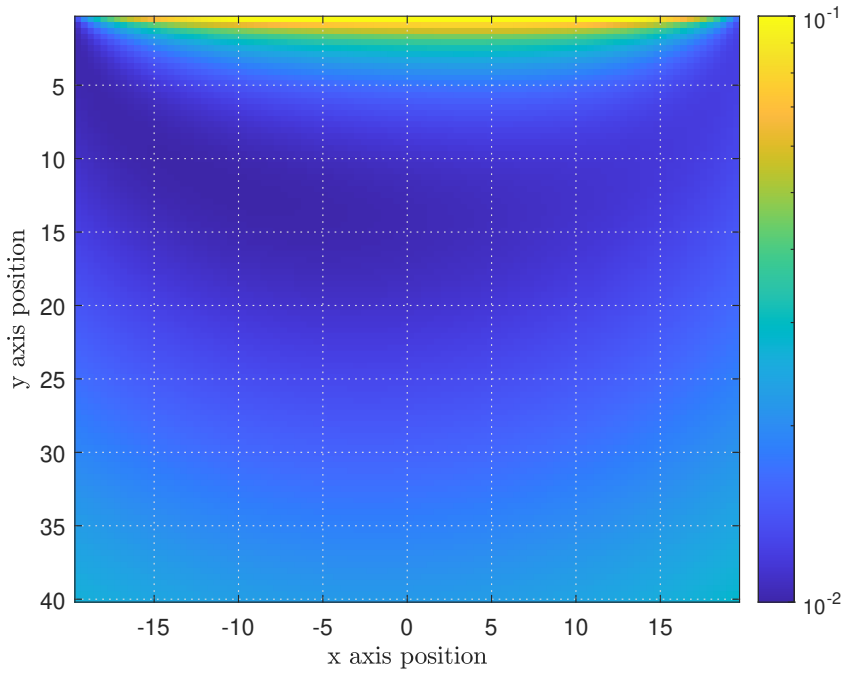

Figure 5.5: CRLB on UE localization in meters. Note that the figure indicates sub-decimeter localization accuracy for the entire area, and almost centimeter-level localization accuracy around where the localization geometry is the most favorable.

Chapter 6

Performance Analysis of a 2D-MUSIC Algorithm for Parametric Near-Field Channel Estimation

Abstract

In this letter, we address parametric channel estimation in a multi-user multiple-input multiple-output system within the radiative near-field of the base station array with aperture antennas. We consider a two-dimensional multiple signal classification algorithm (2D-MUSIC) to estimate both the range and azimuth angles of arrival for the users' channels, utilizing parametric radiative near-field channel models. We analyze the performance of the algorithm by deriving the Cramér-Rao bound (CRB) for parametric estimation, and its effectiveness is compared against the least squares estimator, which is a non-parametric estimator. Numerical results indicate that the 2D-MUSIC algorithm outperforms the least squares estimator. Furthermore, the results demonstrate that the performance of 2D-MUSIC achieves the parametric channel estimation CRB, which shows that the algorithm is asymptotically consistent.

6.1 Introduction

The success of massive multiple-input multiple-output (M-MIMO) implementation in 5G systems, across both sub-6 GHz and mmWave bands, suggests that the next generation of wireless systems will likely exploit even larger arrays, referred to as the extremely large aperture array (ELAA) [76–78]. Moreover, there is an ongoing trend toward employing higher frequencies, implying a smaller wavelength in wireless systems [79,80]. As the array size increases and the wavelength

shrinks, the Fraunhofer array distance, the boundary between radiative near- and far-fields, becomes large. Consequently, the UEs are likely to fall into the radiative near-field region of the ELAA [14, 81]. In the radiative near-field, the spherical curvature of the wavefront is noticeable; therefore, there are spherical phase variations between the antenna elements in the ELAA. The phase variations must be characterized by both the angle and distance between the ELAA and the transmitter. This renders far-field channel models inaccurate as the far-field array response does not capture information about the propagation distance.

To address this issue, polar-domain representation for the extremely large-scale MIMO (XL-MIMO) channel has been proposed in [82, 83]. Reference [82] focuses on the recovery of the angular and distance information in the near-field channel utilizing the sparsity in the polar domain, while [83] utilizes the distance domain in addition to the angular domain to multiplex UEs in LOS scenarios. With the polar-domain representation, one can sample both the angular and distance domains to obtain a near-field codebook. Moreover, the polar-domain representation is used to ensure a sparsity representation of the near-field channel, enabling the utilization of compressive sensing methods such as the classical and algorithms [82].

When the channel is pure-LOS, another way to estimate the near-field channel is to first estimate the parameters of the UEs' locations, given that the channel has a simple and known parametrization. Subsequently, the parameters are substituted into the channel parametric model to yield the channel estimate. The state-of-the-art [14] focuses on developing a low complexity algorithm to estimate the parameters of the UE' locations by performing subsequential parameter estimations neglecting the correlation between the parameters. However, this introduces notable peformance degradation. Furthermore, there is no theoretical bound that is derived to guarantee the performance of the estimator.

In this letter, we explore the possibility of estimating the UEs' locations in polar coordinates based on the 2D near-field channel model, where the channel is assumed to be pure-LOS. Then, we use the parameter estimates to infer the channel coefficients. More importantly, we derive the CRB on the parametric channel estimation MSE to evaluate the performance of the 2D-MUSIC estimator. The CRB provides a lower bound on the variance of any unbiased estimator [12], and depends heavily on the relationship between the observation and the parameter. Therefore, it is useful in evaluating parametric estimators. In [84], the CRB on parametric channel estimation is derived with a far-field model for a system using two reconfigurable intelligent surfaces by considering the non-parametric CRB as a transitional step towards a parametric channel estimation CRB. To the best of the authors' knowledge, however, such an analysis has not been used to evaluate the performance of parametric channel estimators. In this letter, we explore the opportunities of parametric channel estimation in near-field channels with aperture antennas by performing the aforementioned analysis. In addition to the CRB analysis, we also compare the performance of the 2D-MUSIC algorithm with a non-parametric estimator, namely, the least

squares (LS) estimator to observe the performance gain from parametric channel estimation.

6.2 System Model

We consider a BS equipped with a ULA consisting of N aperture antennas, serving K single-antenna UEs. The location of UE k is denoted as $(x_k, 0, z_k)$, which is assumed to be in the radiative near-field region (Fresnel region) of the BS array, for $k \in \{1, \ldots, K\}$. Without loss of generality, we let the BS be geometrically arranged along the x-axis with half-wavelength spacing, and the array is centered around $(0, 0, 0)$. Antenna element n is centered at $(\bar{x}_n, 0, 0)$ with

$$\bar{x}_n = \underbrace{\left(n - \frac{N+1}{2}\right)}_{\delta_n} \underbrace{\frac{\lambda}{2}}_{\Delta}, \tag{6.1}$$

where δ_n and Δ are the index of antenna element n and spacing between two antenna elements, respectively. The aperture antennas each have an area of Δ^2 along the xy-plane.

The channel between antenna element n and UE k located at the distance d_k (from the origin) in the azimuth angle φ_k with respect to the origin (measured from x-axis towards the z-axis) is represented as

$$h_n^k(d_k, \varphi_k) = \sqrt{\beta_{n,k}} e^{-j\frac{2\pi}{\lambda} r_n^k}, \tag{6.2}$$

where $r_n^k = \sqrt{d_k^2 + (\delta_n \Delta)^2 - 2 d_k \Delta \delta_n \cos(\varphi_k)}$. The free-space channel gain between antenna n and UE k ($\beta_{n,k}$) can be approximated as [85]

$$\beta_{n,k} \approx \beta_k = \frac{\lambda^2}{16\pi} \frac{\sin(\varphi_k)}{d_k^2} \tag{6.3}$$

which accounts for the angle-dependent effective antenna area of the transmitter. The approximation holds when the propagation distance is larger than twice the array aperture [81] so that the spherical amplitude variations over the wavefront are negligible but not the phase variations. Using (6.2) and (6.3), we can model the near-field channel vector to UE k as

$$\mathbf{h}_k(d_k, \varphi_k) = \sqrt{\beta_k} \left[e^{-j\frac{2\pi}{\lambda} r_1^k} \ \ldots \ e^{-j\frac{2\pi}{\lambda} r_N^k} \right]^T. \tag{6.4}$$

At time instance l, the received signal can be written as

$$\mathbf{y}[l] = \mathbf{H}\mathbf{s}[l] + \mathbf{w}[l], \quad l = 1, \ldots, L, \tag{6.5}$$

where $\mathbf{H} = [\mathbf{h}_1(d_1, \varphi_1) \ \ldots \ \mathbf{h}_K(d_K, \varphi_K)]$, $\mathbf{y}[l] = [y_1[l] \ \ldots \ y_N[l]]^T$ contains the received signals, $\mathbf{s}[l] = [s_1[l] \ \ldots \ s_K[l]]^T$ represents the transmitted signals from K UEs, and $\mathbf{w}[l] = [w_1[l] \ \ldots \ w_N[l]]^T$ is the additive noise where each entry follows an independent complex Gaussian distribution with zero mean and variance σ^2.

6.3 Near-Field Parametric Channel Estimation via 2D-MUSIC

In this section, our aim is to estimate the channels $\mathbf{h}_k(d_k, \varphi_k)$ for $k = 1, \ldots, K$ based on (6.5). Combining L such observations over time, we first aim to estimate the ranges d_k and azimuth AoAs φ_k for $k = 1, \ldots, K$ using the 2D-MUSIC algorithm. The channel response function, defined in (6.2), allows us to characterize the UEs' channels by estimating the locations $(d_k, \varphi_k), k = 1, \ldots, K$, from L transmissions at distinct instants. This allows us to estimate the channels of the K UEs based on the d_k and φ_k by using the parametric model in (6.4). In the following, we provide a way to utilize 2D-MUSIC to estimate the UEs' channels. We assume that: 1) The UEs are not located in exactly the same angular directions. 2) The transmitted signals are assumed to follow a circular symmetric complex Gaussian distribution. 3) The noise is independent of all the signals.

The MUSIC algorithm works by exploiting the structure of the eigenvectors in the sample covariance matrix [11]:

$$\widehat{\mathbf{R}}_L = \frac{1}{L} \sum_{l=1}^{L} \mathbf{y}[l]\mathbf{y}^H[l]. \tag{6.6}$$

Given the number of UEs K, we first construct the noise-subspace matrix $\widehat{\mathbf{U}}_n \in \mathbb{C}^{N \times (N-K)}$ whose columns are the eigenvectors of $\widehat{\mathbf{R}}_L$ corresponding to the smallest $(N - K)$ eigenvalues. Then, the 2D MUSIC spectrum is generated as

$$S(d, \varphi) = \frac{1}{\mathbf{h}^H(d, \varphi)\widehat{\mathbf{U}}_n \widehat{\mathbf{U}}_n^H \mathbf{h}(d, \varphi)}, \tag{6.7}$$

where each possible value of $\mathbf{h}(d, \varphi)$ is obtained by computing the potential channel responses by plugging the grid points into (6.4). K combinations of (d, φ) corresponding to the peaks in the MUSIC spectrum are then identified, each representing a UE's location. The channel estimate $\hat{\mathbf{H}}$ can then be obtained by substituting the parameter estimates $(d_k, \varphi_k), k = 1, \ldots, K$ into (6.2).

6.4 CRB on Near-Field Parametric Channel Estimation

In parameter estimation problems, bounds on estimation performance serve as the golden standard to evaluate the performance of estimators. To this end, we derive the CRB on the near-field parametric channel estimation in this section. The CRB, the inverse of the FIM, provides a lower bound on the performance of any unbiased estimator [12] via the following matrix inequality:

$$\mathrm{Cov}\left(\hat{\boldsymbol{\theta}}(\mathbf{X})\right) \succeq \mathbf{I}^{-1}(\mathbf{X}; \boldsymbol{\theta}) \tag{6.8}$$

for an estimate of a parameter vector $\boldsymbol{\theta}$ based on an observation vector $\mathbf{X}$. Here, $\mathrm{Cov}(\hat{\boldsymbol{\theta}}(\mathbf{X})) = \mathbb{E}[(\hat{\boldsymbol{\theta}}(\mathbf{X}) - \boldsymbol{\theta})(\hat{\boldsymbol{\theta}}(\mathbf{X}) - \boldsymbol{\theta})^H]$ is the covariance matrix and, consequently, the bound on the sum MSE can be expressed as

$$\mathbb{E}\left[\left\|\hat{\boldsymbol{\theta}}(\mathbf{X}) - \boldsymbol{\theta}\right\|^2\right] \geq \mathrm{tr}\left(\mathbf{I}^{-1}(\mathbf{X};\boldsymbol{\theta})\right). \tag{6.9}$$

In a generic vector parameter estimation problem, the FIM is computed via the following equation [28, Eq. 3.21]:

$$[\mathbf{I}(\mathbf{X};\boldsymbol{\theta})]_{i,j} = -\mathbb{E}\left[\frac{\partial^2 \ln(f(\mathbf{X};\boldsymbol{\theta}))}{\partial\theta_i \partial\theta_j}\right], \tag{6.10}$$

where θ_i is the i-th element of $\boldsymbol{\theta}$. In our near-field parametric channel estimation problem, the observation from a single transmission is stated in (6.5). Before ensembling the observations from multiple transmissions, it is more convenient to change the order of the transmitted signals and the unknown channel in (6.5) as

$$\mathbf{y}[l] = \underbrace{\begin{bmatrix} s_1[l]\mathbf{I}_N & \dots & s_K[l]\mathbf{I}_N \end{bmatrix}}_{\triangleq \mathbf{S}[l] \in \mathbb{C}^{N \times NK}} \underbrace{\begin{bmatrix} \mathbf{h}_1(d_1,\varphi_1) \\ \vdots \\ \mathbf{h}_K(d_K,\varphi_K) \end{bmatrix}}_{\triangleq \tilde{\mathbf{h}}(\boldsymbol{\theta}) \in \mathbb{C}^{NK \times 1}} + \mathbf{w}[l], \tag{6.11}$$

where $\boldsymbol{\theta} \triangleq [d_1 \ \dots \ d_K \ \varphi_1 \ \dots \ \varphi_K]^T \in \mathbb{R}^{2K}$. While (6.11) corresponds to the observation from a single transmission, we can stack the observations from multiple transmissions $l = 1, \dots, L$ vertically to obtain

$$\tilde{\mathbf{y}} = \mathbf{S}\tilde{\mathbf{h}}(\boldsymbol{\theta}) + \tilde{\mathbf{w}} \in \mathbb{C}^{LN \times 1}, \tag{6.12}$$

where $\tilde{\mathbf{y}} \triangleq [\mathbf{y}^T[1] \ \dots \ \mathbf{y}^T[L]]^T \in \mathbb{C}^{LN}$, $\mathbf{S} \triangleq [\mathbf{S}^T[1] \ \dots \ \mathbf{S}^T[L]]^T \in \mathbb{C}^{LN \times NK}$, and $\tilde{\mathbf{w}} \triangleq [\mathbf{w}^T[1] \ \dots \ \mathbf{w}^T[L]]^T \in \mathbb{C}^{LN}$. To compute the FIM, we first define a transition parameter $\mathbf{v} \triangleq \tilde{\mathbf{h}}(\boldsymbol{\theta})$, for which we can express the FIM as

$$\mathbf{I}(\tilde{\mathbf{y}};\mathbf{v}) = \mathbf{S}^H \boldsymbol{\Sigma}_{\tilde{\mathbf{w}}}^{-1} \mathbf{S}, \tag{6.13}$$

where $\boldsymbol{\Sigma}_{\tilde{\mathbf{w}}} = \mathbb{E}[\tilde{\mathbf{w}}\tilde{\mathbf{w}}^H] \in \mathbb{C}^{LN \times LN}$ is the noise covariance matrix, which has the following relationship with the noise covariance for a single transmission $\boldsymbol{\Sigma}_{\mathbf{w}} = \mathbb{E}[\mathbf{w}\mathbf{w}^H] \in \mathbb{C}^{N \times N}$:

$$\boldsymbol{\Sigma}_{\tilde{\mathbf{w}}} = \mathbf{I}_L \otimes \boldsymbol{\Sigma}_{\mathbf{w}} = \sigma^2 \mathbf{I}_{LN}. \tag{6.14}$$

This relation holds since the noise is independent over both time and antennas.

CRB for Vector Transformations

To incorporate the parametric nature of the channel into the CRB analysis, we consider the parametric model $\tilde{\mathbf{h}}(\cdot) : \mathbb{R}^{2K} \mapsto \mathbb{C}^{NK}$ as a vector transformation to utilize the following identity [28, Eq. 3.30]:

$$\mathbf{I}^{-1}(\tilde{\mathbf{y}};\mathbf{v}) = \mathbf{J}_{\tilde{\mathbf{h}}}^H \mathbf{I}^{-1}(\tilde{\mathbf{y}};\boldsymbol{\theta}) \mathbf{J}_{\tilde{\mathbf{h}}}, \tag{6.15}$$

where $\mathbf{J}_{\tilde{\mathbf{h}}} \in \mathbb{C}^{2K \times NK}$ is the Jacobian of the non-linear transformation $\tilde{\mathbf{h}} : \mathbb{R}^{2K} \mapsto \mathbb{C}^{NK}$ with entries $[\mathbf{J}_{\tilde{\mathbf{h}}}]_{i,j} = \frac{\partial \tilde{\mathbf{h}}_j}{\partial \theta_i}$. While (6.15) suffices to obtain the inverse FIM between the observation and the location parameters, the non-parametric FIM in (6.13) is not always invertible. Therefore, it is more desirable to have an expression for $\mathbf{I}(\tilde{\mathbf{y}}; \boldsymbol{\theta})$ in terms of $\mathbf{I}(\tilde{\mathbf{y}}; \mathbf{v})$. To this end, we multiply (6.15) with the pseudoinverse of $\mathbf{J}_{\tilde{\mathbf{h}}}$ from both sides to obtain

$$\mathbf{I}^{-1}(\tilde{\mathbf{y}}; \mathbf{v}) = \mathbf{J}_{\tilde{\mathbf{h}}}^H \mathbf{I}^{-1}(\tilde{\mathbf{y}}; \boldsymbol{\theta}) \mathbf{J}_{\tilde{\mathbf{h}}} \Rightarrow \mathbf{J}_{\tilde{\mathbf{h}}} \mathbf{I}(\tilde{\mathbf{y}}; \mathbf{v}) \mathbf{J}_{\tilde{\mathbf{h}}}^H = \mathbf{I}(\tilde{\mathbf{y}}; \boldsymbol{\theta}). \tag{6.16}$$

Combining (6.13) and (6.16) yields the $2K \times 2K$ FIM between the received signals and the UEs' coordinates. To obtain the parametric channel estimation CRB, we invert $\mathbf{I}(\tilde{\mathbf{y}}; \boldsymbol{\theta})$ and apply (6.15):

$$\mathbf{I}^{-1}(\tilde{\mathbf{y}}; \tilde{\mathbf{h}}(\boldsymbol{\theta})) = \mathbf{J}_{\tilde{\mathbf{h}}}^H \mathbf{I}^{-1}(\tilde{\mathbf{y}}; \boldsymbol{\theta}) \mathbf{J}_{\tilde{\mathbf{h}}}. \tag{6.17}$$

Jacobian of the Parametric Channel

To obtain the CRB on the MSE of any parametric estimator for our setup, what remains is to derive the Jacobian of $\tilde{\mathbf{h}}(\cdot)$ in closed form. Based on the definition of $\tilde{\mathbf{h}}$ in (6.11), the Jacobian can be obtained as $\mathbf{J}_{\tilde{\mathbf{h}}} = [\mathbf{J}_1^T, \mathbf{J}_2^T]^T$ where $\mathbf{J}_1, \mathbf{J}_2 \in \mathbb{C}^{K \times NK}$ are block diagonal matrices containing the partial derivatives of the channel with respect to d_k and φ_k, respectively. That is, $\mathbf{J}_1 = \text{diag}\left(\frac{\partial \mathbf{h}_1^T}{\partial d_1}, \ldots, \frac{\partial \mathbf{h}_K^T}{\partial d_K}\right)$ and $\mathbf{J}_2 = \text{diag}\left(\frac{\partial \mathbf{h}_1^T}{\partial \varphi_1}, \ldots, \frac{\partial \mathbf{h}_K^T}{\partial \varphi_K}\right)$. To derive $\frac{\partial \mathbf{h}_k}{\partial d_k}$ and $\frac{\partial \mathbf{h}_k}{\partial \varphi_k}$, we need to recall the near-field channel model parametrized by UE location in Section 6.2. Starting from (6.4), we have

$$\begin{aligned}
\frac{\partial \mathbf{h}_k}{\partial d_k} &= \frac{1}{2\sqrt{\beta_k}} \frac{\partial \beta_k}{\partial d_k} \left[e^{-j\frac{2\pi}{\lambda} r_1^k} \quad \ldots \quad e^{-j\frac{2\pi}{\lambda} r_N^k} \right]^T \\
&+ \sqrt{\beta_k} \left[-j\frac{2\pi}{\lambda} \frac{\partial r_1^k}{\partial d_k} e^{-j\frac{2\pi}{\lambda} r_1^k} \quad \ldots \quad -j\frac{2\pi}{\lambda} \frac{\partial r_N^k}{\partial d_k} e^{-j\frac{2\pi}{\lambda} r_N^k} \right]^T, \qquad (6.18a) \\
\frac{\partial \mathbf{h}_k}{\partial \varphi_k} &= \frac{1}{2\sqrt{\beta_k}} \frac{\partial \beta_k}{\partial \varphi_k} \left[e^{-j\frac{2\pi}{\lambda} r_1^k} \quad \ldots \quad e^{-j\frac{2\pi}{\lambda} r_N^k} \right]^T \\
&+ \sqrt{\beta_k} \left[-j\frac{2\pi}{\lambda} \frac{\partial r_1^k}{\partial \varphi_k} e^{-j\frac{2\pi}{\lambda} r_1^k} \quad \ldots \quad -j\frac{2\pi}{\lambda} \frac{\partial r_N^k}{\partial \varphi_k} e^{-j\frac{2\pi}{\lambda} r_N^k} \right]^T, \qquad (6.18b)
\end{aligned}$$

where $\frac{\partial \beta_k}{\partial d_k}$, $\frac{\partial \beta_k}{\partial \varphi_k}$, $\frac{\partial r_n^k}{\partial d_k}$, and $\frac{\partial r_n^k}{\partial \varphi_k}$ can be expressed as

$$\frac{\partial \beta_k}{\partial d_k} = -\frac{\lambda^2}{8\pi} \frac{\sin(\varphi_k)}{d_k^3}, \tag{6.19a}$$

$$\frac{\partial \beta_k}{\partial \varphi_k} = \frac{\lambda^2}{16\pi} \frac{\cos(\varphi_k)}{d_k^2}, \tag{6.19b}$$

$$\frac{\partial r_n^k}{\partial d_k} = \frac{d_k - \Delta\delta_n \cos(\varphi_k)}{\sqrt{d_k^2 + (\delta_n \Delta)^2 - 2 d_k \Delta \delta_n \cos(\varphi_k)}}, \tag{6.19c}$$

$$\frac{\partial r_n^k}{\partial \varphi_k} = \frac{d_k \Delta \delta_n \sin(\varphi_k)}{\sqrt{d_k^2 + (\delta_n \Delta)^2 - 2 d_k \Delta \delta_n \cos(\varphi_k)}}. \tag{6.19d}$$

As a result, we have $\mathbf{J}_{\tilde{\mathbf{h}}}$ and hence the CRB for parametric channel estimation in closed form.

6.5 Numerical Results

In this section, we provide numerical examples to demonstrate the performance of the 2D-MUSIC algorithm. In addition, we include a non-parametric channel estimator, namely, the LS estimator. Note that one disadvantage of the LS estimator is that it requires a known sequence of pilots while the 2D-MUSIC method does not. For both estimators, we use the CRB as the benchmark. Specifically, for the LS estimator, we use the non-parametric CRB (inverse of (6.13)) and for 2D-MUSIC, we use the parametric CRB we derived in Section 6.4. In addition, we examine the impact of the location of the UE on the channel estimation performance by considering a two-UE setup, assigning one of the UEs a fixed location, and changing the location of the other UE. We provide the parameters used to generate the numerical results in Table 6.1.

Performance of the 2D-MUSIC Algorithm

We first compare the estimation performance for the 2D-MUSIC algorithm and the LS estimator. As shown in Table 6.1, we consider the transmit SNR (P_p/σ^2) to be within the range of -10 dB and 60 dB. The UEs are dropped by selecting uniformly spaced points over the angular domain between 60° and 120°, and between twice the aperture size and the Fraunhofer array distance to ensure radiating near-field conditions. In Fig. 6.1, we provide the CRBs on the channel estimation NMSE for parametric and non-parametric estimators in blue and black solid lines, respectively. Then, we provide the NMSEs achieved by the 2D-MUSIC algorithm and the LS estimator with green and red lines.

The parameter undergoes a known linear transformation when considering the system model non-parametrically. Then, it is corrupted by additive Gaussian noise with known statistics. Therefore, the LS estimator achieves the CRB

Table 6.1: List of parameters used to generate the numerical results.

Parameter	Value
N	32
L	40
K	4 in Fig. 6.1, 2 in Fig. 6.2
SNR	$-10, 0, \ldots, 60$ dB
λ	10 cm

exactly. On the other hand, the 2D-MUSIC algorithm performs worse than the parametric CRB at low SNR, where the algorithm performance is noise-limited. When the SNR is higher than 20 dB, however, the 2D-MUSIC algorithm performance achieves the parametric CRB, showing that the MUSIC algorithm is asymptotically consistent. In addition, note that 2D-MUSIC consistently outperforms LS at all SNRs.

Location Dependence of the CRB

We will now demonstrate how the parametric CRB changes based on the UE location. To this end, we consider $K = 2$ UEs and fix the SNR to 40 dB. In addition, we fix the location of UE 1, denoted by the red dot in Fig. 6.2. Then, we compute the CRB on the parametric channel estimation NMSE for UE 2 over a rectangular region, as shown in Fig. 6.2, where the color bar shows the CRB value. While the antenna array is located at the origin, we choose our rectangular region so all the points are further than twice the aperture size and closer than the Fraunhofer distance to the antenna array.

Note that the CRB increases as the UE moves towards the sides of the region and as the distance increases. On the other hand, the performance is not affected by UE 2's proximity to UE 1. This is because the system has enough observations and spatial degrees of freedom to accurately resolve the two UEs.

6.6 Conclusions

In this letter, we considered the parametric channel estimation problem, where the UEs are within the radiative near field of the BS array. We used the 2D-MUSIC algorithm, which estimates the range and azimuth AoAs of the UEs' channels, and obtained the channel estimates using the parametric near field channel models for aperture antennas. To evaluate the channel estimation performance of 2D-MUSIC, we derived the CRB of parametric channel estimation in closed form and compared the 2D-MUSIC algorithm with a non-parametric estimator, namely the LS estimator. Our numerical results showed that 2D-MUSIC outperforms the LS estimator, and achieves the parametric channel estimation CRB outside the noise-limited region. In addition, we also demonstrated that the 2D-MUSIC algorithm performance is close to the CRB and hence is an efficient method to estimate the channel parametrically.

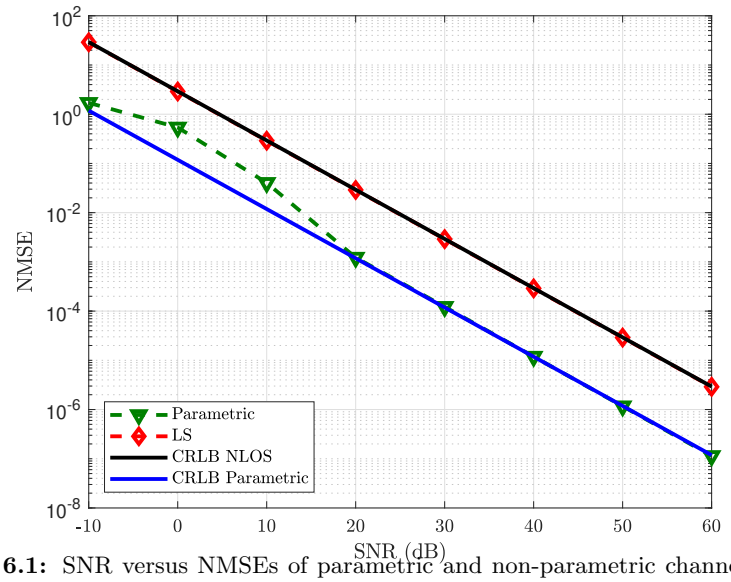

Figure 6.1: SNR versus NMSEs of parametric and non-parametric channel estimation along with parametric and non-parametric CRBs, for the parameters specified in Table 6.1.

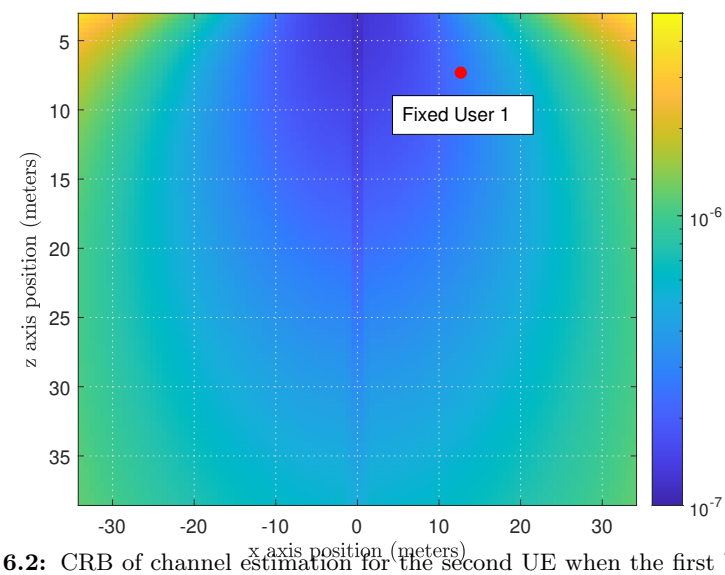

Figure 6.2: CRB of channel estimation for the second UE when the first UE's location is fixed. The SNR is fixed at 40 dB.

Chapter 7

Conclusions and Future Work

7.1 Conclusions

In this thesis, we have covered multiple topics related to the signal processing aspects of RIS-aided wireless communication systems. The main focuses of this thesis were the newly discovered inter-operator pilot contamination and parametric channel estimation. In Chapters 2, 3, and 4, we have covered the first topic. In Chapters 5 and 6, we have covered the second topic. We have shown that both research directions are significant for using RISs in wireless communication systems.

In the first three articles, we have investigated a new kind of pilot contamination effect occurring when multiple RISs are deployed in close proximity. As opposed to multiple UEs using the same pilot sequences contaminating each others' signal in traditional pilot contamination, in multi-RIS pilot contamination, the UE contaminates its own pilot by transmitting over multiple RISs using the same sequence of pilot RIS configurations, essentially creating a virtual twin of the transmitting UE using the same pilot sequence and transmitting over the same RIS. Since there is only a single transmitting UE, it is impossible to resolve the multi-RIS pilot contamination via pilot signal design. Instead, the sequences of RIS configurations should be designed such that the individual paths can be resolved at the BS. To this end, we proposed the orthogonalization of the sequences of RIS configurations during channel estimation, which doubled the channel estimation overhead, which already has a linear complexity in the number of RIS elements. When the BS has a single antenna, it is not possible to mitigate this effect without relying on specific channel structures.

In Chapters 2 and 3, we have analytically characterized the impact of inter-operator pilot contamination in RIS-aided wireless systems. However, the analysis was limited to the case when the BS has a single antenna. As modern wireless communication systems use multiple antennas due to the evolution of MIMO technology, we extended our analysis to systems with multiple BS antennas in

Chapter 4. With the addition of multiple antennas to the system, we also gained an additional tool: receive beamforming. Receive beamforming gave us the capability of obtaining different gains from different channels, and we proposed using this capability to overcome inter-operator pilot contamination. We considered a baseline scheme along with two alternative schemes to overcome inter-operator pilot contamination. First, we considered a scheme that uses MRC to focus the receiver array towards the intended channel to boost the received signal power. In this scheme, the RIS configurations were orthogonalized to overcome inter-operator pilot contamination at the expense of doubling the number of pilots. In the second scheme, we considered using null forming towards the channel between the other operator's RIS and the BS, the main source of inter-operator pilot contamination. In this approach, the RIS configurations were not orthogonalized and hence fewer pilots were used. We also considered a baseline scheme that does not combat inter-operator pilot contamination in any way. Our analysis has shown that nulling the interfering channel results in superior spectral efficiency. While null forming in the second scheme stole some power from the main beam, it used half as many pilots as the first scheme and hence beat the first scheme and the baseline scheme by a good margin. Consequently, our findings lead us to the conclusion that the best way to eliminate inter-operator pilot contamination is by receive beamforming.

In Chapter 5, we have addressed the use of parametric channel models to estimate channels in RIS-aided communication systems. Due to the presence of RISs, the number of channel components to be estimated increases multiplicative with increasing number of RIS elements. Consequently, the pilot transmission requirements for systems with massive RISs become unmanageable and hence impractical. To mitigate this effect, we considered modeling the channels of interest parametrically when LOS conditions exist. In Chapter 5, we considered a two-RIS system with a far-field UE and modeled the UE-RIS channels depending on the UE location. This reduced the number of unknown parameters, and hence the minimum number of pilots to estimate the channel. In Chapter 5, we analytically derive the CRLB on the estimation of location parameters and the channel, and consequently show that parametrization not only provides the capability of estimating the UE location but also boosts the channel estimation performance.

In Chapter 6, we considered an XL-MIMO system consisting of a single BS with a large antenna array and multiple UEs located within the radiative near field of the BS antenna. Using parametric near-field channel models, we estimated the distances and the azimuth angles of the UEs using the 2D-MUSIC algorithm. We also derived the CRLB for near-field MU-MIMO with aperture antennas. We showed that the 2D-MUSIC algorithm is asymptotically consistent and efficient by comparing the channel estimation NMSE against the CRLB. While this study did not include an RIS, the ideas used in this study apply to RIS-aided communication systems.

7.2 Future Work

In this thesis, we discovered, analyzed, and proposed solutions for inter-operator pilot contamination. In addition, we developed important analytical results for parametric channel estimation. However, the analysis for the latter case only applies to pure-LOS conditions, which is usually not the case in real wireless communication systems. Therefore, a more generalized analysis is required to cover hybrid cases where the channel has a LOS component and Non-Line of Sight (NLOS) fading components. In addition, implementing non-linear estimators for the parametric estimation framework and comparing their performance with the CRLB for channel estimation and positioning derived in Chapter 5 is a promising step. Even then, for practical applications, remedies for channels with NLOS components should be devised. Another interesting extension would be localization-aided channel estimation, where localization information is utilized to improve the channel estimation performance. Moreover, we always assumed continuous RIS-configuration phases in our studies. Considering discrete phases will probably result in mixed integer optimization problems or search problems, however, such a research direction will help the RIS technology become a reality.

References

[1] E. Dahlman, S. Parkvall, and J. Skold, *5G NR: The Next Generation Wireless Access Technology*. USA: Academic Press, Inc., 1st ed., 2018.

[2] E. G. Larsson, O. Edfors, F. Tufvesson, and T. L. Marzetta, "Massive MIMO for next generation wireless systems," *IEEE Communications Magazine*, vol. 52, no. 2, pp. 186–195, 2014.

[3] J. G. Andrews, S. Buzzi, W. Choi, S. V. Hanly, A. Lozano, A. C. K. Soong, and J. C. Zhang, "What will 5G be?," *IEEE Journal on Selected Areas in Communications*, vol. 32, no. 6, pp. 1065–1082, 2014.

[4] B. Hochwald, T. Marzetta, and V. Tarokh, "Multiple-antenna channel hardening and its implications for rate feedback and scheduling," *IEEE Transactions on Information Theory*, vol. 50, no. 9, pp. 1893–1909, 2004.

[5] W. Saad, M. Bennis, and M. Chen, "A vision of 6G wireless systems: Applications, trends, technologies, and open research problems," *IEEE Network*, vol. 34, no. 3, pp. 134–142, 2020.

[6] E. Basar, M. Di Renzo, J. De Rosny, M. Debbah, M.-S. Alouini, and R. Zhang, "Wireless communications through reconfigurable intelligent surfaces," *IEEE Access*, vol. 7, pp. 116753–116773, 2019.

[7] B. Rana, S.-S. Cho, and I.-P. Hong, "Review paper on hardware of reconfigurable intelligent surfaces," *IEEE Access*, vol. 11, pp. 29614–29634, 2023.

[8] S. K. R. Vuyyuru, R. Valkonen, D.-H. Kwon, and S. A. Tretyakov, "Efficient anomalous reflector design using array antenna scattering synthesis," $IEEE_{JA}WPL, vol.\ 22, pp.\ 1711 - -1715, July 2023$.

[9] S. K. R. Vuyyuru, R. Valkonen, S. A. Tretyakov, and D.-H. Kwon, "Efficient synthesis of passively loaded finite arrays for tunable anomalous reflection," *arXiv preprint arXiv:2312.04441*, 2023.

[10] G. Mylonopoulos, C. D'Andrea, and S. Buzzi, "Active reconfigurable intelligent surfaces for user localization in mmWave MIMO systems," in *IEEE 23rd*

International Workshop on Signal Processing Advances in Wireless Communication (SPAWC), pp. 1–5, 2022.

[11] R. Schmidt, "Multiple emitter location and signal parameter estimation," *IEEE Transactions on Antennas and Propagation*, vol. 34, no. 3, pp. 276–280, 1986.

[12] H. V. Poor, *An Introduction to Signal Detection and Estimation (2nd Ed.)*. Berlin, Heidelberg: Springer-Verlag, 1994.

[13] T. L. Marzetta, E. G. Larsson, H. Yang, and H. Q. Ngo, *Fundamentals of Massive MIMO*. Cambridge University Press, 2016.

[14] A. Kosasih, Ö. T. Demir, and E. Björnson, "Parametric near-field channel estimation for extremely large aperture arrays," in *2023 57th Asilomar Conference on Signals, Systems, and Computers*, pp. 162–166, 2023.

[15] D. Gürgünoğlu, E. Björnson, and G. Fodor, "Impact of pilot contamination between operators with interfering reconfigurable intelligent surfaces," in *2023 IEEE International Black Sea Conference on Communications and Networking (BlackSeaCom)*, pp. 27–32, 2023.

[16] D. Gürgünoğlu, E. Björnson, and G. Fodor, "Combating inter-operator pilot contamination in reconfigurable intelligent surfaces assisted multi-operator networks," *IEEE Transactions on Communications*, vol. 72, no. 9, pp. 5884–5895, 2024.

[17] E. Björnson and P. Ramezani, "Maximum likelihood channel estimation for RIS-aided communications with LOS channels," in *Asilomar Conference on Signals, Systems and Computers*, 2022.

[18] T. L. Marzetta, "Noncooperative cellular wireless with unlimited numbers of base station antennas," *IEEE Trans. Wireless Commun.*, vol. 9, no. 11, pp. 3590–3600, 2010.

[19] L. Sanguinetti, E. Björnson, and J. Hoydis, "Toward Massive MIMO 2.0: Understanding spatial correlation, interference suppression, and pilot contamination," *IEEE Trans. Commun.*, vol. 68, no. 1, 2020.

[20] J. Jose, A. Ashikhmin, T. L. Marzetta, and S. Vishwanath, "Pilot contamination and precoding in multi-cell TDD systems," vol. 10, no. 8, pp. 2640–2651, 2011.

[21] V. Saxena, G. Fodor, and E. Karipidis, "Mitigating pilot contamination by pilot reuse and power control schemes for massive MIMO systems," in *2015 IEEE 81st Vehicular Technology Conference (VTC Spring)*, pp. 1–6, 2015.

[22] C. Pan, H. Ren, K. Wang, J. F. Kolb, M. Elkashlan, M. Chen, M. Di Renzo, Y. Hao, J. Wang, A. L. Swindlehurst, X. You, and L. Hanzo, "Reconfigurable intelligent surfaces for 6G systems: Principles, applications, and research directions," *IEEE Communications Magazine*, vol. 59, no. 6, pp. 14–20, 2021.

[23] E. Björnson, Ö. Özdogan, and E. G. Larsson, "Reconfigurable intelligent surfaces: Three myths and two critical questions," no. 12, pp. 90–96, 2020.

[24] L. Wei, C. Huang, G. C. Alexandropoulos, C. Yuen, Z. Zhang, and M. Debbah, "Channel estimation for RIS-empowered multi-user MISO wireless communications," *IEEE Transactions on Communications*, vol. 69, no. 6, pp. 4144–4157, 2021.

[25] C. Huang, A. Zappone, G. C. Alexandropoulos, M. Debbah, and C. Yuen, "Reconfigurable intelligent surfaces for energy efficiency in wireless communication," vol. 18, no. 8, pp. 4157–4170, 2019.

[26] N. Garg, H. Ge, and T. Ratnarajah, "Generalized superimposed training scheme in IRS-assisted cell-free massive mimo systems," *IEEE Journal of Selected Topics in Signal Processing*, vol. 16, no. 5, pp. 1157–1171, 2022.

[27] 3GPP, "NR; Physical channels and modulation," Technical Specification (TS) 38.211, 3rd Generation Partnership Project (3GPP), 09 2022. Version 17.4.0.

[28] S. M. Kay, *Fundamentals of Statistical Signal Processing, Volume I: Estimation Theory*. Prentice Hall, 1993.

[29] G. Fodor, N. Rajatheva, W. Zirwas, L. Thiele, M. Kurras, K. Guo, A. Tolli, J. H. Sorensen, and E. De Carvalho, "An overview of massive MIMO technology components in METIS," *IEEE Communications Magazine*, vol. 55, no. 6, pp. 155–161, 2017.

[30] G. T. de Araújo, A. L. F. de Almeida, R. Boyer, and G. Fodor, "Semi-blind joint channel and symbol estimation for IRS-assisted MIMO systems," *IEEE Transactions on Signal Processing*, vol. 71, pp. 1184–1199, 2023.

[31] R. Liu, M. Li, H. Luo, Q. Liu, and A. L. Swindlehurst, "Integrated sensing and communication with reconfigurable intelligent surfaces: Opportunities, applications, and future directions," *IEEE Wireless Communications*, vol. 30, no. 1, pp. 50–57, 2023.

[32] Z. Zhang, L. Dai, X. Chen, C. Liu, F. Yang, R. Schober, and H. V. Poor, "Active RIS vs. passive RIS: Which will prevail in 6G?," *IEEE Transactions on Communications*, vol. 71, no. 3, pp. 1707–1725, 2023.

[33] M. Rihan, A. Zappone, S. Buzzi, G. Fodor, and M. Debbah, "Passive vs. active reconfigurable intelligent surfaces for integrated sensing and communication: Challenges and opportunities," *IEEE Network*, pp. 1–1, 2023.

[34] S. Zhang and R. Zhang, "Capacity characterization for intelligent reflecting surface aided MIMO communication," *IEEE Journal on Selected Areas in Communications*, vol. 38, no. 8, pp. 1823–1838, 2020.

[35] X. Pei, H. Yin, L. Tan, L. Cao, Z. Li, K. Wang, K. Zhang, and E. Björnson, "RIS-aided wireless communications: Prototyping, adaptive beamforming, and indoor/outdoor field trials," 2021.

[36] V. Tapio, A. Shojaeifard, I. Hemadeh, A. Mourad, and M. Juntti, "Reconfigurable intelligent surface for 5g NR uplink coverage enhancement," in *2021 IEEE 94th Vehicular Technology Conference (VTC2021-Fall)*, pp. 1–5, 2021.

[37] Y. Zhao and X. Lv, "Network coexistence analysis of RIS-assisted wireless communications," *IEEE Access*, vol. 10, pp. 63442–63454, 2022.

[38] M. Vincenzi, A. Antonopoulos, E. Kartsakli, J. Vardakas, L. Alonso, and C. Verikoukis, "Cooperation incentives for multi-operator C-RAN energy efficient sharing," in *2017 IEEE International Conference on Communications (ICC)*, pp. 1–6, 2017.

[39] H.-T. Chien, Y.-D. Lin, H.-W. Chang, and C.-L. Lai, "Multi-operator fairness in transparent RAN sharing by soft-partition with blocking and dropping mechanism," *IEEE Transactions on Vehicular Technology*, vol. 67, no. 12, pp. 11597–11605, 2018.

[40] H.-S. Guan, Y.-L. Kuang, G.-Z. Huang, and X.-B. Li, "Analysis of far-field radiation and multi antenna coupling characteristics of antenna on shared tower," in *2020 6th Global Electromagnetic Compatibility Conference (GEMCCON)*, pp. 1–4, 2020.

[41] P. Zheng, X. Ma, and T. Y. Al-Naffouri, "On the impact of mutual coupling on RIS-assisted channel estimation," 2023.

[42] Z. Yu and D. Yuan, "Resource optimization with interference coupling in multi-RIS-assisted multi-cell systems," *IEEE Open Journal of Vehicular Technology*, vol. 3, pp. 98–110, 2022.

[43] E. Björnson and L. Sanguinetti, "Rayleigh fading modeling and channel hardening for reconfigurable intelligent surfaces," *IEEE Wireless Communications Letters*, vol. 10, no. 4, pp. 830–834, 2021.

[44] A. Goldsmith, S. Jafar, N. Jindal, and S. Vishwanath, "Capacity limits of MIMO channels," *IEEE Journal on Selected Areas in Communications*, vol. 21, no. 5, pp. 684–702, 2003.

[45] S. Yang and L. Hanzo, "Fifty years of MIMO detection: The road to large-scale MIMOs," *IEEE Communications Surveys & Tutorials*, vol. 17, no. 4, pp. 1941–1988, 2015.

[46] D. Gesbert, M. Kountouris, R. W. Heath, C.-b. Chae, and T. Salzer, "Shifting the MIMO paradigm," *IEEE Signal Processing Magazine*, vol. 24, no. 5, pp. 36–46, 2007.

[47] T. L. Marzetta, "Massive MIMO: An introduction," *Bell Labs Technical Journal*, vol. 20, pp. 11–22, 2015.

[48] F. Rusek, D. Persson, B. K. Lau, E. G. Larsson, T. L. Marzetta, O. Edfors, and F. Tufvesson, "Scaling up MIMO: Opportunities and challenges with very large arrays," *IEEE Signal Processing Magazine*, vol. 30, no. 1, pp. 40–60, 2013.

[49] J. Jeon, G. Lee, A. A. Ibrahim, J. Yuan, G. Xu, J. Cho, E. Onggosanusi, Y. Kim, J. Lee, and J. C. Zhang, "MIMO evolution toward 6G: Modular massive MIMO in low-frequency bands," *IEEE Communications Magazine*, vol. 59, no. 11, pp. 52–58, 2021.

[50] S. Zeng, B. Di, H. Zhang, J. Gao, S. Yue, X. Hu, R. Fu, J. Zhou, X. Liu, H. Zhang, Y. Wang, S. Sun, H. Qin, X. Su, M. Wang, and L. Song, "RIS-based IMT-2030 testbed for MmWave multi-stream ultra-massive MIMO communications," *IEEE Wireless Communications*, vol. 31, no. 3, pp. 375–382, 2024.

[51] D. G. Brennan, "Linear diversity combining techniques," *Proceedings of the IRE*, vol. 47, no. 6, pp. 1075–1102, 1959.

[52] O. Frost, "An algorithm for linearly constrained adaptive array processing," *Proceedings of the IEEE*, vol. 60, no. 8, pp. 926–935, 1972.

[53] A. Popovska Avramova and V. B. Iversen, "Radio access sharing strategies for multiple operators in cellular networks," in *2015 IEEE International Conference on Communication Workshop (ICCW)*, pp. 1113–1118, 2015.

[54] S. K. A. Kumar and E. Oughton, "Techno-economic assessment of 5G infrastructure sharing business models in rural areas," *Frontiers in Computer Science*, pp. 01–22, 2023. DoI: 10.3389/fcomp.2023.1191853.

[55] E. J. Oughton, K. Katsaros, F. Entezami, D. Kaleshi, and J. Crowcroft, "An open-source techno-economic assessment framework for 5G deployment," *IEEE Access*, vol. 7, pp. 155930–155940, 2019.

[56] E. J. Oughton and W. Lehr, "Surveying 5G techno-economic research to inform the evaluation of 6G wireless technologies," *IEEE Access*, vol. 10, pp. 25237–25257, 2022.

[57] M. S. B. Syed, H. M. Attaullah, S. Ali, and M. I. Aslam, "Wireless communications beyond antennas: The role of reconfigurable intelligent surfaces," *Engineering Proceedings*, vol. 32, no. 1, 2023.

[58] S. H. Zainud-Deen, "Reconfigurable intelligent surfaces for wireless communications," in *2022 39th National Radio Science Conference (NRSC)*, vol. 1, pp. 342–342, 2022.

[59] M. Rihan, A. Zappone, S. Buzzi, G. Fodor, and M. Debbah, "Passive versus active reconfigurable intelligent surfaces for integrated sensing and communication: Challenges and opportunities," *IEEE Network*, vol. 38, no. 3, pp. 218–226, 2024.

[60] C. Pan, H. Ren, K. Wang, J. F. Kolb, M. Elkashlan, M. Chen, M. Di Renzo, Y. Hao, J. Wang, A. L. Swindlehurst, X. You, and L. Hanzo, "Reconfigurable intelligent surfaces for 6G systems: Principles, applications, and research directions," *IEEE Communications Magazine*, vol. 59, no. 6, pp. 14–20, 2021.

[61] E. Ayanoglu, F. Capolino, and A. L. Swindlehurst, "Wave-controlled metasurface-based reconfigurable intelligent surfaces," *IEEE Wireless Communications*, vol. 29, no. 4, pp. 86–92, 2022.

[62] J. Das, P. Das, A. Chandra, B. P. S. Sahoo, S. K. Vankayala, and S. Yoon, "Reducing pilot overhead for channel estimation in RIS-assisted millimeter-wave systems," in *2023 IEEE International Conference on Electronics, Computing and Communication Technologies (CONECCT)*, pp. 1–6, 2023.

[63] G. Zhou, C. Pan, H. Ren, P. Popovski, and A. L. Swindlehurst, "Channel estimation for RIS-aided multiuser millimeter-wave systems," *IEEE Transactions on Signal Processing*, vol. 70, pp. 1478–1492, 2022.

[64] S. Kim and B. Shim, "Channel estimation for reconfigurable intelligent surface-aided mmwave communications," in *GLOBECOM 2022 - 2022 IEEE Global Communications Conference*, pp. 5396–5401, 2022.

[65] N. I. Miridakis, T. A. Tsiftsis, P. A. Karkazis, H. C. Leligou, and P. Popovski, "Impact of inter-operator interference via reconfigurable intelligent surfaces," *IEEE Wireless Communications Letters*, vol. 13, no. 9, pp. 2536–2540, 2024.

[66] G. T. de Araújo, A. L. F. de Almeida, R. Boyer, and G. Fodor, "Semi-blind joint channel and symbol estimation for irs-assisted mimo systems," *IEEE Transactions on Signal Processing*, vol. 71, pp. 1184–1199, 2023.

[67] C.-X. Wang, X. You, X. Gao, X. Zhu, Z. Li, C. Zhang, H. Wang, Y. Huang, Y. Chen, H. Haas, J. S. Thompson, E. G. Larsson, M. D. Renzo, W. Tong, P. Zhu, X. Shen, H. V. Poor, and L. Hanzo, "On the road to 6G: Visions, requirements, key technologies, and testbeds," *IEEE Communications Surveys & Tutorials*, vol. 25, no. 2, pp. 905–974, 2023.

[68] E. Björnson, H. Wymeersch, B. Matthiesen, P. Popovski, L. Sanguinetti, and E. de Carvalho, "Reconfigurable intelligent surfaces: A signal processing perspective with wireless applications," *IEEE Signal Processing Magazine*, vol. 39, no. 2, pp. 135–158, 2022.

[69] C. Ozturk, M. F. Keskin, H. Wymeersch, and S. Gezici, "RIS-aided near-field localization under phase-dependent amplitude variations," *IEEE Transactions on Wireless Communications*, vol. 22, no. 8, pp. 5550–5566, 2023.

[70] C. Ozturk, M. F. Keskin, V. Sciancalepore, H. Wymeersch, and S. Gezici, "Ris-aided localization under pixel failures," *IEEE Transactions on Wireless Communications*, pp. 1–1, 2024.

[71] S. Palmucci, A. Guerra, A. Abrardo, and D. Dardari, "Two-timescale joint precoding design and RIS optimization for user tracking in near-field MIMO systems," *IEEE Transactions on Signal Processing*, vol. 71, pp. 3067–3082, 2023.

[72] F. Jiang, A. Abrardo, K. Keykhosravi, H. Wymeersch, D. Dardari, and M. Di Renzo, "Two-timescale transmission design and ris optimization for integrated localization and communications," *IEEE Transactions on Wireless Communications*, vol. 22, no. 12, pp. 8587–8602, 2023.

[73] X. Hu, C. Zhong, Y. Zhang, X. Chen, and Z. Zhang, "Location information aided multiple intelligent reflecting surface systems," *IEEE Transactions on Communications*, vol. 68, no. 12, pp. 7948–7962, 2020.

[74] R. Zamir, "A proof of the Fisher information inequality via a data processing argument," *IEEE Transactions on Information Theory*, vol. 44, no. 3, pp. 1246–1250, 1998.

[75] S. Buzzi and C. D'Andrea, "Massive mimo 5g cellular networks: mm-wave vs. -wave frequencies," *ZTE Communications*, vol. 15 (S1), pp. 41–49, 2017.

[76] E. Björnson, L. Sanguinetti, H. Wymeersch, J. Hoydis, and T. L. Marzetta, "Massive MIMO is a reality—What is next? Five promising research directions for antenna arrays," *Digital Signal Processing*, vol. 94, pp. 3–20, Nov. 2019.

[77] H. Wang, A. Kosasih, C. -K. Wen, S. Jin and W. Hardjawana, "Expectation propagation detector for extra-large scale massive MIMO," *IEEE Trans. Wireless Commun.*, vol. 19, pp. 2036–2051, Mar. 2020.

[78] A. Amiri, M. Angjelichinoski, E. de Carvalho, and R. W. Heath, "Extremely large aperture massive MIMO: Low complexity receiver architectures," in *Proc. IEEE Global Commun. Conf. Workshops*, (UAE), Dec. 2018.

[79] T. S. Rappaport et al., "Wireless communications and applications above 100 GHz: Opportunities and challenges for 6G and beyond," *IEEE Access*, vol. 7, pp. 78729–78757, June 2019.

[80] L. Sanguinetti, E. Björnson, and J. Hoydis, "Toward massive MIMO 2.0: Understanding spatial correlation, interference suppression, and pilot contamination," *IEEE J. Sel. Areas Commun.*, vol. 68, p. 232–257, Jan. 2020.

[81] E. Björnson and L. Sanguinetti, "Power scaling laws and near-field behaviors of massive MIMO and intelligent reflecting surfaces," *IEEE Open J. of the Commun. Soc.*, vol. 1, pp. 1306–1324, Sept. 2020.

[82] M. Cui and L. Dai, "Channel estimation for extremely large-scale MIMO: Far-field or near-field?," *IRE Trans. Commun.*, vol. 70, pp. 2663–2677, Apr. 2022.

[83] Z. Wu and L. Dai, "Multiple access for near-field communications: SDMA or LDMA?," *IEEE J. Sel. Areas Commun.*, early access.

[84] D. Gürgünoğlu, E. Björnson, and G. Fodor, "Joint pilot-based localization and channel estimation in ris-aided communication systems," *IEEE Wireless Communications Letters*, vol. 13, no. 11, pp. 3119–3123, 2024.

[85] N. Babu, A. Kosasih, C. Masouros, and E. Björnson, "Symbol-level precoding for near-field ISAC," *IEEE Commun. Lett.*, vol. 28, pp. 2041–2045, 9 2024.